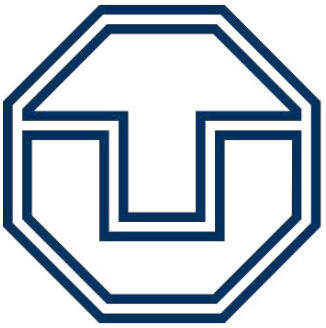

TECHNISCHE UNIVERSITÄT DRESDEN

HEAT AND MASS TRANSFER TO PARTICLES IN PULSATING FLOWS

Von der Fakultät Maschinenwesen der Technischen Universität Dresden zur Erlangung des akademischen Grades

Doktoringenieur (Dr.-Ing.)

angenommene Dissertation

Dipl.-Ing. Heidinger, Stefan

Promotionskommission:

Vorsitz:	Prof. Dr.-Ing. Frank Atzler
	TU Dresden, Institut für Automobiltechnik Dresden
Gutachter:	Prof. Dr. Michael Beckmann
	TU Dresden, Institut für Verfahrenstechnik und Umwelttechnik
	Prof. Dr. André Thess
	Universität Stuttgart, Institut für Energiespeicherung
Prüfer:	Prof. Dr. Antonio Hurtado
	TU Dresden, Institut für Energietechnik
Weiteres Mitglied:	Prof. Dr. Wolfgang Lippmann
	TU Dresden, Institut für Energietechnik

Tag der Einreichung: 29.03.2023 - Tag der Verteidigung: 10.11.2023

Statutory Declaration

I herewith declare that I have composed the present thesis myself and without use of any other than the cited sources and aids. Sentences or parts of sentences quoted literally are marked as such; other references with regard to the statement and scope are indicated by full details of the publications concerned. The thesis in the same or similar form has not been submitted to any examination body and has not been published.

Place, Date Signature (Stefan Heidinger)

Table of Contents

List of Figures

List of Tables

List of Symbols

Roman

$\bar{y}$	Correlation Range
$\hat{y}_i$	Correlation Point
a	Particle Acceleration
C_C	Cunningham Factor
D	Mass Diffusivity
d	Particle Diameter
d_{tube}	Diameter of Resonance Tube
F	Force
f	Oscillation/Pulsation Frequency
G	Gravitational Force
j	Number of Sample Points
L	Characteristic Length
m	Mass
n	Molecules per Unit Volume
P	Pressure Amplitude
p	Pressure
q	Electric Charge
R	Particle Radius
T	Fluid Temperature
t	Time
Tu	Degree of Turbulence
U	Slip Velocity Amplitude
u	Slip Velocity
U_f	Fluid Velocity Amplitude
u_f	Fluid Velocity
U_p	Particle Velocity Amplitude
u_p	Particle Velocity
V	Volume
y_i	Data Point

Greek

α	Thermal Diffusivity
β	Direction of Influence
δ	Boundary Layer Thickness
η	Dynamic Fluid Viscosity
κ	Heat Capacity Ratio
λ	Thermal Conductivity
λ_r	Thermal Conductivity Ratio
λ_{mfp}	Mean Free Path
ν	Kinematic Fluid Viscosity

ω	Angular Frequency
$\overrightarrow{\Psi}$	Gradient of Influence
ϕ	Phase Shift Angle
ρ_f	Fluid Density
ρ_p	Particle Density
σ_T	Thermal Accommodation Coefficient
σ_u	Momentum Accommodation Coefficient
τ	Characteristic Relaxation Time
ζ	General Flow Variable

Dimensionless Numbers

ϵ	Amplitude Parameter
γ	Density Ratio
CFL	Courant-Friedrichs-Lewy number
Kn	Knudsen Number
Ma	Mach Number
Nu	Nusselt Number
Pe	Peclet Number
Pr	Prandtl Number
Re	Reynolds Number
Re_S	Streaming Reynolds Number
Sc	Schmidt Number
Sh	Sherwood Number
Sr	Strouhal Number
Stk	Oscillation Stokes Number
Wo^2	Womersley Number

Indices

0	Initial Condition
∞	Free Stream Condition
Bas	Basset
$crit$	Critical
f	Fluid
g	Gas
LL	Landau & Lifshitz
p	Particle
set	Settling
SN	Schiller & Naumann
Stk	Stokes
t	Terminal
$therm$	Thermophoretic
x	Main Flow Direction
y	Perpendicular to Main Flow Direction

Abbreviations

FRL	Fast Relaxation Limit
HMT	Heat and Mass Transfer
NSE	Navier Stokes Equation
ODE	Ordinary Differential Equation
$plane$	ϵ-Re plane as defined in Section 4.9

PR	Pulsation Reactor	$TMAC$	Tangential Momentum Accommodation Coefficient
SRL	Slow Relaxation Limit		
TAC	Thermal Accommodation Coefficient	TP	Tailpipe
		USL	Ultra Sonic Levitator

CHAPTER 1

Motivation

The pulsation reactor is an established apparatus for processing various kinds of materials. This ranges from simple spray drying applications, thermal treatment of powders, to the synthesis of catalysts and battery materials from precursors solved in combustible carrier liquids. Compared with other means of mass production, material treatment in a pulsation reactor can achieve advantageous properties, such as nano particle sizes and high specific surface areas. Pulsation reactors have been in use for several decades in industry and have reached technology readiness level 9, while adaptation and optimization still rely heavily on empirical knowledge and trial and error approaches. These approaches are time consuming and costly. This work provides a simple model for the heat and mass transfer to particles in pulsating and oscillating flows, with the focus on process conditions achievable in a pulsation reactor. Such a mathematical model enables the solving of adaptation and optimization problems theoretically and, therefore, with minimal effort. In this regard, the dimensionless Nusselt number and Sherwood number are key parameters for evaluating how the particular conditions in a pulsating flow translate to the heat and mass transfer rate at the individual level of the entrained particle.

CHAPTER 2

Introduction

The pulsation reactor [**1**], as displayed Figure 2.1, is a thermo-acoustic device and can be operated with a mixture of combustible gas and air. It consists of two main parts, a combustion chamber and an attached resonance tube, which together form a Helmholtz resonator [**2**]. If the volumes of the combustion chamber and the resonance tube are attuned to each other, a standing pressure wave will form in the resonance tube [**3**], leading to a pulsating flow as described in section 4.2. This reactor can be used for various forms of material treatment, from simple drying applications [**4**, **5**] all the way to achieving special properties for high performance materials [**6**]. The material for treatment is introduced to the pulsating flow at the beginning of the resonance tube and is dragged along to the end, where a filter chamber is positioned [**7**]. This chamber has two functions. On the one hand, it decouples the exhaust gas system from the pulsation reactor acoustically by providing a sudden increase in diameter as well as a volume which is not in tune with the pulsation reactor. Therefore, no additional Helmholtz resonator, which might interfere with the pulsation reactor, is created. On the other hand, it houses a filter system (fabric or cyclone) in order to separate the treated material from the gas stream.

The geometry of a PR determines the pulsation frequency (Helmholtz resonator), independent of the operating parameters (except for the influence of the fluid temperature and the resulting shift in the speed of sound), while a set PR can mainly be operated by controlling the fuel and air inflow. The dependencies between the operating parameters

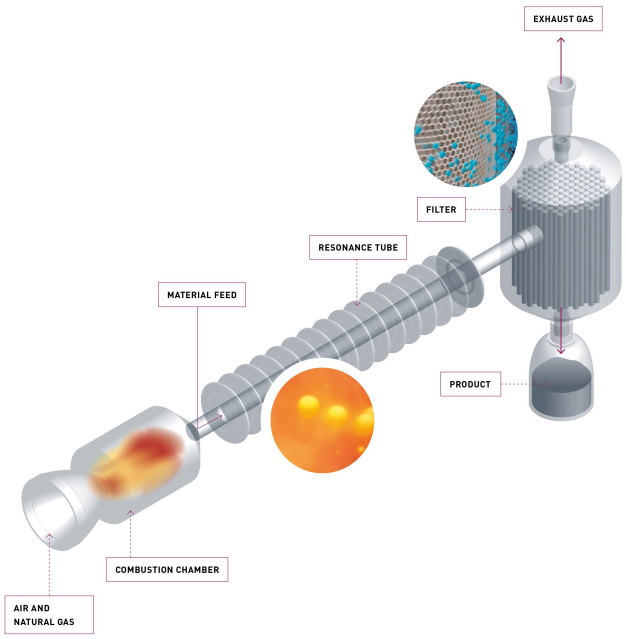

Figure 2.1. Schematic of a pulsation reactor @IBU-tec [**7**].

and the resulting process parameters in a PR are complex and have been the subject of past and ongoing research [**8**]. Many investigations into this topic were conducted for pulsating combustors only, detached from material treatment [**9**, **10**]. Together with the material properties, those quantities form a new set of operating parameters, as illustrated in Figure 2.2. Those operating parameters generate process conditions in the PR, such as fluid temperature, fluid velocity, distinguishable into velocity amplitude and frequency, as well as the particle parameters of size and density. This work does not focus on the operating parameters itself, but is concerned with the process parameters they generate, and it is investigated how the heat and mass transfer (HMT) to the material particles is influenced by the process parameters in the PR. These process parameters function as input parameters for modelling the HMT to a single particle, as displayed in Figure 2.2. Pulsation reactors can be scaled in quite large ranges with respect to operating and process parameters, but rough estimates, supported by existing plants,

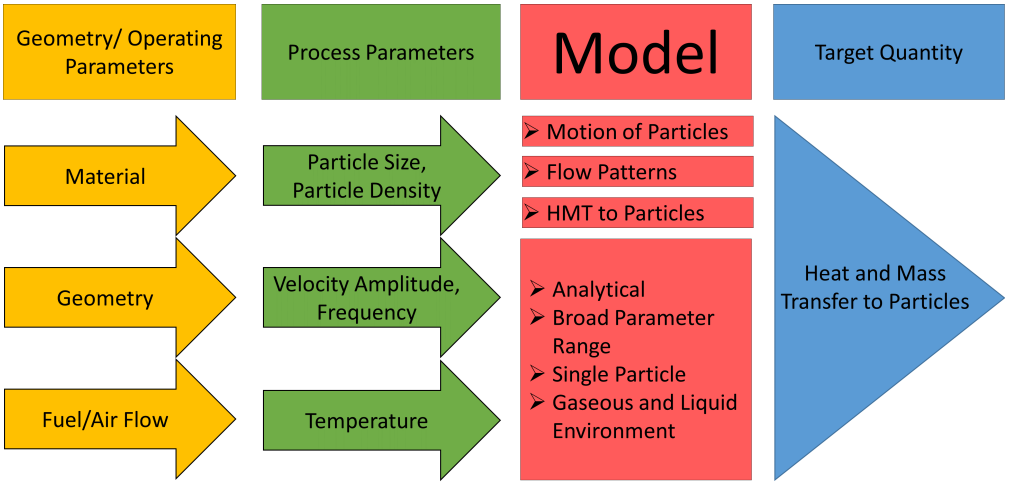

Figure 2.2. Classification of influential parameters and interaction with the model.

industry experts, and literature, are listed in Table 2.1. Nevertheless, the model is designed to deal with input parameter ranges far exceeding those listed in Table 2.1 in order to provide a comprehensive treatment of the HMT to particles (even small spheres) in pulsating (oscillating) flows. This also enables a better assessment of potential for PR technology and pulsating flow HMT enhancement to particles in general. The model can be operated analytically in most cases, while it is not confined to only gases but also incorporates liquids. The model can also be applied for a particle trapped in an ultra sonic levitator (USL), which is highlighted at points throughout the work. After this short introduction, the current state of the research on this topic is presented in Chapter 3. Then, the basic assumptions, consideration, simplifications, and constraints are discussed in Chapter 4. This is followed by the model, which can be divided into three distinct stages, as highlighted in Figure 2.2. Chapter 5 lays out the first stage of the model, which describes the motion of particles in oscillating flows. The second stage in Chapter 6 introduces the flow patterns developing in the vicinity of the particle, while depending directly on the motion of the particle relative to the surrounding flow.

Table 2.1. Operational and constructional parameter ranges of pulsation reactors **[6, 11, 12]**.

Parameter	**Range (approximately)**	**Often applied**
Reaction pipe length	1 m to 10 m	5 m
Combustion chamber volume	0.01 m^3 to 1 m^3	0.1 m^3
Fuel	natural gas, hydrogen	natural gas
Flow velocity	1 m/s to 50 m/s	10 m/s
Pulsation frequency	1-100	20 Hz
Temperature	300 °C to 1200 °C	450 °C to 950 °C
Pressure amplitude	up to 5000 Pa	350 Pa to 1500 Pa
Absolute pressure	10^5 Pa	10^5 Pa
Residence time	0.05 s to 2 s	0.5 s
Throughput (raw material)	0.1 kg/h to 20 kg/h	3 kg/h

Chapter 7 presents an analytical way of determining the HMT intensity to the particle, resulting from the first two stages of the model. The entire algorithm for determining the HMT to the particle is then summarized in Chapter 8 along with a case study of the pulsation reactor. Finally, possible opportunities of utilizing and expanding the model are presented in Chapter 9.

CHAPTER 3

State of the Art

This chapter starts with an overview of the literature on material treatment in pulsation reactors in general. This if followed by a more narrow focus on particle behaviour in pulsating flows. Here it follows a structure similar to the model itself. Similar to the derived model, which was introduced in Chapter 2, the literature is divided into the three distinct stages accordingly. First, the central works for the motion of particles and the literature important for the following considerations in this thesis are presented. Afterwards, a selection of literature for the flow patterns in the vicinity of a particle is introduced. A common approach in this literature is to assume a harmonic oscillating or pulsating slip velocity between particle and fluid and to investigate the behaviour of single particles in this manner. This research is often not connected to the previous bulk of literature and treated as a separate problem. Although the state of the research is not limited to the special phenomenon of Steady Streaming, most literature for flow patterns in oscillating flows is concerned with it. Subsequently, the state of literature for the HMT to particles is summarized while, again, being mostly disconnected to the previous two subtopics. Since the third stage of the model is approached with a structured literature review and a resulting meta correlation, more literature can be found within Chapter 7. Finally, it is laid out how non continuum effects for the motion and the HMT in connection with small particles are handled in the literature.

3.1. Material Treatment in the Pulsation Reactor

A comprehensive summary of pulsating combustion and applications is given by Zinn [**9**] and later by Meng et al. [**10**]. A more specific overview, tailored to pulsation reactors, is delivered by Hoffmann & Ommer [**1**], including working principle, historical development, enhanced heat and mass transfer, and possible applications. Complementary to their paper, Begand et al. [**13**] provide a good overview of the application of pulsation reactor technology in different fields for various tasks, namely drying, dehydration, decomposition reactions, oxidation, and change of modification. This is followed up by a detailed investigation into various influential parameters of material synthesis in the pulsation reactor, such as pressure oscillations, temperature, and residence time, by Begand [**14**]. The subjected materials were aluminum oxide, titanium oxide, yttrium(III) oxide, and zirconium oxide, while the particle size distribution, specific surface area, and crystal structure were investigated. Kudra [**4**] gives a structured overview on the status and potentials of pulse combustion spray drying. Wu & Lu [**15**] conducted a numerical study of a pulsation reactor for spray drying, which was partly validated by experiment. The atomization of the solution was achieved by the pulsating flow itself and led to a 50% reduced particle size compared to a nozzle-type atomizer. The evaporation rate was found to be around 6 times higher than for traditional spray drying applications.

3.2. Particle Motion in an Oscillating Fluid

While plenty of literature exist on the motion of particles in oscillating flows, only the most influential works and most relevant works for this thesis are presented. Basset [**16**], Boussinesq [**17**], and Oseen [**18**] laid the basis for most of the following considerations

with their drag formulation for unsteady particle motion (BBO equation):

$$F_{Bas} = 3\pi\eta du + \frac{\pi}{12}d^3\rho_f\frac{du}{dt} + \frac{3}{2}d^2\sqrt{\pi\rho_f\eta}\int_{t_0}^{t}\frac{du/dt}{\sqrt{t-t'}}dt' \tag{3.1}$$

where ρ_p, ρ_f, η, d, t and $u(t)$ denote, respectively, the particle and fluid density, the dynamic fluid viscosity, the particle diameter, time, and the slip velocity between particle and fluid. The first term considers pure drag, while the second term considers added mass. The last term was theoretically derived and is referred to as the *history term*. The transformed formulation for a unsteady fluid motion by Tchen [**19**] was later corrected by Maxey & Riley [**20**]. Equation 3.1 was solved analytically for a harmonic flow by Hjelmfelt & Mockros [**21**] and further examined by Chan et al. [**22**] and Coimbra & Rangel [**23**]. The case of a particle falling through a vertically oscillating fluid received much attention [**24**–**27**] because of its perceived practical significance [**28**], though Molerus [**29**] questioned the practical applicability of the approach. Houghten [**30**] formulated a nonlinear Langevin equation, predicting retardation in the settling velocity [**31**] due to the oscillating motion of the fluid. The theory could not be sufficiently validated by experiment, with several possible reasons for the discrepancies suggested by Herringe [**32**]. Abbad & Souhar [**33**] could confirm the validity of the history term in the Basset formulation by experiment for small particle displacement amplitudes $\epsilon \leq 1$ and moderate Reynolds numbers $Re \leq 2.5$. Since these formulations are mathematically only valid for small Reynolds numbers $Re \leq 1$, the terms in Equation 3.1 have been corrected with empirically derived factors by Odar & Hamilton [**34**] in order to extent their applicability to higher Reynolds numbers:

$$F_{Bas} = c_1\left(3\pi\eta du\right) + \Delta_A\left(\frac{\pi}{12}d^3\rho_f\frac{du}{dt}\right) + \Delta_H\left(\frac{3}{2}d^2\sqrt{\pi\rho_f\eta}\int_{t_0}^{t}\frac{du/dt}{\sqrt{t-t'}}dt'\right), \tag{3.2}$$

$$\text{with } c_1 = 1 + 0.15Re^{2/3} \quad \Delta_A = 1.05 - \frac{0.066}{0.12 + Ac} \quad \Delta_H = 2.88 + \frac{3.12}{(1+Ac^2)^3}$$

with the acceleration number $Ac = u^2/(a_p d)$. On the one hand, these factors alter the drag model by making it non-linear, requiring a numerical solution; on the other hand, Correlation 3.2 has been validated experimentally extensively and widely applied in engineering [**35**]. The range of validity for gas-solid flows has been shown to reach Reynolds numbers of 16,000 [**36**]. While several other authors, e.g. Karanfilan & Kotas [**37**], corrected the drag coefficient of the falling spheres with factors depending on the Reynolds number, Baird et al. [**38**] suggested a factor depending on the amplitude parameter ϵ. Mei [**39**] investigated the flow around a harmonically oscillating sphere with a Fourier mode expansion in the frequency domain, a time dependent finite difference technique in the time domain, and a matched asymptotic expansion for high-frequency oscillations. The author found that the total unsteady drag compares well with the experiments by Odar [**40**], while the inner of three boundary layers around the particle is governed by the quasi steady Stokes equation for large particle displacement amplitudes $\epsilon \gg 1$, and small Reynolds numbers $Re \ll 1$. For the same parameter case, Mei et al. [**41**, **42**] suggested a correction to the Basset history force. Landau & Lifshitz [**43**] derived an analytical drag model by linearizing the Navier-Stokes equations (NSEs) around small particle displacement amplitudes $\epsilon \ll 1$, which was later experimentally validated by Gupta et al. [**44**].

3.3. Steady Streaming (Flow Pattern)

Steady Streaming describes the second order phenomenon of steady (one directional) rotating vertices developing in the vicinity of a particle oscillating with a small amplitude parameter ϵ. It was first pointed out by Lord Rayleigh [**45**] and was then theoretically and practically considered by Schlichting [**46**]. Andres & Ingard [**47**] investigated the Steady Streaming pattern around a cylinder for a low Reynolds number oscillating flow by applying the Oseen approximation in order to solve the Navier-Stokes equations. Lane [**48**] took the previously developed model for Steady Streaming in the vicinity of

a cylinder by Raney et al. [**49**] (see also Holtsmark et al. [**50**]), which is based on a perturbation method, and adopted it for a sphere. Based on Lane's model, Thrasher & Westervelt [**51**] showed that the thickness of the inner Steady Streaming region increases with a decreasing Womersley number. Nyborg formulated a mathematical framework for Acoustic Streaming [**52**], a form of compressible flow Steady Streaming which is often associated with high sound frequencies. Based on the Nyborg framework, analytical models for this kind of streaming were derived in the case of rigid particles by Klaseboer et al. [**53**] and droplets and bubbles by Baasch et al. [**54**]. Nyborg also adopted the Acoustic Streaming framework for Steady Streaming near a rigid boundary [**55**]. Riley [**56**] developed a more general formulation of Steady Streaming, also via perturbation methods, after laying the groundwork before [**57**]. This is achieved by calculating the solutions for the oscillatory boundary layer and the outer flow separately, a concept worked out by Wang [**58**] and Stuart [**59**], and then matching them at the interface. Riley introduced the four dimensionless parameters, which are also adopted in this work and used in order to characterize flow states and flow patterns for particles in oscillating flows:

$$\text{amplitude parameter} \qquad \epsilon = U/\omega d; \tag{3.3}$$

$$\text{Womersley number} \qquad Wo^2 = \omega d^2/\nu; \tag{3.4}$$

$$\text{Reynolds number} \qquad Re = Ud/\nu; \tag{3.5}$$

$$\text{Streaming Reynolds number} \qquad Re_s = U^2/\omega\nu \tag{3.6}$$

with the slip velocity amplitude U, the kinematic fluid viscosity ν and the angular oscillation frequency ω. These dimensionless numbers are not independent and can be transformed into one another. Their meaning and dependencies are discussed more in

depth in Section 4.6. Since Riley only considered $\epsilon \ll 1$, in order to be able to linearize the equations of motion, the criteria for the following case descriptions also imply the ranges of the other parameters 3.3.

- $\boldsymbol{Wo^2 = O(1)}$ **(Case I):** Steady Streaming extends beyond the oscillatory boundary layer in the form of a Stokes flow and affects a large region compared with d.

- $\boldsymbol{Re = O(1)}$ **(Case II):** The Reynolds number does not play a vital role in this consideration and the flow patterns are comparable to Case I in nature.

- $\boldsymbol{Re_S = O(1)}$ **(Case III):** While for $Re_S \ll 1$ (Case I + II) the outer flow is Stokes-like, for $Re_S \gg 1$ the outer flow assumes a boundary-layer character in which the inner boundary layer is embedded. Here it becomes obvious that in the case of Steady Streaming, the Streaming Reynolds number is the primary determinant of the flow state and the flow pattern is similar to the Reynolds number for steady flows.

- $\boldsymbol{Wo^2 \ll 1}$ **(Case IV):** In this case, the oscillatory (inner) boundary layer will extend over a much wider region than d, comparable to the outer boundary layer in Case I + II.

The mathematical framework of Steady Streaming is further developed by Riley [**60**, **61**], while a clear distinction is drawn to Acoustic Streaming (aka Quartz Wind), which describes jet-like winds caused by the dissipation of acoustic energy in high frequency acoustic beams [**62**]. Steady Streaming near and in bubbles and droplets was experimentally investigated by Elder [**63**] and then theoretically considered by Davidson &

Riley [**64**] while applying Riley's case structure above. Longuet-Higgins [**65**, **66**] showed that a volume oscillation superimposed on the lateral oscillation considered by Davidson & Riley increases the Steady Streaming by an order of magnitude. Pozrikidis [**67**] investigated the oscillatory flow past spheroid particles numerically by linearizing the equations of motion with the restraint of $\epsilon < 1$ and then applying the boundary-integral method. Similar flow patterns were discovered for all considered particle shapes. Chang & Maxey [**68**] used a direct numerical simulation based on spectral methods in order to investigate the oscillatory motion of the flow around a sphere. They considered small Reynolds numbers and $0.1 \leq \epsilon \leq 10$, which differs from major portions of the literature, where the condition $\epsilon \ll 1$ is used to deduce linearized equations of motions. They found that flow separation occurs at lower Reynolds numbers in oscillating flows compared with steady flows. The steady streaming patterns of $\epsilon > 1$ were qualitatively similar to those of $\epsilon < 1$. A simulation of the same problem was conducted by Alassar & Badr [**69**], where the flow was calculated using truncation methods, with the Reynolds number being $10 \leq Re \leq 200$ and the amplitude parameter $0.16 \leq \epsilon \leq 1.3$. In this simulation, they were able to reproduce the anticipated double layer structure around the particle. This study was recently reproduced by Mishra et al. [**70**]. Alassar [**71**] conducted a numerical study which concluded that increasing the amplitude parameter ϵ strengthens the secondary streaming and the inner, rotating layer gets thinner at higher Reynolds numbers. This work investigated $25 \leq Re \leq 200$ and $0.125 \leq \epsilon \leq 5$. Klotsa et al. [**72**] investigated two close spheres in an oscillating flow and found an equilibrium gap between them due to a short range repulsive force and a long range attractive force. Then they investigated the resulting forming of chains of spheres due to this phenomenon [**73**]. This research was then intensified by Jalal et al. [**74**–**76**]. Steady Streaming was visualized experimentally

by Kotas et al. [**77**] using phase-locked particle pathlines and by Otto et al. [**78**] applying particle imaging velocimetry.

3.4. Heat and Mass Transfer in Oscillating Flows

Baxi & Ramachandran [**79**] experimentally investigated the heat transfer from oscillating spheres in air. They found a many-fold increase in heat transfer due to the oscillations. Larsen & Jensen [**80**] were able to experimentally enhance the mass transfer at a suspended droplet in air by up to 90% when applying a sound field with a loudspeaker. Mori et al. [**81**] investigated the heat and mass transfer from a sphere (solid and liquid) in a pulsating flow (steady flow superimposed with an oscillating flow). The setup was comparable to the flow in a pulsation reactor, with a quarter standing wave due to an open end resonance tube. They found an overall reduced heat and mass transfer, comparable with a steady flow. While Davidson [**64**] considered the heat transfer from a cylinder executing small oscillations in a fluid, Gopinath & Mills [**82**] adapted the approach for spheres with the condition of large Womersley numbers $Wo \gg 1$. They presented the empirically derived relation for the average Nusselt number $\overline{\overline{Nu}} = 1.413(Re)^{1/2}(\epsilon)^{1/2}Pr^{0.7}$ for a Prandtl number of $Pr \approx 1$, which was validated by experiment. The double overline indicates the average over the surface of the sphere and the oscillation cycle. Gopinath also considered small torsional particle oscillations [**83**] and the superposition of transverse and torsional oscillations [**84**]. Since large Womersley numbers relate to the acoustic streaming in an acoustic levitator, Kawahara et al. [**85**] built on the work of Gopinath when investigating the mass transfer at particles and droplets suspended in such a devices. They suggested the Sherwood number relation $\overline{\overline{Sh}} = 1.89U/\sqrt{\omega D} \approx 1.336Re^{1/2}\epsilon^{1/2}$ with the mass diffusivity D, after laying the foundation and discussing the flow patterns in Yarin et al. [**86**] and [**87**], respectively. Al Taweel & Landau [**88**] composed a comprehensive meta analysis on the mass transfer between solid spheres and oscillating fluids by

incorporating eleven previously published experimental studies and correlations for the average Sherwood number [**89**–**98**]. They suggested the following correlations for gases depending on the Schmidt number Sc:

$$\overline{Sh} = 1.1 Re^{1/2} \epsilon^{1/2} Sc^{1/2} \qquad \text{for } \epsilon < 0.4 \tag{3.7}$$

$$\overline{Sh} = 0.88 Re^{1/2} \epsilon^{1/2} Sc^{1/2} \qquad \text{for } 0.4 \leq \epsilon < 0.75 \tag{3.8}$$

$$\overline{Sh} = 2 + 0.382 Re^{1/2} Sc^{1/3} \qquad \text{for } \epsilon \geq 0.75 \tag{3.9}$$

Drummond & Lyman [**99**] applied a pseudospectral numerical method on the considerations of Al Taweel & Landau and suggested that the flow transition already takes place at $\epsilon \approx 0.25$ and the Sherwood number becomes independent from ϵ above this value. Their consideration was confined to $1 < Re < 150$. A qualitatively similar behavior was found by Alassar et al. [**100**] in case of the average Nusselt number for a sphere in an oscillating flow. A minimum at $\epsilon \approx 1$ was found in this numerical study. Ohmi et al. [**101**] theoretically considered a pulsating flow by superimposing previous suggested Sherwood correlations for steady and oscillating flows around spheres [**81**,**94**,**98**]. The theoretically found Sherwood correlation could not be confirmed by experiments with a naphthalene covered sphere [**102**]; instead, the correlation $\overline{\overline{Sh}} = 2 + [0.11 + 0.38(U/\overline{U})^{3/5}(\epsilon)^{1/5}]^{1/4} Sc^{1/3} Re^{1/2}$ was suggested. Ha [**103**] and then Ha & Yavuzkurt [**104**] found an up to 290% enhancement of the average Nusselt number in the presence of an acoustic field at the particles. In this numerical simulation, only particles of 100 µm were considered, while the fluid velocity amplitude was varied $2.5\,\mathrm{ms}^{-1} \leq U_f \leq 15\,\mathrm{ms}^{-1}$. Frequencies of 50 Hz, 1000 Hz, and 2000 Hz are applied, which results in amplitude parameters of $12.5 \leq \epsilon \leq 500$. The following empirical relation is suggested for the average Nusselt number:

$$\overline{\overline{Nu}} - 2 = 0.41954 \sqrt{Re} Pr^{1/3} \tag{3.10}$$

This study is followed by a similar one with a pulsating flow instead of an oscillating flow [**105**]. It delivers an empiric correlation of the space- and time-averaged Nusselt(Sherwood) number:

$$\frac{\overline{\overline{Nu_t}}-2}{\overline{\overline{Nu_0}}-2}=\frac{\overline{\overline{Sh_t}}-2}{\overline{\overline{Sh_0}}-2}=F\left(\frac{U}{\overline{\overline{U}}}\right)\quad F=1+9.608\times10^{-3}\frac{U}{\overline{\overline{U}}}-0.109608\left(\frac{U}{\overline{\overline{U}}}\right)^2 \tag{3.11}$$

It depends on the ratio of steady velocity $\overline{U}$ to the acoustic velocity amplitude U. Parts of this study where reproduced by Jiang et al. [**106**]. The results are the influence of body curvature in relation to the influence of flow acceleration when considering pressure gradient, shear stress, and flow separation. This paper investigates the specific flow characteristics in the vicinity of coal particles in a boiler. It assumes a constant particle diameter of 100 µm and a constant gas temperature of 1200 °C, which determines all gas properties. The oscillation frequencies were chosen as 50 Hz and 5000 Hz. This is a remake of Ha's study [**103**] with different parameters and is in accordance with Ha's results. Jiang et al. also confirmed the work of Gopinath & Mills, while presenting a detailed analysis of the influential phenomenon of heat transfer due to acoustic streaming [**107**, **108**]. Blackburn [**109**] conducted a numerical investigation on the drag coefficient and the Sherwood number with $0.05 \leq \epsilon \leq 5$ and $1 \leq Re \leq 100$. It was concluded that the drag matches Basset's solution well, even for high Reynolds numbers. Nevertheless, the mean Sherwood number was lower in every case than in the steady case when calculated with the corresponding rms flow value. A good overview and introduction into particles and droplets in standing wave levitator is given by Lierke [**110**], with an emphasize on heat and mass transfer in [**111**]. It is complemented by Sadhal's [**112**] overview of the flow pattern around a solid spheroid particle in a acoustic levitator.

3.5. Heat and Mass Transfer in Pulsating Flows

Guinon et al. [**113**] fostered a steady state approach for mass transfer to particles in pulsating flows by applying an averaged slip velocity. They found experimentally that pulsation dampens the mass transfer without flow reversal and enhances mass transfer with flow reversal. The following quasi steady Sherwood correlations were proposed:

$$Sh = 1.23 Sc^{1/3} Re^{0.23} \quad \text{for} \quad Re \leq 20 \tag{3.12}$$

$$Sh = 0.39 Sc^{1/3} Re^{0.58} \quad \text{for} \quad Re > 20 \tag{3.13}$$

Mishra et al. [**70**] conducted a numerical study of pulsatile flows around a sphere for power-law fluids. In case of a Newtonian fluid, the correlation for the average Nusselt number at the particle $\overline{\overline{Nu}} = 2 + 0.232 Re^{0.547} Pr^{0.398} [1 + \epsilon^{-0.044} (U/\overline{U})^{0.154}]$ was suggested. Carvalho [**114**] derived an equation of motion for solid particles in pulsating flows. The equation was solved by using a fourth-order Runge–Kutta method, while the behavior of coal-ash-type and coal material particles was investigated in the hot flow of a Rijke pulsating combustor. The author found that the particle average velocity is higher in pulsating flows, while also possessing sinusoidal behavior. Mass transfer in a pulsed column was experimentally investigated by Krasuk & Smith [**115**, **116**]. They found an increase in the mass transfer coefficient with pulse velocity. Liu et. al. [**117**] experimentally investigated the mean heat transfer from a brass sphere in an pulsating flow, created by a pulse combustor. An empirical equation for the mean Nusselt number with the mean Reynolds number $\overline{Re}$ and the pulsation frequency f was suggested:

$$\overline{Nu} = \left(2 + 0.6 \overline{Re}^{1/2} Pr^{1/3}\right) (1 + f)^{0.15} \quad for \quad 3.5 < \overline{Re} < 76000 \tag{3.14}$$

Teiwes et al. [**118**] calculated the process conditions in a pulsation reactor by CFD and then calculated the motion of discrete particles in it. An enhanced heat and mass transfer between gas and particles up to 40% was found compared with steady flow conditions. Dahm [**119**] investigated the heat transfer at particles in pulsation reactors. A correlation for the Nusselt number is suggested, considering the enhanced degree of turbulence Tu in a pulsation reactor compared with an entrained flow reactor:

$$\overline{Nu} = 2 + 0.364 \left(\sqrt{Re} + 3.54 Re \frac{Pr}{Pr_{turb}} Tu^2 \right) \tag{3.15}$$

The value of Pr_{turb} is discussed and assumed to be 0.5 for pulsation reactors. Furthermore, only a maximum of 3% of the occurring heat transfer from the hot gas to the particles is attributed to radiation by the author, which is negligible.

3.6. Non-continuum Effects

The general applicability of the Navier-Stokes equations is tied to the continuum regime, where the characteristic length L of the system is much larger than the free mean path λ_{mfp} of the gas molecules. The Knudsen number $Kn = \lambda_{mfp}/L$ can be utilized as a criterion for this condition. Cunningham [**120**] and then Knudsen and Weber [**121**] suggested a correcting factor that accounts for the reduction in drag when considering small particles. They suggested a form of the so called Cunningham factor:

$$C_C = 1 + Kn \left[\alpha + \beta \exp\left(-\gamma / Kn \right) \right] \tag{3.16}$$

with the corrected Stokes drag force

$$F_D = -\frac{3\pi\eta d u}{C_C} \tag{3.17}$$

α, β, and γ are coefficients determined by correlation of experimental data. Pioneering work in this regard was done by Millikan (also known for his precise quantification of the

elementary charge [**122**]) with his famous Millikan apparatus [**123**]. For oil droplets in air, the correlation

$$C_C = 1 + Kn \left[1.209 + 0.471 \exp\left(-\frac{0.596}{Kn} \right) \right] \tag{3.18}$$

was suggested. Many experiments were conducted over the years proposing various values of α, β, and γ, while varying influential parameters like gas temperature, pressure, particle surface nature, particle shape, gas composition, and droplet viscosity. Allen & Raabe [**124**] reevaluated and confirmed Millikan's work, improved Millikan's apparatus, and then investigated solid particles [**125**]. The following correlation for the Cunningham factor was suggested:

$$C_C = 1 + Kn \left[1.142 + 0.558 \exp\left(-\frac{0.999}{Kn} \right) \right] \tag{3.19}$$

Rader [**126**] reevaluated Millikan's work on the slip correction for various gases [**127**] and suggested for oil droplets in air:

$$C_C = 1 + Kn \left[1.209 + 0.440 \exp\left(-\frac{0.789}{Kn} \right) \right] \tag{3.20}$$

The author also stated that the slip correction correlation for air lies around the average of the other gases (Ar, He, H_2, CH_4, C_2H_4, i-C_4H_{10}, N_2O, CO_2), which implies that air constitutes an approximation for an unknown gas composition in this regard. Hutchins et al. [**128**] used modulated dynamic light scattering to measure the slip correction, which differs in nature from the apparatus used by previous researchers. Instead of the size of the solid particles, which was kept at 1 µm to 2 µm, the pressure was varied in order to obtain Knudsen numbers of 0.06 to 500. The following Cunningham factor was

suggested:

$$C_C = 1 + Kn\left[1.231 + 0.470\exp\left(-\frac{1.178}{Kn}\right)\right] \tag{3.21}$$

Kim et al. [**129**] investigated the slip correction explicitly for nanosized particles (20 nm to 100 nm) and for Knudsen numbers of 0.5 to 83. The following empirical correlation was proposed

$$C_C = 1 + Kn\left[1.142 + 0.505\exp\left(\frac{-0.936}{Kn}\right)\right] \tag{3.22}$$

for this parameter range (free molecular regime). Barber & Emerson [**130**] proposed an analytical applicable expression for the slip correction of a sphere in a gas:

$$\text{Total Drag} = -3\pi\eta du\left(\frac{1 + 4\frac{2-\sigma_u}{\sigma_u}Kn}{1 + 6\frac{2-\sigma_u}{\sigma_u}Kn}\right)$$

In this case, σ_u is the tangential momentum accommodation coefficient (TMAC). It describes which fraction of the gas molecules are reflected divisively (with momentum transfer) in contrast to reflected specularly (without momentum transfer) at the surface of the particles. This depends on the particle material as well as the gas. Moshfegh et al. [**131**] numerically investigated the incompressible slip flow regime past a spherical particle by imposing the analytical slip boundary condition from [**130**]. In contrast to previous slip corrections, a correlation is presented that depends on the Knudsen number and the Reynolds number:

$$\frac{F_D}{F_{D,Slip}} = 0.24Re + 2.00Kn + 0.98 \tag{3.23}$$

$$\text{for} \quad 0 \leq Re \leq 1 \quad \text{and} \quad 0.01 \leq Kn \leq 0.1$$

Non-continuum effects affect not only the drag between particle and fluid, but also the heat and mass transfer. While for drag this can be imagined as a velocity jump at the particle surface, for heat transfer it behaves like a temperature jump. Smoluchowski [**132**]

suggested a description for the temperature jump between gas and a wall in the slip flow regime:

$$T_g - T_w = \left(\frac{2\kappa}{\kappa+1}\right)\left(\frac{2-\sigma_T}{\sigma_T}\right)\left(\frac{Kn}{Pr}\right)\left(\frac{\partial T}{\partial n}\right) \tag{3.24}$$

Here, T_w is the dimensionless wall temperature, T_g the dimensionless temperature of the first layer of gas adjacent to the wall, κ the gas specific heat capacity ratio, σ_T the thermal accommodation coefficient, and $\partial T/\partial n$ is the normal temperature gradient at the wall. Some researchers have incorporated this approach recently. Mohajer et al. [**133**] conducted a numerical simulation for the heat transfer at microspherical particles in the slip flow regime. They found that, while the slip leads to a higher slip velocity, which in turn leads to a higher Nusselt number, the temperature jump, which goes along with the slip, leads to a decrease in the Nusselt number. For small temperature differences the former effect is dominant and for large temperature differences the later effect dominates. In that case, the gas properties need to be considered variable within the boundary layer. Liu et al. [**134**] also put an emphasis on the necessity to incorporate variable gas properties, substantiating the work of Mohajer et al. in their numerical study. Additionally, they found that the Nusselt number is higher when the gas temperature is higher than the particle temperature and compressibility effects are considered. Anbarsooz & Niazmand [**135**] conducted a numerical calculation in order to investigate the heat transfer characteristics of slip flows over solid spheres with $0 \leq Re \leq 50$, $0.7 \leq Pr \leq 7.0$, and $0 \leq Kn \leq 0.1$. The authors showed the influence of the above mentioned opposing effects of increased slip velocity and temperature jump. For small Prandtl numbers ($Pr \approx 0.7$ - gases), the Nusselt number decreases with increasing Knudsen numbers (temperature jump dominates). For the limiting case of $Re \to 0$ (pure conduction), the temperature

profile can be calculated analytically with

$$T = T_\infty - \frac{T_\infty - T_w}{1 + \frac{4\kappa}{\kappa+1}\frac{2-\sigma_T}{\sigma_T}\frac{Kn}{Pr}}\frac{R}{r} \tag{3.25}$$

with the corresponding Nusselt number

$$Nu = \frac{2}{1 + \frac{4\kappa}{\kappa+1}\frac{2-\sigma_T}{\sigma_T}\frac{Kn}{Pr}} \tag{3.26}$$

Ben-Ami & Manela **[136]** investigated under which conditions the Navier-Stokes-Fourier description of a pulsating sphere in a rarefied gas breaks down. And Yap & Sader **[137]** considered the combined effect of rarefaction and unsteady motion on a sphere.

As shown, the state of the art in this topic is already quite developed with many different exiting models, theories, and experiments. But each of them only covers small parameter ranges of the behaviour of particles in pulsating and oscillating flows, while an overarching framework is still missing. Often, only the motion of particles is considered, while the heat and mass transfer is omitted. In many works, the motion of the particles is considered an input parameter when the HMT is investigated. The same is true for flow patterns around the particles. In the following, an algorithm is presented in order to model the motion of particles in an oscillating flow by considering relaxation with a few broad range input parameters. The model employs two central dimensionless numbers, which help afterwards to transition directly to modelling the respective flow patterns and HMT to the single particle.

CHAPTER 4

Basic Assumptions and Considerations

The aim of this work is to model the influence of the few parameters listed in Table 4.1, with broad ranges, on the processes involved, from the basic motion of a single particle in Chapter 5, to the various flow patterns forming around it in Chapter 6, to the resulting heat and mass transfer to the particle in Chapter 7. The analytical model can be applied for a gaseous as well as a liquid environment. Each value combination of input parameters is related to a value of the Nusselt (Sherwood) number. In the first section, the input parameters and their ranges are discussed. This is followed by a discussion of the nature of pulsating and oscillating flows in PRs and in general, while several simplifications are introduced. Subsequently, several potential forces acting on the particle are considered or neglected in Section 4.3. Then, in Section 4.4, the analytic solution for the motion of the particle in a pulsating flow is derived with the Stokes drag model. The last simplification for enabling a harmonic analysis is applied by neglecting the transient part and transferring the solution to the oscillating flow case. Afterwards, in Section 4.5, the harmonic analysis is conducted with the Stokes drag model and a simple expression for the slip velocity is derived, which can also be interpreted graphically. An overview and brief discussion of the dimensionless numbers and their relations is presented in Section 4.6. Finally, the ϵ-Re plane is introduced, which functions as a uniting basis for many following considerations.

4.1. Input Parameters

The considered input parameters are listed in Table 4.1, with their investigated ranges, which are larger than the range of achievable process conditions in a pulsation reactor (see Table 2.1). This is by design, on the one hand, in order to capture effects outside of the current scope of pulsation reactors and to provide educated advice for further development on the one hand. On the other hand, this allows to expand the theoretical considerations to ultra sonic levitators (USL), which create process conditions similar to those of PRs. Additionally, the parameter range requirements for a pulsation reactor are so large that expanding them further does not add much complexity to the model, because many extreme cases need to be taken into account anyways. The input parameters can be fundamentally categorized into fluid related and particle related. These two categories are considered to be completely independent, hence this model utilizes one way coupling only (see Horwitz & Mani **[138, 139]** for two way coupling corrections). This assumption is discussed in more depth in Section 4.3. Many input parameters lead to secondary input parameters or can be exchanged for other parameters due to known dependencies. For example, under the assumption of an ideal gas **[140]**, a known gas temperature T enables the calculation of various other properties, such as the kinematic viscosity ν, the dynamic viscosity η, as well as the gas density ρ_g via power

Table 4.1. List of input parameters.

Matter	**Parameter**	**Symbol**	**Range**	**Unit**
Fluid	Velocity Amplitude	U_f	0 - 50	m/s
	Frequency	f	0 - 100000	Hz
	Temperature	T	300 - 1500	K
Particle	Diameter	d	10^{-3} - 10^{-9}	m
	Density	ρ_p	100 - 10000	kg/m^3

relations [**141**]:

$$\frac{\rho_g}{\rho_0} = \left(\frac{T}{T_0}\right)^{-1} \quad \frac{\eta_g}{\eta_0} = \left(\frac{T}{T_0}\right)^{n_\eta} \quad \frac{\nu_g}{\nu_0} = \left(\frac{T}{T_0}\right)^{n_{\eta+1}} \tag{4.1}$$

The reference values at $T_0 = 273\text{K}$, as well as the exponents, are material properties and are tabled in literature for various gases. Similar dependencies are known for liquids as well, but must be modelled for each liquid separately. Another example would be the exchange of the fluid velocity amplitude U_f for the pressure amplitude P, since they can be converted into each other via the speed of sound c in the fluid under the assumption of linear acoustics [**142**]:

$$P = \rho_f c U_f \tag{4.2}$$

4.2. Pulsating Flow

A pulsating flow can be defined as an oscillating flow superimposed on a non-vanishing steady velocity [**143**]. For the special case of a pulsating pipe flow, complete solutions were derived by Sexl [**144**], Womersley [**145**], and Uchida [**146**]. Following the lines of Hussain & Reynolds [**147**], any flow variable can be split into 3 components

$$f(x,t) = \bar{\zeta}(x) + \langle \zeta(x,\phi) \rangle + \zeta'(x,t) \tag{4.3}$$

with the temporally averaged (steady) part $\bar{\zeta}(x)$, the oscillating part $\langle \zeta(x,\phi) \rangle$, depending on the angle in the cycle ϕ, and a part that is statistically (randomly) fluctuating $\zeta'(x,t)$. This work assumes a spatially constant steady and oscillating part as well as a negligible fluctuating part in the dimensions of the particle. Figure 4.1 shows a typical velocity profile of pulsating pipe flow e.g. in the resonance tube of a pulsation reactor. The profile is dominated by the annular effect, discovered by Richardson [**148**], which describes an increased absolute flow velocity close to the tube walls and an even velocity profile in

the center (plug flow), in contrast to the parabolic velocity distribution of a pipe flow. The particle diameter d is much smaller than the diameter d_{tube} of the resonance tube

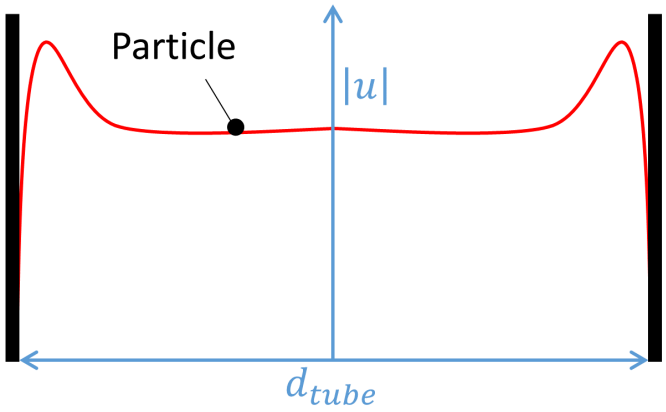

Figure 4.1. Pulsating flow velocity profile in a tube.

$d \ll d_{tube}$. This allows a simplification of the plug flow velocity profile of the fluid in the center of the pipe at the resolution of the particle to one-directional and, therefore, one-dimensional. Additionally, the pressure gradient and velocity gradient are considered harmonic. The validity of this assumption was demonstrated by experiment **[8]**, in which the pressure in a pulsation reactor was measured with a heat resistant microphone with a high sampling rate. As an example, one of the operation points is displayed in Figure 4.2. There, the measured pressure profiles in time for 4 measurement points along the tailpipe of a PR are shown. The pressure amplitude decreases along the tailpipe as predicted by Helmholtz resonator theory **[2]**. For the sake of comparison, an ideal harmonic pressure profile is plotted on top of the measured profiles. It can be seen that they do not differ significantly, even though they become less harmonic towards the end of the tailpipe. The total harmonic distortion (THD) **[149]**

$$THD_F = \frac{\sqrt{\sum_{n=2}^{\infty} P_n^2}}{P_1} \tag{4.4}$$

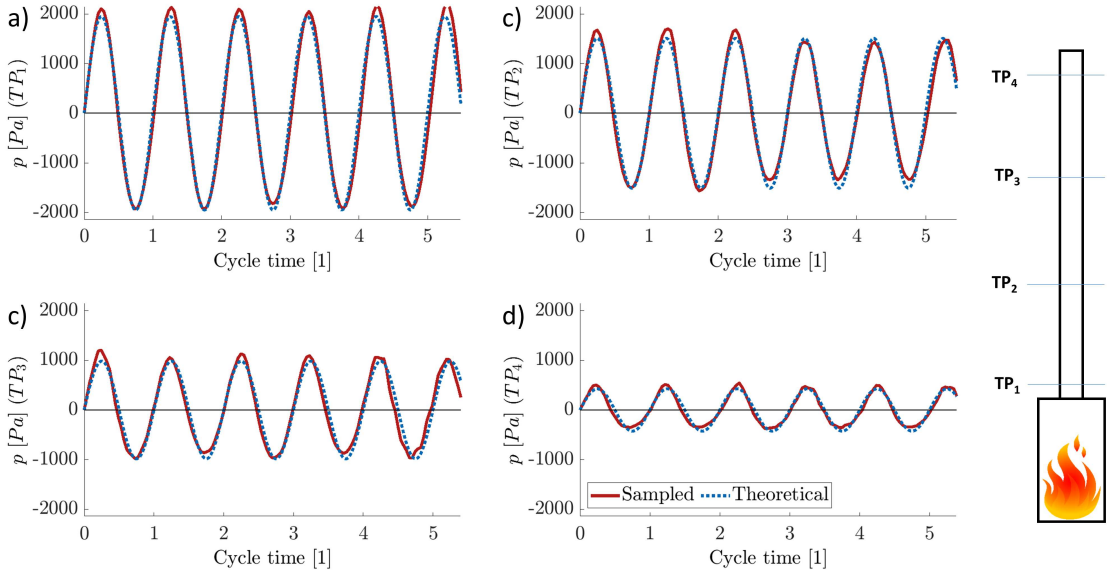

Figure 4.2. Comparison of an artificially generated fundamental with measured pressure data at 4 different points along the tailpipe ($TP_1 - TP_4 \longrightarrow a) - d)$) at a PR.

was calculated with the fundamental order of the pressure amplitude P_1 and the higher harmonics P_n for various operation points (different fuel and air intakes). It was demonstrated that the THD never exceeded 20% at any point, even if the pulsation was at its stability limit [**8**]. In the parameter areas where a PR is usually operated, the THD is significantly smaller. The pressure profile can be converted into the velocity profile and the velocity amplitude U_f can be calculated with

$$U_f = \frac{P}{\rho_f c} \tag{4.5}$$

Therefore, the pressure curve and the oscillating flow velocity can be considered harmonic. This assumption is also often applied in literature for USLs [**86**, **87**]. Hence, the flow velocity of a one-dimensional, harmonic, pulsating flow can be described as:

$$u_f(t) = \bar{u}_f + U_f \cos \omega t \tag{4.6}$$

with the steady mean velocity component $\bar{u}_f = f \int_t^{t+1/f} u_f(t)\ dt$, the fluid velocity amplitude U_f, and the angular pulsation frequency $\omega = 2\pi f$.

4.3. Forces on the Particle

Several (potential) forces are acting on a single particle in a pulsation reactor [**150**]. In the following they are each examined and neglected or taken into account:

Gravity G

Gravity is a force in the direction of the gravitational acceleration g and can be calculated via $G = (1 - 1/\gamma)g$ with the density ratio between fluid and particle $\gamma = \rho_p/\rho_f$. The density ratio plays a vital role in many following considerations and is discussed in length in Section 5.2. In case the terminal settling velocity $U_{set,t} = G\tau$, calculated with the characteristic particle relaxation time $\tau = \gamma d^2/(18\nu)$, is much smaller than the fluid velocity amplitude $U_{set,t} \ll U_f$, gravity can be neglected [**151**]. Most pulsation reactors are constructed horizontally [**6**], and if $U_{set,t} \gg U_f$ holds true, the particle would sink to the bottom of the reactor and then deposit there, which would be an undesirable configuration in the first place. Also, the limit case of $U_{set,t} \approx U_f$, where particles are dragged along in the fluid stream as they bounce off the bottom of the tube, is not considered. Therefore, gravity is neglected in this work.

Saffman Force $\mathbf{F_S}$

The shear induced lift force investigated by Saffman [**152**] that can be calculated via the expression $3.084 U_x \nu/(\gamma d)\sqrt{|dU_f/dy|/\nu}$ acts on particles in shear flows, and should be taken into account close to walls when considering deposition. Here, dU_f/dy is the fluid velocity gradient perpendicular to the main flow direction, while U_x is the slip velocity between particle and fluid in the main

flow direction. The slip velocity is one of the main concerns of this work and is mainly discussed in the next section and Section 5.1. In this work, only the flow in the center of the tube with plug flow character is considered, as derived in Section 4.2. Therefore, this force is neglected in this context. Nevertheless, in a PR, the Saffman force can help or hinder particle depositing, depending on the phase lag of the particle [**153**].

Thermophoretic Force $\mathbf{F_{therm}}$

This force is associated with temperature gradients in the fluid and can be calculated with $F_{therm} = -(\eta_{therm}/m_p)\nabla \ln(T)$ and the thermophoretic force coefficient $\eta_{therm} = 2.34(3\pi\eta\nu d)(\lambda_r + 4.36Kn)/[(1+6.84Kn)(1+8.72Kn+\lambda_r)]$. Here, $\lambda_r = \lambda_f/\lambda_p$ is the thermal conductivity ratio between the fluid and the particle [**154**]. The dimensionless Knudsen number $Kn = \lambda_{mfp}/d$ is the ratio between the mean free path of gas molecules and the particle diameter and is treated more in depth in Section 5.6. The thermophoretic force acts against the temperature gradient, towards the cooler medium. It can be substantial for very small particles over very small dimensions, but does not need to be taken into account in a free stream, which the flow in a PR can be considered as for small particles.

Electrostatic Force $\mathbf{F_E}$

This force requires a charged particle and an electric field and can be calculated with $F_E = 3q^2/8\pi^2\epsilon_0\rho_p d^3 y^2$. Here, q is the charge on the particle and ϵ_0 ($8.854\,187 \times 10^{-12}\,\mathrm{F\,m^{-1}}$) is the electric permittivity of vacuum, which is close to air. While particles can get charged by many processes, including mirror

charging, interacting with other particles, etc., the charges and occurring electric fields in a pulsation reactor are usually small and can be neglected.

Collision with other particles

This phenomenon can not be attributed to a force in the convectional sense, but rather the exchange of momentum. Still, it is an important aspect enabling change in particle velocities, sintering of particles, or charging as mentioned in the previous paragraph. Taking the usual dimensions of a PR into account with the usual material throughput, as listed in Table 2.1, mean particle distances of around $300d$ can be expected. This is enough to exclude particle-particle interaction and treat single particles on an individual level **[155]**.

Drag Force $\mathbf{F_D}$

Particle drag is a force resulting from the friction between a particle and a surrounding medium when the particle moves at a different velocity as the medium. It is modelled in this work and is covered substantially in the next section and Section 5.1.

Inertia $\mathbf{F_I}$

The inertial force is acting against a forced motion of any body and can be described in the case of a particle as $F_I = (\pi/6)\rho_p d^3 a_p$, with the acceleration of the particle a_p. Similar to drag, it is applied in this work in the next section and Section 5.1.

An overview of the forces acting on a particle which are included and neglected in this work is shown in Figure 4.3. The two forces considered in this work are the particle

drag and the inertia of the the particle which are in a constant equilibrium state. This equilibrium state is the starting point for deriving the motion of the particle in the next section.

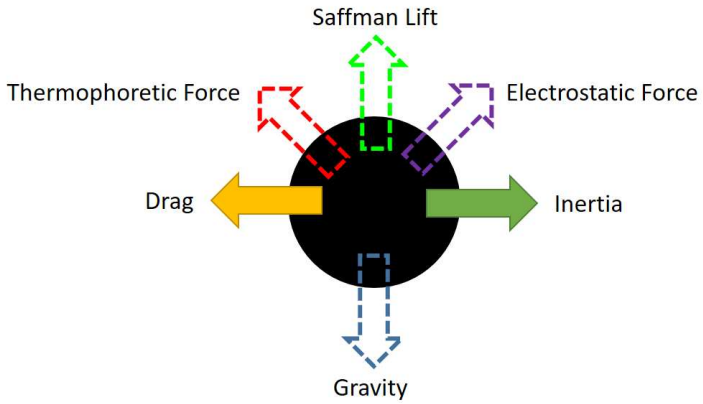

Figure 4.3. Various forces acting on a single particle. Forces with filled arrows are included in this work and forces with empty arrows are neglected.

4.4. Motion of Particles - Stokes Solution

The slip velocity

$$u(t) = u_f(t) - u_p(t) \tag{4.7}$$

between the fluid velocity $u_f(t)$ and the particle velocity $u_p(t)$ is the central quantity for many particle considerations. Modelling this quantity is achieved by calculating the actual particle velocity for a known fluid velocity and then deriving the instantaneous slip velocity via Equation 4.7. Starting point is the constant force equilibrium on the particle, while the main forces in many cases are drag and inertia, as laid out in the previous section. In a first step, the one dimensional particle motion will be derived specifically with the Stokes drag model and then generalized for other drag models presented later, in Section 5.1. The Stokes drag model is derived from the Navier-Stokes equations (NSEs) by asymptotic analysis for negligible small inertial and dominating viscous forces in the

fluid **[156]**. The ratio of inertial to viscous forces is expressed via the Reynolds number $Re = ud/\nu$. Even though the Stokes model is derived for the limit case of $Re \to 0$, it is commonly considered valid up to $Re = 1$. The drag force $F_{D,Stk}$ predicted by the Stokes model and the inertial force of a spherical particle F_I

$$F_{D,Stk} = 3\pi\eta d u \tag{4.8}$$

$$F_I = \rho_p \frac{\pi}{6} d^3 a \tag{4.9}$$

together with the fluid velocity expressed in Equation 4.6, lead to the ordinary differential equation (ODE) of the force equilibrium

$$\dot{u}_p + \frac{1}{\tau} u_p = \frac{1}{\tau} \left[\bar{u}_f + U_f \cos\left(\omega t + \phi_0\right) \right] \tag{4.10}$$

A detailed derivation and solution of this ODE can be found in Appendix A. Various parameters of the particle and the surrounding fluid are summarised in the relaxation time $\tau = \rho_p d^2/18\eta$, which are input parameters from Table 4.1 or can be calculated from input parameters via Relations 4.1. These properties do not depend on the motion of the particle and are therefore considered to be constant. This can also be assumed for the angular frequency ω of the pulsating flow, while the product of τ and ω merges all constant influential parameters of the problem to a single dimensionless number, the oscillation Stokes number $Stk = \omega\tau$ **[157]**. The relaxation time τ indicates how fast a particle can adapt to changing flow conditions, while the angular frequency ω indicates how fast the flow conditions change. Hence, the Stokes number indicates how well a

particle can follow the changing flow. ODE 4.10 can be solved to

$$u_p(t) = \underbrace{\left[u_0 - \bar{u}_f - \frac{U_f}{1+Stk^2}\left[\cos(\phi_0) + Stk\sin(\phi_0)\right]\right] e^{-\frac{t}{\tau}}}_{\text{transient}} + \underbrace{\bar{u}_f + \frac{U_f}{1+Stk^2}\left[\cos\left(\omega t + \phi_0\right) + Stk\sin\left(\omega t + \phi_0\right)\right]}_{\text{resident}} \tag{4.11}$$

and the slip velocity can be calculated with

$$\begin{aligned} u(t) &= u_f(t) - u_p(t) \\ &= \underbrace{\left[\bar{u}_f - u_0 + \frac{U_f}{1+Stk^2}\left[\cos(\phi_0) + Stk\sin(\phi_0)\right]\right] e^{-\frac{t}{\tau}}}_{\text{transient}} \\ &+ \underbrace{U_f\frac{Stk}{1+Stk^2}\left[Stk\cos\left(\omega t + \phi_0\right) - \sin\left(\omega t + \phi_0\right)\right]}_{\text{resident}} \end{aligned} \tag{4.12}$$

Equations 4.11 and 4.12 are divided into a transient and a resident part. The transient part describes how the particle is brought up to the resident particle velocity (not the fluid velocity), while the resident part describes how the particle behaves in the continuously oscillating flow, as shown in Figure 4.4. The transient part diminishes, while time progresses:

$$\lim_{t\to\infty}\left(\left[\bar{u}_f - u_0 + \frac{U_f}{1+Stk^2}\left[\cos(\phi_0) + Stk\sin(\phi_0)\right]\right] e^{-\frac{t}{\tau}}\right) = 0 \tag{4.13}$$

After $t = 3\tau$, the transient part has shrunk to 5% of its initial value and is considered negligible. It is dominated by the difference of the initial particle velocity u_0 and the mean fluid velocity $\bar{u}_f$. Furthermore, the time in the cycle of the oscillating fluid velocity ϕ_0 when the particle is injected into the flow is crucial. After the decay of the transient part, hence after $t = 3\tau$, the motion of the particle becomes repetitive, so further constraints

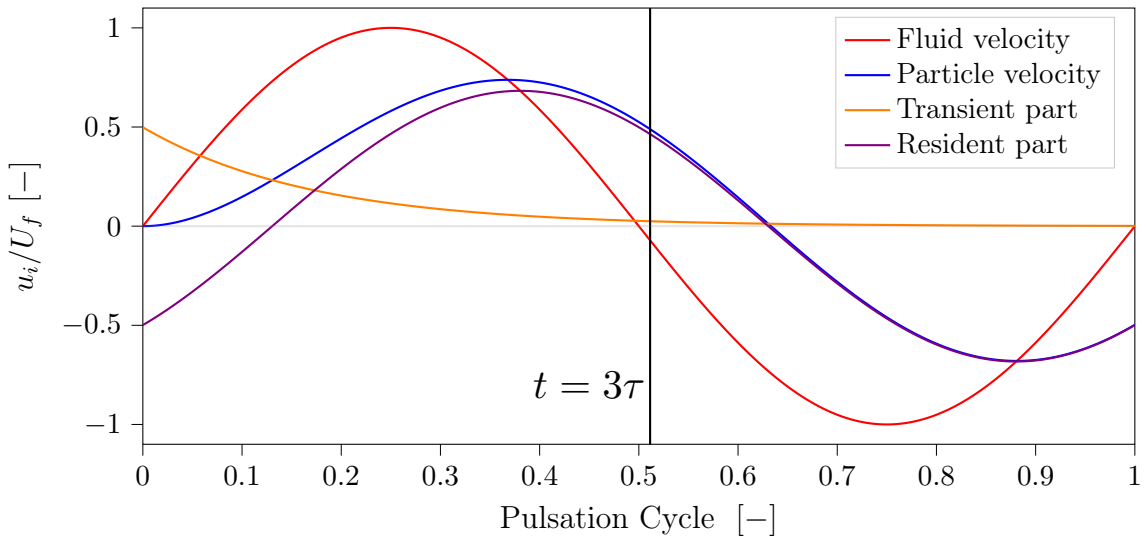

Figure 4.4. Initial particle motion split into resident and transient part. After $t = 3\tau$ the transient part has shrunk to 5% of its initial value. All velocities are in relation to fluid amplitude U_f. $Stk = 1; \phi_0 = 0; u_0 = \bar{u}_f = 0$ m/s.

and simplification can be applied:

$$u(t > 3\tau) \approx U_f \frac{Stk}{1 + Stk^2} \left[Stk \cos(\omega t + \phi_0) - \sin(\omega t + \phi_0) \right] \tag{4.14}$$

A display of this motion behavior can be seen in Figure 4.5, where it is shown that the particle will perform an oscillating motion with the same frequency as the fluid, but with smaller amplitude and a phase shift, which both depend on the Stokes number Stk. In this work, only the resident part of the particle motion ($t > 3\tau$) is considered, which enables harmonic, time independent investigations. Nevertheless, the application of the Stokes drag model with Equation 4.12 delivers an educated, conservative guess of the slip velocity for the consideration of transient effects, even for $Re > 1$ [**151**, **158**]. Since USLs feature a standing sound wave and the particles can be considered fixed in place, no transient effects occur in the first place.

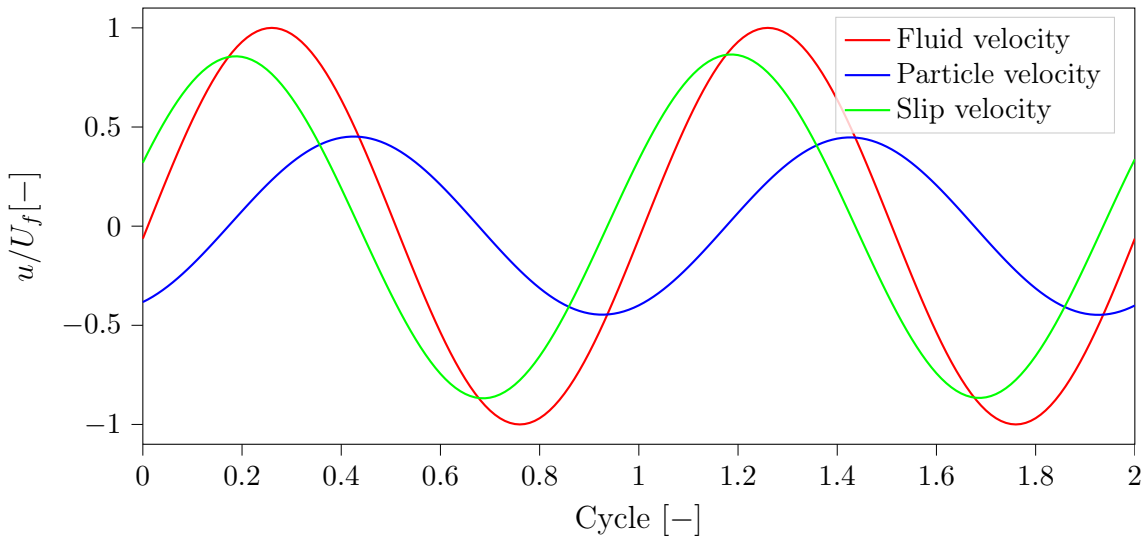

Figure 4.5. Repetitive motion of a particle in an oscillating flow, calculated analytically with the Stokes drag model. All velocities are in relation to the fluid velocity amplitude U_f.

4.5. Harmonic Analysis

Not only can the fluid velocity be modelled as harmonic, as shown in Section 4.2, but so can the particle velocity and the slip velocity, as long as $t > 3\tau$, as laid out in the previous section and visualized in Figure 4.5. This means that each velocity is defined by an amplitude, frequency, and phase shift. The phase shift is only important for describing the timely relations between the velocities and is therefore neglected in the following considerations. As stated in Section 4.4, the slip velocity is the most important quantity for all following considerations. Since the slip velocity oscillates with the same frequency as the fluid, which is an input parameter, this quantity is already known, leaving the slip velocity amplitude as the only undetermined quantity needed in order to describe the slip velocity. The amplitude of the slip velocity oscillation is the extreme value of Equation 4.14 and is solely dependent on the Stokes number and the

fluid velocity amplitude, which can be calculated directly from input parameters:

$$\frac{U}{U_f} = \frac{1}{\sqrt{1 + \frac{1}{Stk^2}}} \tag{4.15}$$

Equation 4.15 is displayed in Figure 4.6. For small Stokes numbers $Stk \ll 1$, the ratio of slip velocity amplitude to fluid velocity amplitude is equal to the Stokes number itself, while for large Stokes numbers $Stk \gg 1$ the ratio becomes unity. These phenomenon are labeled fast relaxation limit (FRL) and slow relaxation limit (SRL) in this work, and are covered in more depth in Section 5.3. The fluid velocity amplitude U_f, particle

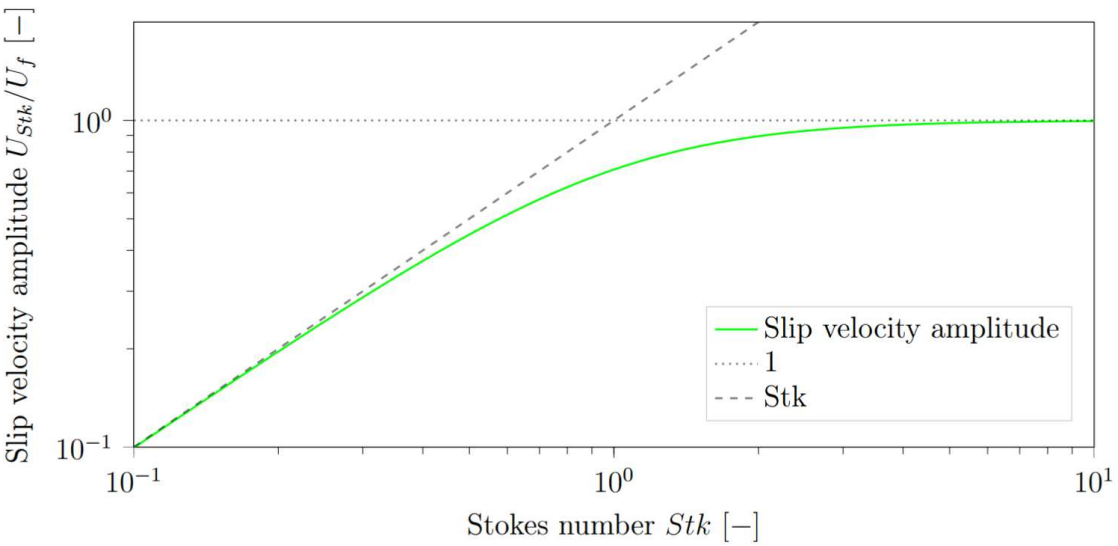

Figure 4.6. Plot of Equation 4.15. Slip velocity amplitude in relation to fluid velocity amplitude in respect to the Stokes number Stk.

velocity amplitude U_p, and relative velocity amplitude U can be expressed as vectors, which form a right triangle as displayed in Figure 4.7. It becomes obvious that many geometrical relations can be applied to this problem, such as trigonometric functions and the Pythagorean theorem. Furthermore, the internal angle ϕ_p between the fluid velocity amplitude vector and the particle velocity amplitude vector indicates the phase shift between fluid velocity oscillation and particle velocity oscillation. It is very similar

for the the internal angle ϕ between the fluid velocity amplitude vector and the relative velocity amplitude vector, but in this case it is the negative phase shift between fluid velocity oscillation and relative velocity oscillation. The relations in Figure 4.7 are valid at any instance in time, independent of the applied drag model.

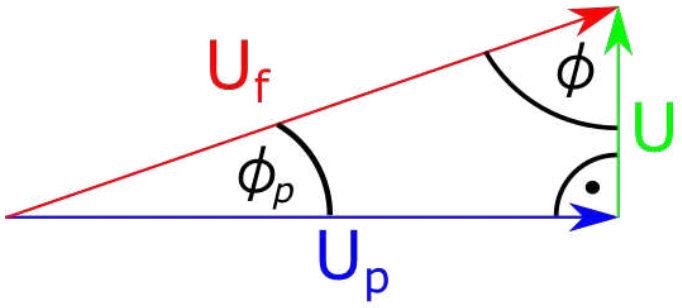

Figure 4.7. Vectorial representation of fluid velocity amplitude U_f, particle velocity amplitude U_p, and relative velocity amplitude U, including phase shift angles in reference to the fluid oscillation of the particle velocity ϕ_p and relative velocity ϕ.

4.6. Dimensionless Numbers

The large range of considered input parameters in general and the exhaustive range of considered particle sizes in particular bring the necessity to apply different sub-models for drag, flow patterns, as well as heat and mass transfer. Many different states and regimes are considered, often ranging from one extreme to the other. Dimensionless numbers are the primary source of criteria to evaluate phenomenon qualitatively [**159**], especially in fluid dynamics, and then choose the appropriate sub-models accordingly. An overview of all the utilized dimensionless numbers in this work can be found in Table 4.2. The Reynolds number, as introduced in Section 4.4, is the central dimensionless number and important in most fluid dynamic considerations. In the case of oscillating flows, the oscillation Reynolds number $Re = Ud/\nu$ is utilized, which is calculated with the slip velocity amplitude instead of the instantaneous slip velocity. The oscillation Reynolds

number is paired with the amplitude parameter $\epsilon = A/d$ with the displacement amplitude $A = U/\omega$, as laid out in Chapter 3. It describes how far the particle oscillates in relation to its own diameter. This dimensionless number is important in order to determine the type of boundary layer that forms around the particle, as discussed in Chapter 6. In some literature, the Strouhal number $Sr = 1/\epsilon$ is used, which is the reciprocal amplitude parameter. The Womersley number $Wo^2 = Re/\epsilon = d^2/\delta^2$ sets the particle diameter in relation to the boundary layer thickness $\delta = \sqrt{\nu/\omega}$. It is primarily utilized in this work as an indicator if the flow can be considered quasi steady, as described in Section 5.1. The Streaming Reynolds number $Re_S = Re\epsilon = U^2/(\omega\nu)$ provides an indication as to if the second order effect of Steady Streaming needs to be taken into consideration, while taking the place of the classic Reynolds number, when dealing with this phenomenon, as laid out in Chapter 6. The oscillation Stokes number was already introduced in Section 4.4 and is discussed in more depth in Section 5.3. The Knudsen number $Kn = \lambda_{mfp}/d$ sets the mean free path λ_{mfp} of gas molecules in relation to the particle diameter. Small Knudsen numbers allow for the application of continuum fluid dynamics, while large Knudsen numbers require the consideration of non-continuum effects. Large Knudsen numbers are connected to small particle sizes ($d \leq 10^{-}6$) in gases, which is utilized in Sections 5.6 and 7.7. The Mach number $Ma = U_f/c$ sets the velocity of the fluid in relation to the speed of sound in the fluid. Small Mach numbers allow for the treatment of gas flows as incompressible, which often reduces the complexity of the flow models. In this work, all considered flows are treated incompressible. The ratio $\gamma = \rho_p/\rho_f$ between the density of the particle ρ_p and the density of the fluid ρ_g is a central quantity for the consideration of drag models in Section 5.1 and particle relaxation in Section 5.3. Some of the discussed dimensionless numbers have multiple labels or can be expressed by a combination of other dimensionless numbers. Figure 4.8 displays the important relations between some of the

Table 4.2. Overview of dimensionless numbers.

	Phenomenon	**Dimensionless number**	$\ll 1$	≈ 1	$\gg 1$
Fluid dynamics	Flow regime	Reynolds number $Re = \frac{Ud}{\nu}$	Creeping flow	Transition regime	Potential flow
	Flow pattern	Amplitude parameter $\epsilon = \frac{U}{\omega d}$	Steady Streaming	Transition regime	Classic boundary layer
	Quasi-steady flow	Womersley number $Wo^2 = \frac{d}{\delta}$	Quasi-steady flow	Transition regime	Unsteady flow
	Steady Streaming	Streaming Reynolds number $Re_S = Re\ \epsilon$	Steady Streaming negligible	Transition regime	Steady Streaming dominant
	Particle relaxation	Stokes number $Stk = \frac{\omega \rho_f d^2}{18\eta}$	FRL	Relaxation	SRL
	Flow description	Knudsen number $Kn = \frac{\lambda}{d}$	Continuum flow	Slip flow	Free molecular flow
	Incompressible flow	Mach number $Ma = \frac{U_f}{c}$	Subsonic flow	Transition regime	Supersonic flow
	Density ratio	$\gamma = \frac{\rho_p}{\rho_f}$	fluid denser	approx. equal	particle denser
Heat and mass transfer	Thermal boundary layer thickness	Prandtl number $Pr = \frac{\nu}{\alpha}$	thermal diffusivity dominant	approx. equal	momentum diffusivity dominant
	Mass boundary layer thickness	Schmidt number $Sc = \frac{\nu}{D}$	mass diffusivity dominant	approx. equal	momentum diffusivity dominant
	Heat transfer	Nusselt number $Nu = \frac{hd}{k}$	convective heat transfer dominant	approx. equal	conductive heat transfer dominant
	Mass transfer	Sherwood number $Sh = \frac{hd}{D}$	convective mass transfer dominant	approx. equal	diffusion dominant

dimensionless numbers used in this work. After this brief introduction of the important dimensionless numbers for the motion of particles in oscillating flows and the associated flow pattern around the particle, additional dimensionless numbers for the description of the resulting HMT at the particle are introduced. The Prandtl number $Pr = \nu/\alpha$ sets the momentum diffusivity in relation to the thermal difussivity α. Another interpretation is the relation between the momentum boundary layer thickness and the thermal boundary layer thickness. Together with the Reynolds number, the Prandtl number can be used to determine the Nusselt number $Nu = hd/k$ in steady flows, as laid out in Section 7.3. The Nusselt number is calculated with the convective heat transfer coefficient h and the thermal conductivity k and sets the conductive heat transfer in relation with the

convective heat transfer. Overall it can be used as a criterion for the intensity of the occurring heat transfer. When dealing with mass transfer instead of heat transfer, the counterpart to the Prandtl number is the Schmidt number $Sc = \nu/D$ and the counterpart to the Nusselt number is the Sherwood number $Sh = h_m d/D$. The Schmidt number sets the momentum diffusivity in relation to the mass difussivity D, while the Sherwood number sets the convective mass transfer, expressed by the convective mass transfer coefficient h_m, in relation to the occurring diffusion. The Sherwood number is utilized in Chapter 7 alongside the Nusselt number.

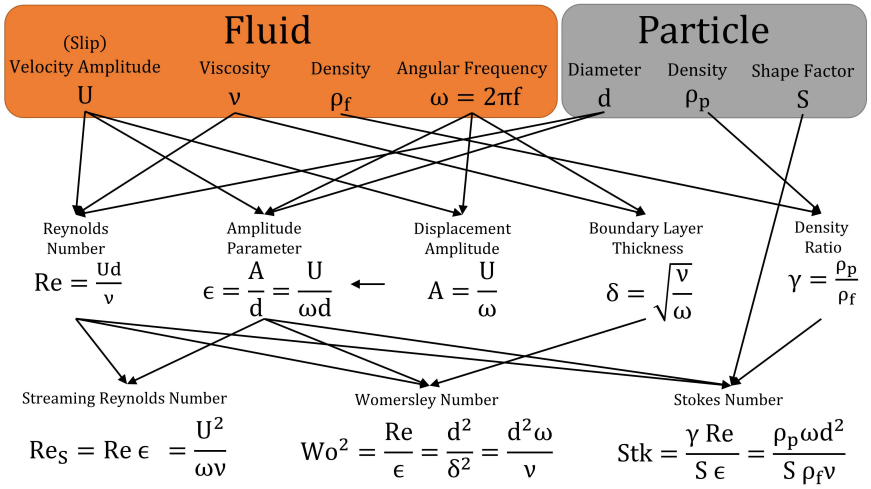

Figure 4.8. Dependencies and relations between the central dimensionless numbers in oscillating multi-phase flow.

4.7. The ϵ-Re Plane

In case the particle is fixed in position (or the particle executes harmonic oscillations in a fluid at rest), the interaction between the fluid and the particle as well as the resulting flow state is defined by two dimensionless numbers: the oscillation Reynolds number Re and the amplitude parameter ϵ, as introduced in the previous section. In case particle relaxation needs to be considered, as described in Section 5.3, the flow state

also depends on the density ratio γ, which acts as a parameter. Reynolds number and amplitude parameter span a plane in which all flow states can be pinpointed, as shown in Figure 4.9. The bisectors of this plane are the Womersley number $Wo^2 = Re/\epsilon$ [**145**]

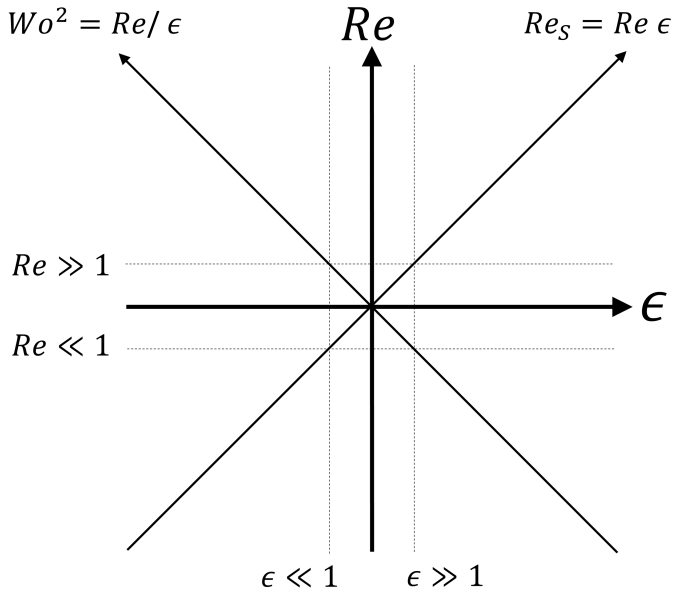

Figure 4.9. ϵ-Re plane by Heidinger et al. [**160**] in which all flow states of a single particle in an oscillating flow can be defined.

and the Streaming Reynolds number $Re_S = \epsilon\ Re$ [**61**]. The ϵ-Re plane was introduced by Wang [**161**] and then adopted by Chong et al. [**162**]. In this work, it functions as a uniting basis for the discussion of particle motion (Section 5.1), slip velocity (Section 5.2), particle relaxation (Section 5.3), flow patterns (Chapter 6), and HMT (Chapter 7). For this endeavour, the axis of the plane are sometimes expressed in the decimal logarithmic scale. This has several advantages and disadvantages. Advantages are that the plane now has its origin at $O(0, 0)$, enabling a direct use of Euclidean vectors without the need of any origin transformation, as discussed in Section 5.4. Additionally, complex vectors can be used in order to describe points in the plane and perform vector calculations. Disadvantages are the need to transform into the logarithmic scale and back afterwards in order to conduct calculations, as well as the lack of relatability to the size of the

treated quantities. From here on, the ϵ-Re plane is simply referred to as 'plane' in this context.

CHAPTER 5

Motion of the Particle

The particle motion in a one-dimensional pulsating flow was derived and discussed in Section 4.4 with the simple drag model by Stokes. Stokes has a comparably small range of validity of $Re \leq 1$ and not all flow states resulting from the parameter ranges of Table 4.1 can be modelled by it. Therefore, in Section 5.1 an investigation will be carried out to discern which drag models can be utilized in various areas of the plane introduced in Section 4.7 in order to cover large parts of it. Subsequently, the resulting slip velocity amplitude is determined in Section 5.2, which is the first target quantity as discussed in Section 4.2. After this, particle relaxation in one-dimensional oscillating flows is generalized in Section 5.3. Utilizing the derived relaxation limits, Section 5.4 provides a crude way of navigating the plane on the basis of a sensitivity analysis. This is followed by an investigation in Section 5.5, on the limits in which the simple Stokes model differs insignificantly from other drag models. If the Stokes model differs insignificantly from another model, even outside of its perceived range of validity, it can be applied in the respective parameter range as a substitution. Section 5.6 lays out how the plane can be adapted for small particles, for which continuum flow mechanics provide insufficient descriptions. Chapter 5 is then concluded by a short summary in Section 5.7.

5.1. Drag Models

An important step is choosing the appropriate drag model for the prevalent flow regimes around the particle. There are several cases to consider. A major distinction to draw is between a flow that can be considered steady compared with an unsteady flow.

The main criterion for differentiating is whether the boundary layer $\delta = \sqrt{\nu/\omega}$ is larger or smaller than the particle itself. This phenomenon is expressed by the Womersley number $Wo^2 = d^2/\delta^2$ [**145**]. The Womersley number is sometimes also referred to as Stokes number [**163**] or frequency parameter M^2 [**76**] in literature. If $Wo^2 \ll 1$, the flow can be considered steady [**43**]. In case the Reynolds number is also smaller than unity $Re < 1$, the viscous forces dominate and creeping flow can be assumed. This assumption leads to mathematical simplifications expressed via the Stokes drag model presented in Section 4.4. If $Wo^2 \ll 1$, while the Reynolds number exceeds the validity range of the Stokes model $Re > 1$, the flow can still be considered steady, but a drag model with a higher range of validity regarding the Reynolds number has to be applied. In this case, the Schiller & Naumann (SN) model [**164**] (see also [**165**]) can be used, which is applied widely in literature [**139**, **166**, **167**]. It differs in nature from the Stokes model in two important aspects. On the one hand, it is an empirical model derived via the correlation of experimental data, rather than being derived from the NSEs by omitting inertial forces. On the other hand, applying the drag model by Schiller & Naumann leads to a non-linear motion ODE, which can only be solved numerically. In the opposite case of $Wo^2 \gg 1$, the drag model by Landau & Lifshitz [**43**] can be applied, as long as the displacement amplitude $A = U/\omega$ is smaller than the particle diameter itself. This ratio is expressed by the amplitude parameter $\epsilon = A/d$. The drag model by Landau & Lifshitz is derived by linearizing the NSEs around small oscillation amplitudes $\epsilon \ll 1$. In case neither $Wo^2 \ll 1$ nor $Wo^2 \gg 1$, but $Re < 1$, the drag model by Basset [**16**] can be considered valid, which is explicitly derived for unsteady flow conditions and was introduced in Chapter 3. It is an extension of the Stokes model that, besides pure drag, also considers added mass and the pressure gradient. Additionally, the "history" of the fluid is factored in by an additional, theoretically derived term. In this work, only the

steady state is considered and therefore the lower boundary of the history integral t_0 is set to $-\infty$. The Reynolds number Re, the Womersley number Wo^2, and the amplitude parameter ϵ are the central dimensionless numbers used to characterise oscillating flows, though they are not independent from each other. The ϵ-Re plane, as introduced in Section 4.7, can be utilized in order to graphically distinguish ranges of validity for drag models, as seen in Figure 5.1. An undefined area is recognizable where none of the above models are valid from a mathematical point of view. Here, the empirical correlations by Odar & Hamilton **[34]**, as introduced in Chapter 3, can be applied or the NSEs need to be solved numerically. The models by Stokes and Landau & Lifshitz

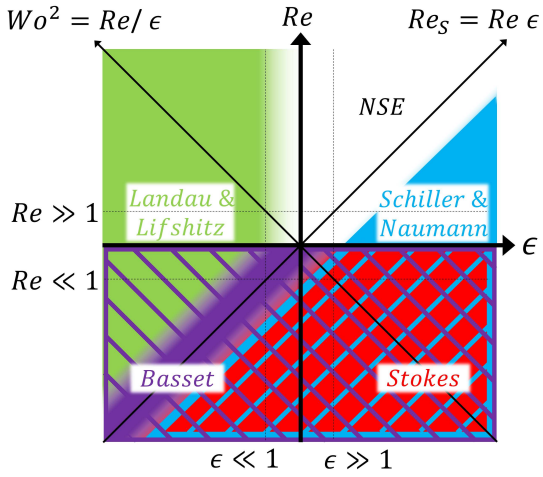

Model	**Range of validity**	**Significant features**
Stokes	$Re < 1$ $Wo^2 \ll 1$	linear/ asymptotic analysis
Schiller& Naumann	$Wo^2 \ll 1$ $Re < 1000$	non-linear/ empiric
Basset	$Re < 1$	linear/ half-empiric/ asymptotic analysis
Landau& Lifshitz	$Wo^2 \gg 1$ $\epsilon \ll 1$	linear/ asymptotic analysis

Figure 5.1. Models considered for various combinations of Reynolds number Re, amplitude parameter ϵ, and Womersley number Wo^2. **left:** Various drag models displayed in the ϵ-Re plane. The frames indicate the limits of validity, while the colored areas mark the preferable model. **right:** Various drag models with their limits of validity and significant features.

are derived from the NSEs by asymptotic analysis for extreme conditions and achieving mathematical simplification. Those extreme conditions are $Re \ll 1$ or $\epsilon \ll 1$. As long as the NSEs can be considered valid and the extreme conditions are met, these models can also be considered valid, although it is often not clear when these conditions are met, as pointed out in Section 5.5. In contrast, empiric models like Basset, Schiller & Naumann

and Odar & Hamilton are approximations of relations retrieved by fitting regressions to experimental data. Therefore, they inherently provide less theoretical reliability due to the multiple sources of error in the model building process. This is also highlighted by the vast amount of different, yet competing empiric correlations for the same parameter areas [**168**], as pointed out in Section 3.2. Additionally, Stokes and Landau & Lifshitz, as well as Basset, lead to linear and therefore analytically solvable differential equations of particle motion. Hence, they grant more mathematical accessibility and are easier to implement than non-linear models. A detailed derivation and solution of the motion ODE with the Landau & Lifshitz model can be found in Appendix B, while the solutions to the ODEs for the other models are well known in literature [**21**]. In parameter areas where multiple models are valid, linear models are preferable to non-linear models and asymptotic analysis is preferable to empiric models. A good treatise on drag model validity ranges in sound waves can be found with Temkin & Leung [**169**]. In Figure 5.1, the validity limits of the models are indicated by frames, while the preferable models are indicated by the areas in various colours. This classification was conducted along the arguments laid out above. The limits of validity for the discussed drag models and their main features are presented in Table 5.1.

5.2. Slip Velocity Amplitude

Each drag model from Table 5.1 expresses the drag force on the particle differently. If the algorithm presented in Section 4.4 is applied to the remaining drag models, an expression for the slip velocity amplitude can be found, as listed in Table 5.1. In each case, the slip velocity amplitude U, normalized with the fluid velocity amplitude U_f, is solely dependent on the Womersley number and the density ratio, while the Cunningham factor C_C is set to 1 for now and addressed later in Section 5.6. The Womersley number $Wo^2 = Re/\epsilon$ can be expressed with the amplitude parameter and the oscillation Reynolds

Table 5.1. Normalized slip velocity amplitude U/U_f for several drag models depending on the Womersley number Wo^2 and the density ratio γ.

Name	**Drag force F_D**	**Velocity ratio U/U_f**
Stokes	$\frac{3\pi\eta du}{C_C}$	$\left[1+\left(\frac{18}{Wo^2\gamma C_C}\right)^2\right]^{-1/2}$
Schiller & Naumann	$\frac{3\pi\eta duSN}{C_C}$	$\left[1+\left(\frac{18\ SN}{Wo^2\gamma C_C}\right)^2\right]^{-1/2}$ $SN=1+0.158Re^{2/3}$
Basset	$\frac{3\pi\eta du}{C_C}-\frac{\pi}{6}d^3\frac{\partial p}{\partial x}+\frac{\pi}{12}d^3\rho_f\frac{du}{dt}$ $+\frac{3}{2}d^2\sqrt{\pi\rho_f\eta}\int_{t_0}^{t}\frac{du/dt}{\sqrt{t-t'}}dt'$	$\left[1+\frac{1}{(1+f_1)^2-f_2^2}\right]^{-1/2}$ $f_1=\frac{\left[(\gamma+0.5)+\frac{9}{\sqrt{2}Wo}\right][1-\gamma]}{\left[\frac{18}{Wo^2C_C}+\frac{9}{\sqrt{2}Wo}\right]^2+\left[(\gamma+0.5)+\frac{9}{\sqrt{2}Wo}\right]^2}$ $f_2=\frac{\left[\frac{18}{Wo^2C_C}+\frac{9}{\sqrt{2}Wo}\right][1-\gamma]}{\left[\frac{18}{Wo^2C_C}+\frac{9}{\sqrt{2}Wo}\right]^2+\left[(\gamma+0.5)+\frac{9}{\sqrt{2}Wo}\right]^2}$
Landau & Lifshitz	$\frac{3\pi\eta du}{C_C}\left(1+\frac{d}{2\delta}\right)$ $+\frac{3}{4}\pi d^2\sqrt{\frac{2\eta\rho}{\omega}}\left(1+\frac{d}{9\delta}\right)\frac{du}{dt}$	$\left[\left(\frac{18}{Wo^2\gamma C_C}+\frac{1}{\sqrt{2}Wo\gamma}\right)^2+\left(\frac{1}{\sqrt{2}Wo\gamma}+\frac{3/2}{\sqrt{\gamma}}+1\right)^2\right]^{-1/2}$

number as presented in Figure 4.8. This implies that the flow state not only depends on the Reynolds number Re and the amplitude parameter ϵ, but also on the density ratio $\gamma = \rho_p/\rho_f$ between particle and fluid when particle relaxation needs to be considered. The slip velocity amplitude U is the only unknown value in order to calculate the oscillation Reynolds number $Re = Ud/\nu$ and the amplitude parameter $\epsilon = U/(\omega d)$, while the density ratio acts as a parameter for the plane. The position on the plane can still be pinpointed by calculating the Reynolds number and the amplitude parameter, but the plane looks different for each value of the density ratio. The result of calculating the slip velocity amplitude ratio with the drag model formulations from Table 5.1 can be seen in Figure 5.2, where this phenomenon is observable as plane **a)** with $\gamma = 25000$ looks different from plane **c)** with $\gamma = 8$. The first analysis of the slip velocity, which takes place in Section 5.3, is confined to the case $\gamma \gg 1$, displayed in the left plot of Figure 5.2. The case $\gamma > 1$, with its apparent model discontinuities, is addressed then in Section 5.5.

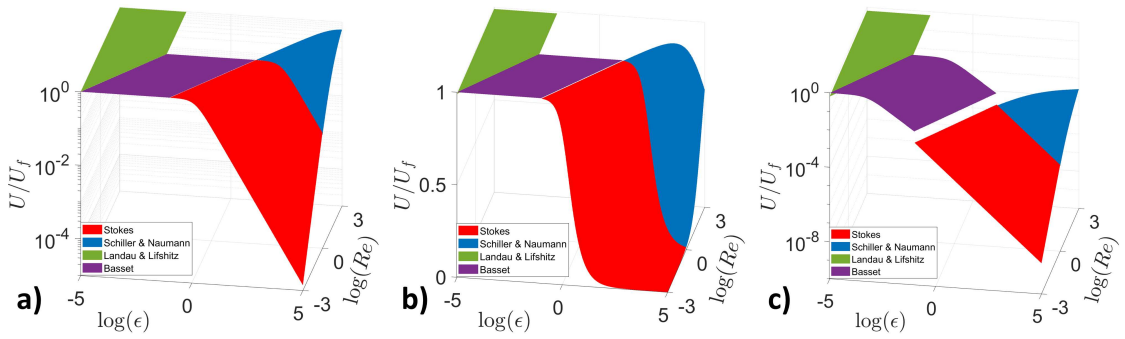

Figure 5.2. Normalized slip velocity amplitude, calculated with various drag models. **a:** $\gamma = 25000$ (logarithmic z-axis scale); **b:** $\gamma = 25000$; **c:** $\gamma = 8$.

5.3. Particle Relaxation

Particle relaxation is the transient phenomenon of particles adapting to changed flow conditions. A special case of initial particle relaxation is described in Section 4.4, where particles are released into a pulsating flow. In case of an oscillating flow, the flow velocity keeps changing, while the entrained particles can never fully adapt their velocity, leading to an oscillating, but resident slip velocity as described in Section 4.4. This slip velocity (expressed by the slip velocity amplitude U) depends on the drag at the particle, and therefore theoretically on the applied drag model. The result of calculating the slip velocity amplitude with appropriate drag models from Table 5.1 is displayed in Figure 5.2. Two areas of slip velocity behaviour can be distinguished in graph **a)** of Figure 5.2; one area where $U/U_f \approx 1$ and another area where $U/U_f < 1$. In the first area, the inertia of the particle is so high that it can not follow the flow, leading to a slip velocity as high as the fluid velocity. In the second area, the influence of relaxation is significant and the slip velocity needs to be considered more carefully. In this case, the particle motion presented in Section 4.4 takes place (see Figure 4.5), where the particle performs (harmonic) oscillations with the same frequency as the fluid, but with smaller amplitude. Here, the slip velocity can be calculated with an appropriate drag model, listed in Table 5.1. This area is tied to moderate Womersley numbers. Similar to

negligible relaxation at very high Womersley numbers, relaxation can also be neglected at very low Womersley numbers. In this case, the slip velocity amplitude becomes very small. Graph **a)** in Figure 5.2 is displayed with a logarithmic z-axis in order to better capture the slip velocity amplitude behaviour. The negligible relaxation at very low Womersley numbers becomes obvious when displaying the same data from 5.2 **a)** without a logarithmic scaled z-axis, as can be seen in graph **b)**. This means that there is not only a limit for negligible relaxation associated with high Womersley numbers, but also a limit for negligible relaxation associated with low Womersley numbers. These limits are dubbed fast relaxation limit (FRL) and slow relaxation limit (SRL), respectively, referring to the ability of the particle to adapt to the flow. As explained in Section 5.2, and observable in the discrepancy of Figure 5.2 **a)** and **c)**, the plane for the slip velocity amplitude is different, depending on the density ratio. This is also the case for the size of the three areas of negligible and impactful particle relaxation. The limits between the areas move towards higher Womersley numbers for lower density ratios and vice versa. Therefore, with the utilization of cut-off criteria, two values of the Womersley numbers can be defined, depending on a critical density ratio, above and below which particle relaxation can be neglected. This is shown in Figure 5.3, where the critical density ratio γ_{crit} is plotted against the Womersley number for various cut-off criteria, while above the solid line (SRL) and below the dashed line (FRL) the particle relaxation can be neglected. Additionally, this phenomenon is also displayed for the case of very small particles (U_{C_C}), but only discussed later in detail in Section 5.6. Since the Womersley number and the density ratio combined depend on all five input parameters of the model, as listed in Table 4.1, an asymptotic behaviour in the SRL and FRL can be determined for each input parameter as well. This asymptotic behaviour can then be expressed in

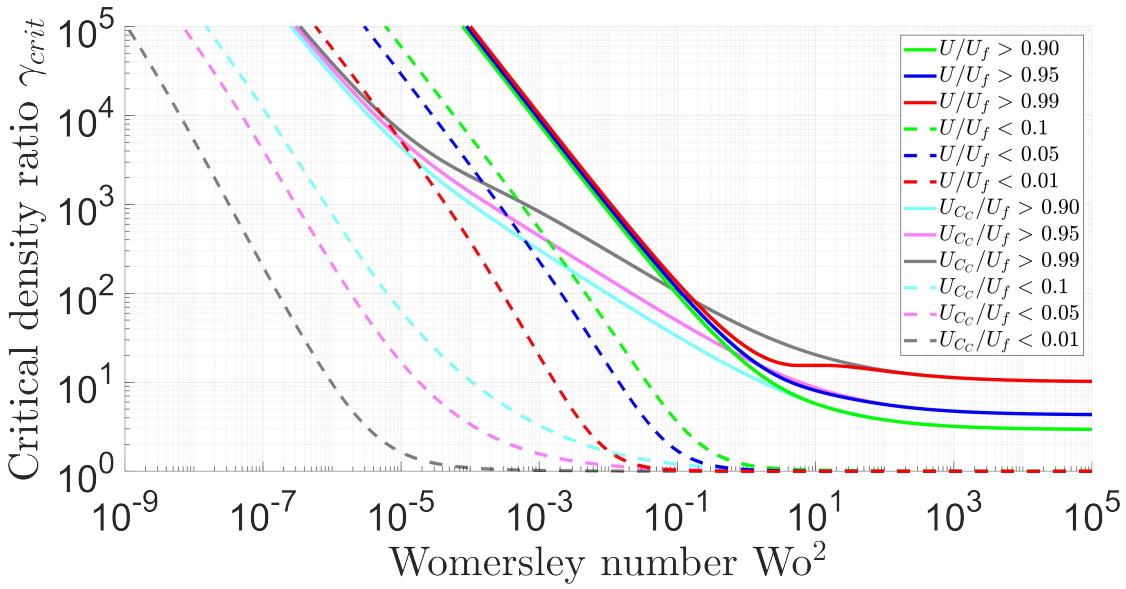

Figure 5.3. Critical density ratio depending on the Womersley number for various cut-off criteria. The particle relaxation can be neglected above the solid line and below the dashed line. Cut-off criteria for non-continuum flows are indicated with U_{C_C} for a Knudsen number of $Kn = 100$ relating to nano-sized particles.

terms of amplitude parameter and Reynolds number, as shown in the next section, which deals with effective navigation in the plane.

5.4. Navigation in the ϵ-Re Plane

Each flow state can be pinpointed in the plane as described in Section 4.7, with the support of the density ratio as a parameter in case of particle relaxation, as laid out in Section 5.3. A sensitivity study was conducted on the change in the position on the plane to a change of the various input parameters in order to utilize the plane effectively. The influence on the position on the plane is first derived with the particle diameter as an example and then transferred to the other input parameters listed in Table 4.1. Figure 5.4 shows the logarithm of the amplitude parameter and the Reynolds number displayed over the logarithm of the particle diameter. Similar to the previous section, three general areas are highlighted. In detail, this is the yellow area **a)**, where particle

relaxation happens so fast that it can be neglected (FRL). This area is associated with small particle diameters. The red area **c)** is tied to large particle diameters, and here, the particle relaxation happens so slowly that it can be neglected as well (SRL). In the last, green area **b)**, between the other areas, particle relaxation needs to be considered. While the general shape of the curves are independent of the other input parameters, the absolute values are not. This becomes clear for the curves of ϵ and Re differentiated with respect to the particle diameter, also shown in Figure 5.4. While the asymptotic values in area **a)** and **c)** are constant and independent of the other input parameters, this is not the case for area **b)**. Its location, slope, and width with respect to the diameter do depend on the value of the other input parameters. Now the sensitivity of

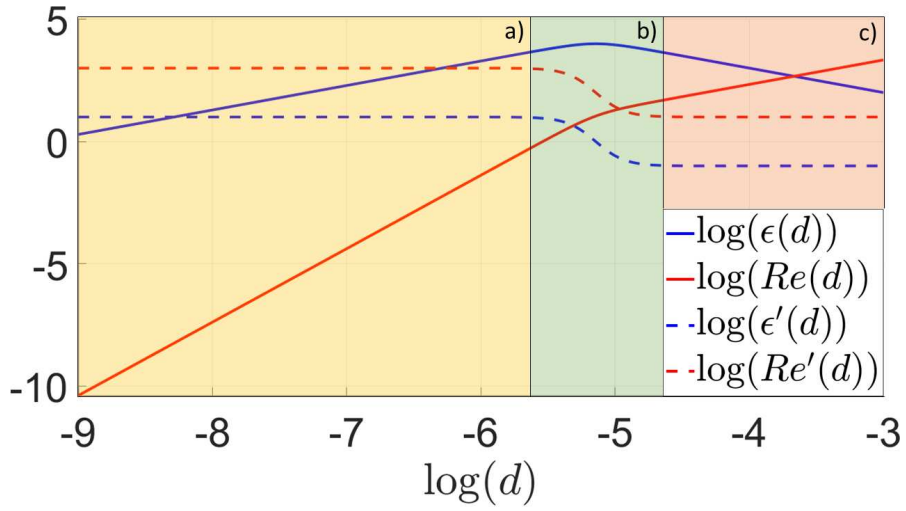

Figure 5.4. Logarithmic amplitude parameter $\log(\epsilon)$ and logarithmic Reynolds number $\log(Re)$ in respect to the logarithmic particle diameter $\log(d)$. Areas of **a)** fast relaxation limit, highlighted in yellow; **b)** considerable relaxation, highlighted in green; **c)** slow relaxation limit, highlighted in red. Additionally, the first derivatives of the logarithmic amplitude parameter $\log(\epsilon')$ and the logarithmic Reynolds number $\log(Re')$ are plotted.

the Reynolds number and the amplitude parameter in respect to the particle diameter can be derived for the fast and the slow relaxation asymptotic case, independently of the other input parameters. This information can be displayed by the length and the

direction of a vector in the logarithmic plane, as shown in Figure 5.5. Here, the fast

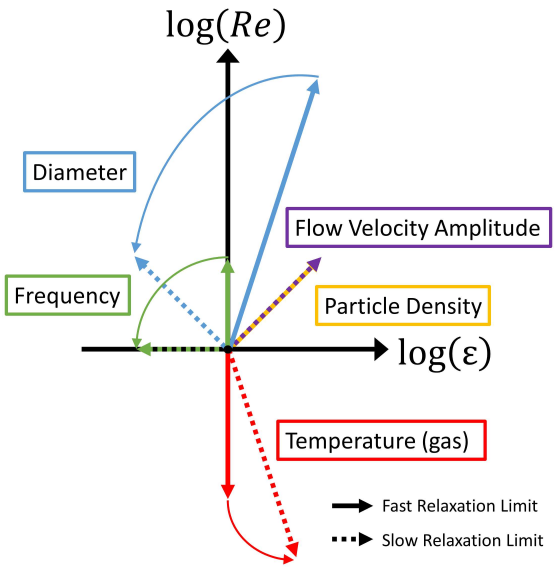

Figure 5.5. Sensitivity of the input parameters to the position on the plane. Vectors give the direction and sensitivity of a shift in position on the plane, for an increase in the respective input parameter. Solid vectors mark the shift in the fast relaxation limit, while dashed vectors show the shift in the slow relaxation limit. These red vectors are only valid if the fluid is a gas.

relaxation limit is indicated by a solid vector and the slow relaxation limit by a dashed vector. In case particle relaxation cannot be neglected, the sensitivity of the change in position on the logarithmic plane in respect to the diameter falls in between the fast and slow relaxation limit (indicated by vector length and orientation). This general approach can be transferred to the other input parameters, as shown in Figure 5.5. While a fast and slow asymptotic relaxation limit can also be derived for the frequency and fluid temperature, this is not the case for the flow velocity amplitude and the density of the particles. Note that the red vectors in Figure 5.5 are only valid in case the fluid is a gas, since the viscosity derivation in respect to the temperature has a different sign compared with a liquid. In case of a liquid, the red vectors would be mirrored at the ϵ axis. Additionally, for a liquid, the temperature dependencies cannot be modelled with the exponential functions presented in Section 4.1, leading to another length of the red

vectors in Figure 5.5. The sensitivity with respect to the flow velocity amplitude is constant and independent of other input parameters or particle relaxation, leading to a single vector in Figure 5.5 representing the influence of the flow velocity amplitude. In contrast, the slow relaxation limit of the particle density is zero, while the fast relaxation limit is the same as the velocity amplitude. This leads to the two vectors overlapping one another in Figure 5.5. Note that the logarithmic scale of the plane leads to a linear behaviour of the vectors, but, nevertheless, implies an exponential effect. Even though Figure 5.5 delivers a good overview of the influence of the various input parameters on the location on the logarithmic plane, quantification is needed in order to properly calculate any shift in position. While the vectors have the correct proportion to each other and the correct angles, absolute values are listed in Table 5.2 for each coordinate and input parameter. This is especially useful when a set point $P_1(\log(\epsilon_1), \log(Re_1))$ on the ϵ-Re plane is given. Then, the new position can be calculated for a change of an input parameter or, the other way around, in order to gain knowledge on how to change an input parameter to reach the desired location $P_2(\log(\epsilon_2), \log(Re_2))$. The following calculation describes transformation with the particle diameter as an example:

$$P_2 = P_1 + [log(d_2) - log(d_1)] \ \overrightarrow{\Psi} \tag{5.1}$$

$$\text{with} \quad \overrightarrow{\Psi} = \left(\lim_{d \longrightarrow FRL/SRL} (\log(\epsilon'(d))), \lim_{d \longrightarrow FRL/SRL} (\log(Re'(d))) \right) \tag{5.2}$$

This relation holds true for any other input parameter, as long as the respective values from Table 5.2 are applied. Several constraints need to be noted here. This calculation can only be considered valid for negligible relaxation. In case relaxation needs to be considered, Figure 5.5 gives a good impression of the amount and direction of the shift in position, but it does not deliver precise values. In case of relaxation, it is advised to apply the full algorithm in order to determine ϵ and Re as lined out in Section 5.1. Figure

5.5 and Table 5.2 provide logarithmic values only, hence, the size of a vector provides a good impression of how the location on the logarithmic ϵ-Re plane shifts, but a poor impression of the change in actual values of ϵ and Re.

Table 5.2. Calculated sensitivity of amplitude parameter ϵ and Reynolds number Re in respect to the input parameters. The values for the fluid temperature are only valid for gases.

Input Parameter	Relaxation Limit	$\lim(\log(\epsilon'))$	$\lim(\log(Re'))$	$\vec{\Psi}$	$\lvert\vec{\Psi}\rvert$	β
Particle	fast	1	3	$(1,3)$	$\sqrt{10}$	0.4π
diameter	slow	-1	1	$(-1,1)$	$\sqrt{2}$	0.75π
Oscillation	fast	0	1	$(0,1)$	1	0.5π
frequency	slow	-1	0	$(-1,0)$	1	π
Particle	fast	1	1	$(1,1)$	$\sqrt{2}$	0.25π
density	slow	0	0	$(0,0)$	0	–
Fluid velocity	fast	1	1	$(1,1)$	$\sqrt{2}$	0.25π
amplitude	slow	1	1	$(1,1)$	$\sqrt{2}$	0.25π
Fluid	fast	0	-1.67	$(0,-1.67)$	1.67	1.5π
temperature	slow	-0.67	-2.34	$(0.67,-2.34)$	2.43	1.6π

5.5. Extension of the Stokes Model

As pointed out in Sections 5.1 and 5.2, models derived by asymptotic analysis can be considered valid in the extreme value limits on which their formulations are based. It is often stated that a certain value has to be very small or very large for the application of the model, without delivering quantification. This is due to the problem that often the behavior of other influential parameters of the model are not specified or limited. If one or more of these other influential parameters reach extreme values themselves, the characteristic values that led to the simplified model must still be extreme in relation to those parameters. As an example, the Stokes model can be considered valid under the conditions of $Re \ll 1$ and $Wo \ll 1$, as laid out in Section 5.1. As a rule of thumb, Stokes delivers reasonable results up to $Re \leq 1$ in most cases. This is still true in many cases for $Re > 1$, while the number of cases becomes less and less with increasing Reynolds number. It behaves similarly with the second condition of $Wo \ll 1$. For most cases,

$Wo = 0.01$, as applied in all graphs of Figure 5.2, is sufficient. In graph **c)** of Figure 5.2 this is not the case, which is made obvious by the significant model inconsistencies. There, the density ratio $\gamma = 8$, which can be considered an extreme value (the particle has almost the same density as the fluid), and, in relation to this small γ, $Wo = 0.01$ does not fulfill the condition of $Wo \ll 1$ sufficiently. Therefore, it is now pointed out how the various models in Figure 5.1 relate to each other and under which conditions the deviations between the models become minimal. This enables the Stokes model, which is preferable over the other models as argued in Section 5.1, to be applied outside of its commonly perceived range of validity for some parameter ranges.

As soon as the transient part of the particle motion has decayed as described in Section 4.4, the resident part becomes repetitive. Since the particle then oscillates with the same frequency as the surrounding fluid, further constraints can be applied in order to enhance mathematical accessibility. With a straight, steady motion, the differences in acceleration and drag of the models lead to an ever increasing difference in velocity, while the different motions due to different drag models in an oscillating flow are continuously compensated for due to the repetitive nature of the motion. Therefore, the velocities calculated with the presented drag models deviate significantly less in oscillating flows. For large parts of the plane, $U/U_f \approx 1$ holds true. In this area, all the drag models deliver insignificantly different values for the slip velocity amplitude ratio and are therefore interchangeable there. For medium and large values of the density ratio $\gamma = \rho_p/\rho_f$, Stokes reaches $U/U_f \approx 1$, within its limits of validity, while for small values of γ this is not the case. This phenomenon is pointed out in Figure 5.2, where $\gamma = 25000$ in graph **a)** (e.g. iron particles in hot gas) and $\gamma = 8$ in graph **c)** (e.g. iron particles in water). For $\gamma = 25000$, $U/U_f \approx 1$ is reached within the Stokes model for $Re < 1$ and therefore Stokes can be extended into the unsteady area of Basset and Landau & Lifshitz (LL), since the results

deviate there only insignificantly. In contrast, for $\gamma = 8$, $U/U_f \approx 1$ is not reached within Stokes' limits of validity and it deviates therefore significantly from the other models. More so, the edges of all the considered models do not align properly to their neighbours. Even a slight deviation between Basset and LL is recognisable. While Basset converges to $U/U_f = 1$ for large Stokes numbers, this is not the case for LL, where a part dependent on γ, remains:

$$\lim_{Stk\to\infty} U_{Basset}/U_f = 1 \tag{5.3}$$

$$\lim_{Stk\to\infty} U_{LL}/U_f \quad = \frac{\sqrt{\gamma}}{\sqrt{\gamma} + 3/2} \tag{5.4}$$

The deviation between Stokes and the other models increases with a decreasing γ. This finding is also in keeping with other approaches in the literature [**21**, **151**, **155**]. For large γ, the quasi-steady approximation is valid for the entire relaxation part of the plane, and the slip velocity amplitude can be calculated by Stokes or SN. For small γ this is not the case. The same approach can be applied to the comparison between Stokes and Schiller & Naumann (SN). Here it is not γ, but rather the ratio between Re and Stk, which is the determining factor. This relates to the distinction of $U/U_f \approx 1$ being reached before or after Re becomes unity. Even though the limit $Wo^2 \ll 1$ is set here to $Wo^2 = 0.01$ in Figure 5.2, the slip velocity amplitude calculated with the Basset model still deviates substantially from the Stokes model. Similar to the comparison between Stokes and Basset, on the right-hand side of Figure 5.2, the values at the model limits between Stokes and SN and even between Basset and LL do not match well, although this effect is not as pronounced. This is contrary to the high-density ratio case displayed in graph **a)** of Figure 5.2, where the values at the model limits do match well. This raises the question of under which conditions the models connect to each other well or can even be applied interchangeably. The relation between Stokes and other models can be

calculated with the expressions presented in Table 5.3, while harmonic particle velocities and slip velocities are assumed. The derivation of the deviation between Stokes and the SN model is given in detail in Appendix C. The expressions in Table 5.3 are derived from the expressions in Table 5.1 and also depend only on γ and Wo^2. This time, however, the oscillation Stokes number $Stk = \omega\tau_p = \gamma Wo^2/18$ is utilized [**157**]. It sets the characteristic time of the particle $\tau_p = \rho_p d^2/18\eta$ in relation to the characteristic time of the flow $\tau_f = 1/\omega$. It functions as a criterion for how well the particle can adapt to the changing flow conditions. When the normalized slip velocity amplitude in an oscillating flow is calculated with the Stokes model, it is only dependent on the oscillation Stokes number $U/U_f = 1/\sqrt{1 + 1/Stk^2}$. Therefore, the oscillation Stokes number is utilized in comparing the Stokes model with the other models. The criterion for an acceptable deviation between the models was defined as 5%, and the parameter areas where the deviation is above and below this criterion are displayed in Figure 5.6 for the various models. The density ratio γ is the decisive parameter for the comparison between Stokes and Basset, as well as Stokes and the LL model, while for the comparison between Stokes and the SN model it is the Reynolds number. Additionally, at least one criterion is presented in Table 5.3 for the deviation between Stokes and the other drag models to stay below 5%, while multiple criteria are set in relation to each other via logical operators. In this case, the Stokes model can be applied in the validity range of the respective model. These criteria are also plotted in Figure 5.6. Simple criteria were chosen for the sake of convenience, as they can not match the 5% error interface perfectly. This means that the deviation will stay below 5% if the criterion is met, but it can also stay below 5% if the criterion is violated, as can be seen in Figure 5.6. Stokes can be used in order to calculate the slip velocity amplitude in the entire colored area of the plane when all criteria in Table 5.3 are met, hence $(\gamma > 1000) \wedge (\gamma Stk^{6/5} > 370) \wedge (Stk < \sqrt{3Re})$. Graphically, it is even suggested that this finding is also valid for the undefined area, where the NSEs need to be

Table 5.3. Relations of the drag models listed in Table 5.1 to the Stokes model, expressed with the oscillation Stokes number Stk and the density ratio γ. Additionally, the limit is given up to which the deviation stays below 5%, in which case the Stokes model can be applied in the validity range of the respective model. Multiple criteria are set in relation to each other via the logic operator $\wedge$—'and'.

Name	**Relation to Stokes U_i/U_{Stk}**	$\lvert U_i - U_{Stk}\rvert/U_{Stk} < 5\%$
Schiller & Naumann	$\left\{\frac{Stk^2+1}{Stk^2+SN^2}\right\}^{1/2}$ $SN = 1 + 0.158Re^{2/3}$	$\frac{\sqrt{3Re}}{Stk} < 1$
Basset	$\left\{\left[1+\frac{1}{Stk^2}\right]\left[1-(1+f_1)^2-f_2^2\right]\right\}^{1/2}$ $f_1 = \frac{2(1-\gamma)\left(1+2\gamma+3\sqrt{\frac{\gamma}{Stk}}\right)}{\left(2\frac{\gamma}{Stk}+3\sqrt{\frac{\gamma}{Stk}}\right)^2+\left(1+2\gamma+3\sqrt{\frac{\gamma}{Stk}}\right)^2}$ $f_2 = \frac{2(1-\gamma)\left(2\frac{\gamma}{Stk}+3\sqrt{\frac{\gamma}{Stk}}\right)}{\left(2\frac{\gamma}{Stk}+3\sqrt{\frac{\gamma}{Stk}}\right)^2+\left(1+2\gamma+3\sqrt{\frac{\gamma}{Stk}}\right)^2}$	$(\gamma Stk^{6/5} > 370) \wedge (\gamma > 5)$
Landau & Lifshitz	$\left\{\frac{Stk^2+1}{Stk^2\left[\left(\frac{3}{\sqrt{2\gamma Stk}}+\frac{1}{Stk}\right)^2+\left(\frac{3}{2\sqrt{\gamma Stk}}+\frac{1}{\sqrt{2\gamma}}+1\right)^2\right]}\right\}^{1/2}$	$(\gamma > 1000)$

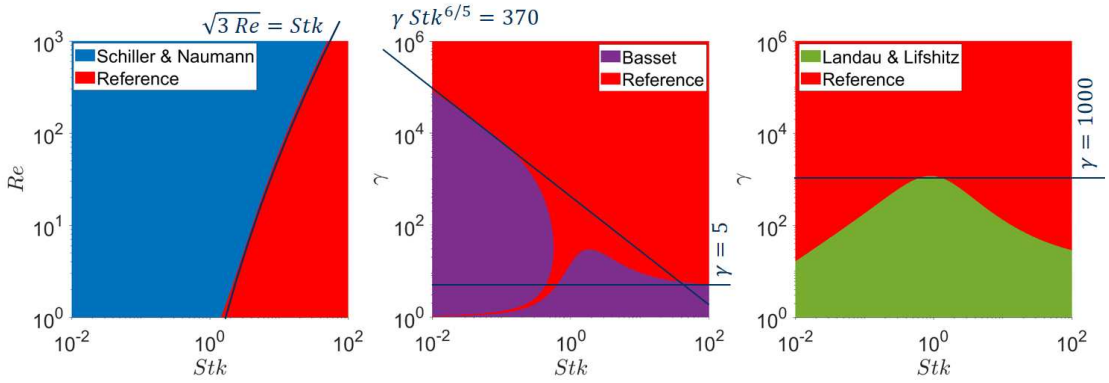

Figure 5.6. Areas where the deviation between Stokes and the respective drag model is above (blue—Schiller & Naumann; purple—Basset; green—Landau & Lifshitz) and below (red) 5%. In the red areas, the Stokes model can be applied in the validity range of the respective model.

solved numerically from a mathematical point of view. For large density ratios γ, which can be found with solid particles in hot gas flows, the Stokes model can be applied for large parts of the plane. This makes it especially interesting for modelling of particles in one-dimensional oscillating flows, for example in the investigation of a pulsation reactor. Table 5.4 shows a collection of typically treated materials in a PR with the respected

densities and the density ratios for various gas temperatures. It can be seen that the criteria for applying Stokes over the other drag models listed in Table 5.3 are met in most constellations, especially for high gas temperatures.

Table 5.4. Typical treated materials in a PR with the respected density and density ratios for various gas temperatures.

Gas temperature [°C]		**20**	**100**	**500**	**1000**
Material	Density [kg/m^3]	1.188	0.933	0.450	0.273
Zirconium dioxide	6000	5051	6432	13327	21946
Zinc oxide	5600	4714	6003	12439	20483
Aluminium oxide	4000	3367	4288	8885	14631

5.6. Additional Effects at Micro Scale

If the characteristic length, in this case the particle diameter, gets small enough, non-continuum effects will start to emerge. This is primarily the case for a gaseous environment, and this is the only case for which it is considered in this work. The dimensionless Knudsen number $Kn = \lambda_{mfp}/d$ serves as a criterion deciding whether those effects have to be considered. It is expressed by the ratio of the free mean path length of gas molecules λ_{mfp} to the particle diameter d. The free mean path length can be calculated as

$$\lambda_{mfp} = \frac{1}{\sqrt{2} n \pi d_m^2} \tag{5.5}$$

with the mean diameter of gas molecules d_m and n is the number of molecules per unit volume

$$n = \frac{p}{k_B T} \tag{5.6}$$

with the absolute pressure p, the absolute gas temperature T, and the Boltzmann constant k_B ($1.380\,649 \times 10^{-23}\,\mathrm{J\,K^{-1}}$). The mean size of gas molecules is available in literature and is tabulated for air at 3.7 nm [**140**]. The non-continuum effect with the most

influence on the problem presented here is the emerging retroactive effect of momentum transfer from the gas molecules to the particle surface. It can be factored into the drag models via an adaptation of the no slip condition at the particle surface [**163**] and a correction to the drag coefficient with the Cunningham factor C_C [**120**]:

$$C_{D,Slip} = \frac{C_D}{C_C} \tag{5.7}$$

This factor can be expressed via three empiric coefficients α, β, γ or via the experimentally determined tangential momentum accommodation coefficient σ_u:

$$C_C = \begin{cases} 1 + Kn\left[\alpha + \beta \exp\left(-\gamma/Kn\right)\right] \\ \frac{1+6\frac{2-\sigma_u}{\sigma_u}Kn}{1+4\frac{2-\sigma_u}{\sigma_u}Kn} \end{cases} \tag{5.8}$$

Here, the values for the coefficients $\alpha = 2.34$, $\beta = 1.05$, and $\gamma = -0.39$ from Allen & Raabe [**125**] for a correlation of all solid particle sizes within 2.1% [**170**] are applied, leading to

$$C_C = 1 + Kn\left[2.34 + 1.05 \exp\left(-\frac{0.39}{Kn}\right)\right] \tag{5.9}$$

Even though it is conceptually incorrect to imagine the particles with large Knudsen numbers "slipping" through the gas [**170**], the factor C_C is widely referred to as the slip correction factor in literature [**125**, **126**, **129**, **131**]. It is unity for large particle diameters and increases with decreasing particle size. Its effect becomes significant for particles smaller than 1 μm. The drag models presented in Section 5.1 are derived by asymptotic analysis or by empirical analysis of phenomenon in the continuum regime. Therefore, they can only be considered valid in the continuum regime. When particles are below dimensions of a few micrometers, the drag can then be adapted with the Cunningham factor C_C, as shown in Table 5.1. Similar to the density ratio, the Cunningham factor works as a parameter for the utilization of the plane, which is unity for most parameter

ranges. The relation between Cunningham factor and the Knudsen number is plotted on the right side of Figure 5.7, while the resulting normalized slip velocity amplitude is plotted on the left side for Knudsen number of $Kn = 100$. It becomes obvious that the

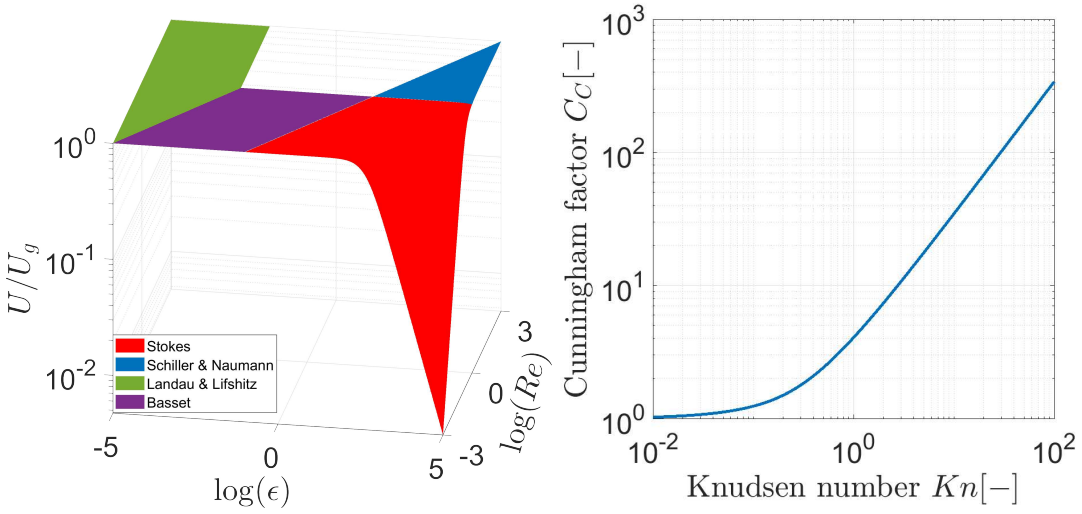

Figure 5.7. Effect of Cunningham factor. **left:** Normalized slip velocity with a density ratio of $\gamma = 25000$ (corresponds to iron particles in hot gas) and a Knudsen number of $Kn = 100$ (corresponds to nano-sized particles); **right:** Dependency of the Cunningham factor on the Knudsen number.

non-continuum drag leads to an overall enhanced slip velocity between particle and fluid and increasing the parameter area where $U/U_g \approx 1$ can be assumed. This information can also be retrieved from Figure 5.3, where the dashed lines indicate the cut-off criteria for this case. The non-continuum effects on heat and mass transfer are considered later in Section 7.7.

5.7. Analytical Particle Motion - Summary and Conclusion

The motion of a spherical particle in a one-dimensional pulsating flow was considered. The slip velocity between fluid and particle was identified as the target quantity in order to function as an input parameter for later stages of the model and was derived using the Stokes drag model. Strong simplifications were achieved by neglecting the transient part,

leading to only harmonic oscillating quantities. In case of negligible particle relaxation, the interaction of a single particle with an oscillating flow is mainly determined by the dimensionless amplitude parameter $\epsilon = U/(\omega d)$ and the oscillation Reynolds number $Re = Ud/\nu$. Therefore, the ϵ-Re plane was introduced, serving as a graphical basis for most of the following discussions. Beside Stokes, the more sophisticated flow resistance models by Schiller & Naumann, Landau & Lifshitz, and Basset were utilized in order to cover large parts of the previously introduced plane and in order to discuss particle relaxation in the plane comprehensively. The slip velocity amplitude was then calculated with all flow resistance models and the density ratio $\gamma = \rho_p/\rho_f$ between particle and fluid was introduced as a parameter. Criteria were derived under which circumstances relaxation has to be considered in order to determine the slip velocity amplitude. A sensitivity analysis on how the input parameters affect the position in the plane was presented and then it was laid out how this can be utilized in order to navigate the plane. This was followed by a discussion on the circumstances in which the preferable Stokes drag model differs insignificantly from the other models, while formulations for calculating the deviation between the models directly were presented. It was shown that the Stokes drag model is sufficient in most parameter ranges for modeling the particle motion in a hot pulsating gas flow, as featured in a pulsation reactor. Finally, the adaption of the previously presented models for small particles in the non-continuum regime was laid out. The next stage of the model is presented in the following Chapter, where the flow patterns in the vicinity of the particle are considered.

CHAPTER 6

Flow Patterns in the Vicinity of the Particle

In this chapter, the flow patterns around a fixed spherical particle in an oscillating fluid are considered. Alternatively, the case of an oscillating particle in a fluid at rest is covered as well, since the two cases are mathematically indistinguishable when the flow can be considered incompressible [**96**, **171**]. All flows in this work are considered incompressible and all presented flow patterns around the particle are the result of conducted direct numerical simulations (DNS). They are presented here in order to qualitatively discuss influential flow phenomena in various parts of the plane. The flow around the particle is considered to be symmetrical to the axis of oscillation, enabling a two-dimensional flow analysis. The flow pattern are only discussed qualitatively at this point, but a more in depth explanation of the utilized data processing algorithm, the settings, the programs, the mesh, and the investigated parameter combinations of the DNS can be found in Appendix D.

6.1. Creeping Flow

First, the trivial case of creeping flow at $Re \ll 1$ and arbitrary ϵ is dealt with. Independent of the particle displacement amplitude A, the flow in the direct vicinity of the particle behaves as a creeping flow, where all inertial forces can be neglected, and the flow pattern is point-symmetrical to the particle center. The according area in the plane is highlighted in the graph on the left-hand side of Figure 6.1, while the flow pattern is displayed on the right side.

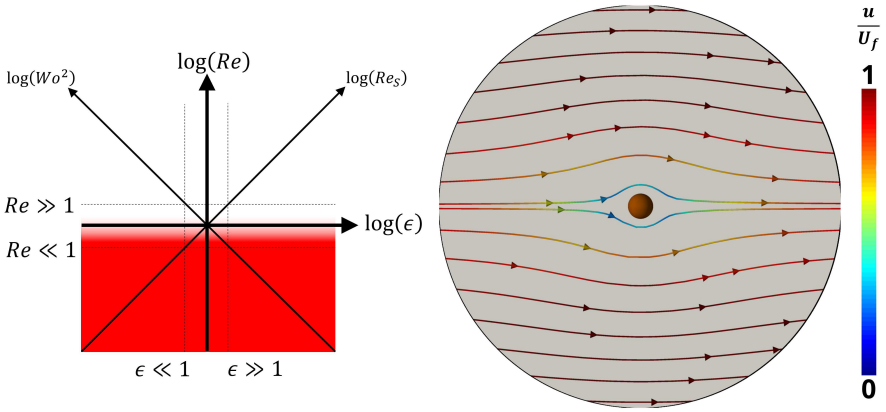

Figure 6.1. Flow pattern around the particle at maximum velocity for small Reynolds numbers $Re \ll 1$. **left:** ϵ-Re plane with the respective area highlighted in red; **right:** Creeping flow pattern around the particle. Stream line colors are displayed normalized with the fluid velocity amplitude.

6.2. Quasi-steady Flow

In case the the amplitude parameter is large enough, the particle travels enough distance, compared with its own size, that a classic boundary layer, described by Prandtl [**172**], will form. In this case, the steady boundary layer dominates, and the flow pattern can be considered quasi-steady. The shape and features of this boundary layer depend primarily on the Reynolds number of the flow [**173**]. For $Re \ll 1$, this translates into a creeping flow as already described in the previous paragraph and displayed in Figure 6.1. For an increasing Reynolds number $Re \approx 1$, the point-symmetry to the particle centre is lost, while the streamlines shift towards the wake of the particle. The respective area on the plane is highlighted on the left side of Figure 6.2, while the according flow pattern around the particle is displayed on the right side. If the Reynolds number is further increased, back flow vortices will form in the wake of the particle, while the flow pattern is still symmetric to the axis of oscillation. With an increasing Reynolds number $Re \gg 1$, the prominent Kármán vortex street behind the particle develops. This can be observed in Figure 6.3

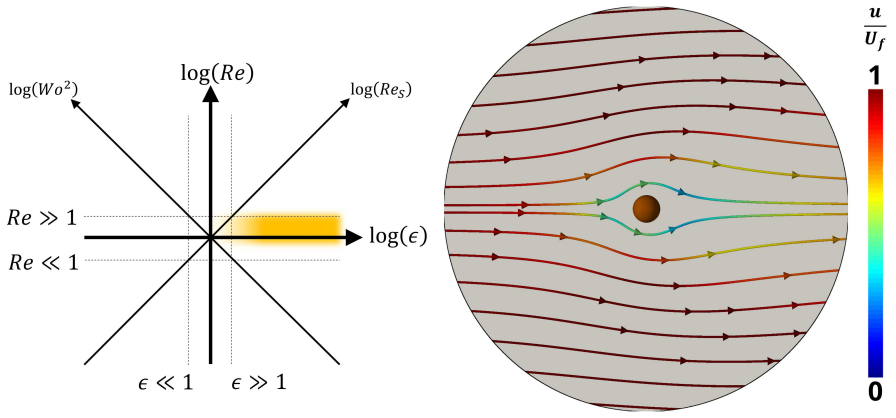

Figure 6.2. Flow pattern around the particle at maximum velocity for large amplitude parameters $\epsilon \gg 1$ and moderate Reynolds numbers $Re \approx 1$. **left:** ϵ-Re plane with the respective area highlighted in yellow; **right:** Flow pattern around the particle, where the streamlines start to shift towards the wake. Stream line colors are displayed normalized with the fluid velocity amplitude.

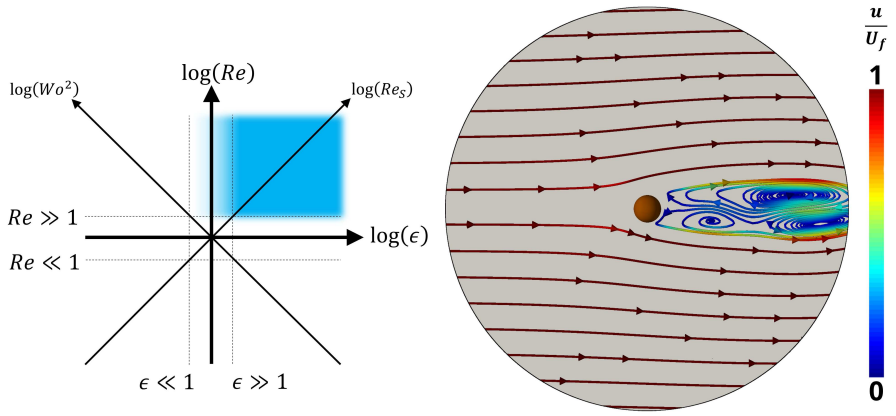

Figure 6.3. Flow pattern around the particle at maximum velocity for large amplitude parameters $\epsilon \gg 1$ and high Reynolds numbers $Re \gg 1$. **left:** ϵ-Re plane with the respective area highlighted in blue; **right:** Flow pattern around the particle with Kármán vortex street in the wake. Stream line colors are displayed normalized with the fluid velocity amplitude.

6.3. Steady Streaming

After dealing with the quasi-steady case, the influence of unsteady oscillation is now discussed. In the case of a small amplitude parameter $\epsilon \ll 1$ and a small Reynolds number $Re \ll 1$, the creeping flow pattern as presented in Figure 6.1 occurs. With an increasing Reynolds numbers $Re > 1$, while keeping $\epsilon \ll 1$, the second order phenomenon

of Steady Streaming becomes more and more pronounced and a distinction between primary and secondary flow must be made. While the primary flow still behaves very similar to the quasi-steady case, wake shedding is prevented and second order steady rotating vortices form in four quadrants around the particle. Each flow pattern of the primary flow is a snapshot of the flow around the particle taken at the maximum slip velocity, while secondary flow patterns result from averaging the velocity distribution over one (or several) full oscillation cycle(s). The phenomenon is displayed in Figure 6.4, where, on the bottom right-hand side, the secondary flow around the particle is presented. Four

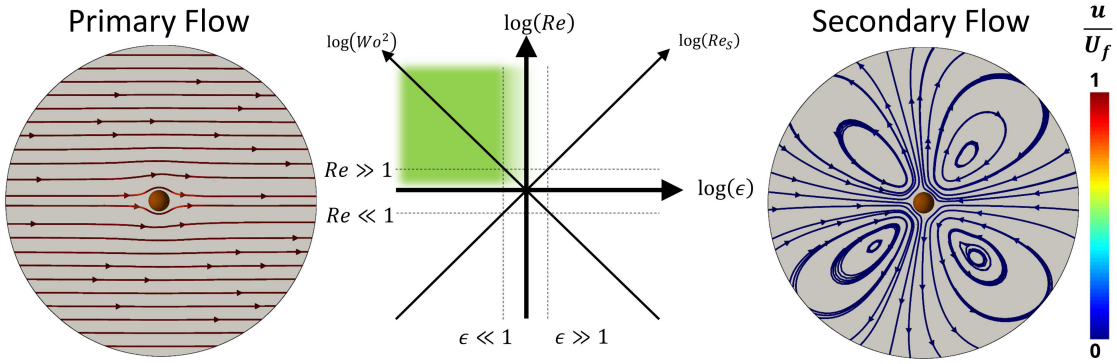

Figure 6.4. Flow pattern around the particle at maximum velocity for small amplitude parameters $\epsilon \ll 1$ and high Reynolds numbers $Re \gg 1$. **left:** ϵ-Re plane with the according area highlighted in green; **top right:** Primary flow pattern around the particle. **bottom right:** Secondary flow pattern (Steady Streaming) around the particle with **thick** inner boundary layer. Stream line colors are displayed normalized with the fluid velocity amplitude.

steady rotating vortices are visible, which stretch close to the particle's surface. Here, the inner, so-called Stokes layer, extends far into the flow. In contrast, in case the Reynolds number is large $Re \gg 1$, while the the amplitude parameter is moderate $\epsilon \approx 1$, the inner boundary layer becomes thinner and is enclosed by another outer boundary layer. This outer boundary layer also consists of 4 steady rotating vortices. High velocities close to the particle surface emerge in this configuration. This is visible in the bottom right-hand corner of Figure 6.5, where there are not just four, but eight steady vortices to be seen.

The inner boundary layer is magnified and, due to the velocity color code, a substantial velocity compared with the free stream velocity amplitude (30-40%) directly at the particle surface is noticeable. These special flow patterns with their distinctive velocity distributions relate directly to the occurring heat and mass transfer at the particle, as is derived in the next chapter. An overview of the distinctive flow patterns for various areas of the plane can be found in Figure 6.6.

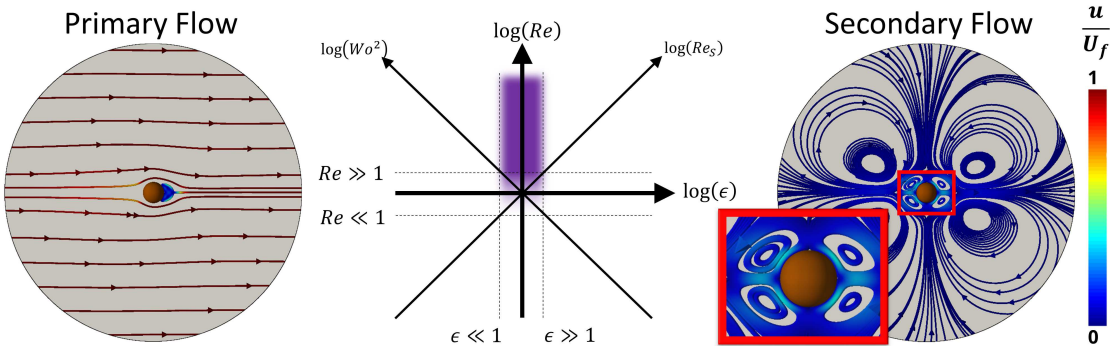

Figure 6.5. Flow pattern around the particle at maximum velocity for moderate amplitude parameters $\epsilon \approx 1$ and high Reynolds numbers $Re \gg 1$. **left:** ϵ-Re plane with the respective area highlighted in purple; **top right:** Primary flow pattern around the particle. **bottom right:** Secondary flow pattern (Steady Streaming) around the particle with **thin** inner boundary layer. Stream line colors are displayed normalized with the fluid velocity amplitude.

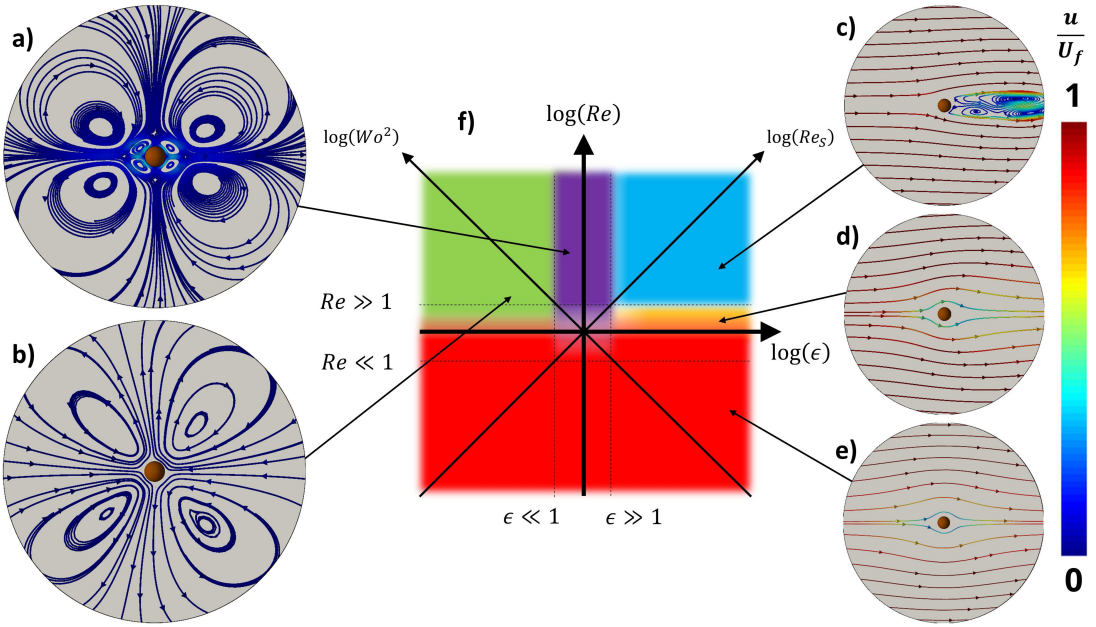

Figure 6.6. Overview of flow patterns around the particle in the ϵ-Re plane: **a)** Steady Streaming with thin inner boundary layer at $\epsilon \approx 1$ and $Re \gg 1$ (purple); **b)** Steady Streaming with thick inner boundary layer at $\epsilon \ll 1$ and $Re \gg 1$ (green); **c)** Quasi-steady flow with Kármán vortex street behind the particle at $\epsilon \gg 1$ and $Re \gg 1$ (blue); **d)** Quasi-steady flow with asymmetry towards the wake of the particle at $\epsilon \gg 1$ and $Re \approx 1$ (yellow); **e)** Creeping flow around the particle at an arbitrary ϵ and $Re \ll 1$ (red); **f)** ϵ-Re plane with respective areas of flow patterns. Stream line colors are displayed normalized with the fluid velocity amplitude.

CHAPTER 7

Heat and Mass Transfer to Particles

In Chapters 4, 5, and 6 of this work, it was established how the motion of a particle in an oscillating flow and the resulting flow patterns around it can be defined by two dimensionless numbers: the oscillation Reynolds number Re and the amplitude parameter ϵ, which span a plane as shown in Figure 4.9. These two dimensionless numbers are also central for the consideration of the heat and mass transfer (HMT) resulting from the oscillation of the flow. This means that not only is the motion of particles defined for each point in the ϵ-Re plane, but also the resulting flow patterns, as well as the heat transfer in the form of the Nusselt number Nu and the mass transfer in the form of the Sherwood number Sh. The Nusselt number expresses the ratio of convective to conductive heat transfer intensity over any boundary layer; in this case, to the particle surface. It can be utilized more generally as a metric of intensity of convective heat transfer to the particle. The Sherwood number is defined analogously for mass transfer.

In this chapter, a Nusselt(Sherwood) number correlation for the entire plane is derived. For this purpose, a structured literature review is presented in order to cover large parts of the plane with experimental, numerical, and analytical data for the occurring HMT. First, the structure of the acquired data is presented in Section 7.1. This is followed by a discussion on how the quasi-steady part of the plane is defined and how modelling in this part is handled in Section 7.2. A separate meta correlation is suggested for this part of the plane. Afterwards, Section 7.3 handles the data for the HMT in oscillating flows and a meta correlation for the entire plan is presented while incorporating the steady meta

correlation in the model building process. Subsequently, the design of the meta correlation and the deviations to the considered models are discussed in Sections 7.4 and 7.5. Then, in Section 7.6, the meta correlation is compared to the quasi-steady assumption in order to highlight areas in the plane of enhanced and reduced HMT due to the oscillation of the flow. The discussion of non-continuum effects for the consideration of particle drag in Section 5.6 is extended here in Section 7.7 since these effects also play a role in the HMT to particles. Chapter 7 is then summarized and concluded in Section 7.8. Large parts of this chapter have already been published separately by the author **[174]**, but are laid out here again for the sake of comprehensiveness.

7.1. Data

A list of the 33 considered works can be found in Table 7.1 and a graphical overview in Figure 7.1. The Reynolds analogy (Prandtl analogy) is considered applicable in oscillating flows **[162, 175, 176]**, leading to the interchangeability of correlations for Nusselt number and Sherwood number by exchanging the Schmidt number for the Prandtl number and vise versa. Therefore, the correlations for the HMT to particles suggested by many authors can be expressed generally as

$$Nu(or\ Sh) = A + \left(BRe^{i} + CRe^{j}\right) Pr^{k}(or\ Sc^{k})\epsilon^{l} \tag{7.1}$$

while the parameters (A, B, C, i, j, k, l) differ for individual correlations. For steady HMT, this approach has been used by Yavuzkurt et al. **[176]** and is extended here with the term 'ϵ^{l}' in order to incorporate correlations for oscillating flows. All correlations in Table 7.1 fit this general ansatz except one. Sometimes, no correlation was provides by the respective authors, but their data sets were utilized directly. In the upper part of Table 7.1, correlations for the HMT to particles in steady flows are listed, while the

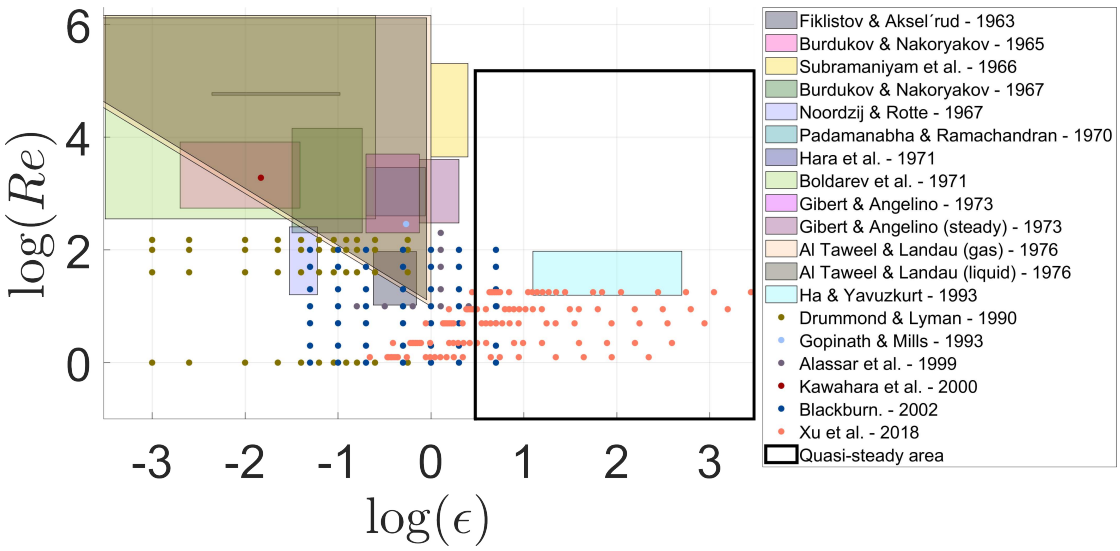

Figure 7.1. Overview of considered experimental and numerical data and correlations for the HMT to particles in **oscillating** flows. Colored patches indicate a provided correlation by the authors, while single points indicate individual measurement and simulation points without a correlation provided by the respective authors.

lower part displays correlations for the HMT in oscillating flows. At the end of each part, the meta correlations derived here are displayed. Additionally, the validity range of each correlation is mentioned, which was explicitly stated by the authors or implicitly derived by the range of their data. The validity ranges are in terms of solely the Reynolds number for steady correlations and Reynolds number and amplitude parameter for oscillating flows. Furthermore, the normalized root mean squared deviation ($NRMSD$) and the normalized root maximum squared deviation are presented for the deviation of the individual correlation or data set from the respective meta correlation. The $NRMSD$ is calculated via

$$NRMSD = \sqrt{\frac{\sum_{i=1}^{n} (y_i - \hat{y}_i)^2}{j\bar{y}^2}} \tag{7.2}$$

with the value of the respective correlation or single data point y_i, the value of the meta correlation $\hat{y}_i$, the value range of the respective correlation $\bar{y}$, and the number of sample points j. Note that the R^2 value (coefficient of determination) is not a suitable measure for the correlation of nonlinear regressions **[177]** and is therefore not used here. The source of the data is cited in the last column of Table 7.1. Figure 7.1 provides an overview of where in the plane data exist in literature. The colored patches indicate correlations provided by the respective authors, while dots indicate individual points of data. All of the data from oscillating flows, which are also listed in the lower part of Table 7.1, are displayed there, while the quasi-steady area is only marked with a black rectangle. In this area, the steady models from the upper part of Table 7.1 can be applied, but are not plotted individually for the sake of clarity. It is now discussed in the next section how this area is defined and how the steady models are incorporated.

Table 7.1. A list of investigated works in literature dealing with the HMT to spherical particles in steady (upper part) and oscillating flows (lower part). The conducted data preparation for some marked works (†, ‡, ††) can be found in Appendix E.

Authors	***Re* [-]**	**Steady *NRMSD* [%](max)**	**Meta *NRMSD* [%](max)**	**A**	**B**	**C**	**i**	**j**	**k**	**l**	**Source**
Mori et al.	4 - 24	8.4 (12.3)	8.7 (15.1)	2.000	0.550	0.000	0.500	0.000	0.333	0.000	[**81**]
Ranz & Marshall	0.1 - 2×10^2	3.8 (10.3)	3.8 (24.3)	2.000	0.600	0.000	0.500	0.000	0.333	0.000	[**178**]
Hsu et al.	60 - 320	6.4 (9.0)	8.4 (30.2)	2.000	0.544	0.000	0.500	0.000	0.333	0.000	[**179**]
Whitaker	3.5 - 7.6×10^4	7.0 (21.9)	5.2 (46.1)	2.000	0.400	0.060	0.500	0.667	0.400	0.000	[**180**]
Gnielinski	1 - 10^4	9.8 (32.9)	7.2 (28.1)	2.000	0.664	0.000	0.500	0.000	0.333	0.000	[**181**]
Ke et al.	10 - 200	9.7 (19.2)	9.0 (21.7)	1.910	0.545	0.019	0.500	0.667	0.333	0.000	[**182**]
Richter & Nikrityuk	10 - 250	6.9 (15.5)	6.8 (24.6)	1.760	0.550	0.014	0.500	0.667	0.333	0.000	[**183**]
Sayegh & Gauvin	0.2 - 100	3.4 (5.1)	3.8 (28.3)	2.000	0.473	0.000	0.552	0.000	0.780	0.000	[**184**]
Melissari & Argyropoulos	10^2 - 5×10^4	2.9 (7.2)	3.5 (36.7)	2.000	0.470	0.000	0.500	0.000	0.360	0.000	[**185**]
Witte	3.5×10^4- 1.5×10^5	26.2 (35.8)	20.9 (72.2)	2.000	0.386	0.000	0.500	0.000	0.500	0.000	[**186**]
Chuchottaworn et al.	1 - 200	7.8 (26.5)	6.3 (23.4)	2.000	0.370	0.000	0.610	0.000	0.510	0.000	[**187**]
Bagchi et al.	50 - 500	10.2 (15.1)	11.7 (23.1)	data points - no given correlation							[**188**]
Blackburn	1 - 100	6.0 (11.2)	6.0 (13.8)	data points - no given correlation							[**109**]
Acrivos & Taylor	0 - 1	6.4 (7.4)	6.2 (14.0)	$\overline{\overline{Nu}} = 2 + \frac{1}{2} RePr + \frac{1}{4} (RePr)^2 \log(RePr)$							[**189**]
Steady meta correlation	10^{-1} - 1.5×10^5	4.3 (27.1)	1.7 (24.0)	2.000	0.500	0.000	0.500	0.000	0.333	0.000	[**174**]

Authors	***Re* [-]**	**ϵ [-]**	**Meta *NRMSD* [%](max)**	**A**	**B**	**C**	**i**	**j**	**k**	**l**	**Source**
Fiklistov & Aksel'rud	10.5 - 93.5	0.24 - 0.7	21.1 (38.4)	0.000	0.490	0.000	0.700	0.000	0.333	0.130	[**91**]
Burdukov & Nakoryakov †	5.5×10^2 8.4×10^3	2×10^{-3} 4.5×10^{-2}	8.2 (20.8)	0.000	1.300	0.000	0.500	0.000	0.500	0.500	[**89**]
Subramaniyam et al.	4.5×10^3 2.0×10^5	1 2.5	7.4 (33.5)	0.000	0.259	0.000	0.620	0.000	0.333	0.000	[**190**]
Burdukov & Nakoryakov ‡	2×10^2 1.4×10^4	3.2×10^{-2} 0.18	23.1 (62.2)	0.000	0.640	0.000	0.500	0.000	0.333	0.167	[**90**]
Noordzij & Rotte	16 2.6×10^2	3×10^{-2} 6×10^{-2}	29.7 (61.8)	0.000	0.096	0.000	0.500	0.000	0.500	0.000	[**190**]
Padamanabha & Ramachandran	4×10^2 2.9×10^3	0.2 0.87	27.5 (107.4)	0.000	0.505	0.000	0.640	0.000	0.000	0.630	[**93**]
Hara et al.	5.5×10^4 6.1×10^4	4.4×10^{-3} 0.11	26.8 (50.1)	0.000	7.500	0.000	0.500	0.000	0.333	0.167	[**190**]
Boldarev et al. ††	35.4 1.4×10^6	3.1×10^{-4} 0.25	15.4 (52.5)	0.000	0.640	0.000	0.500	0.000	0.333	0.167	[**95**]
Gibert & Angelino	2×10^2 5×10^3	0.2 0.75	10.3 (29.0)	0.000	0.592	0.000	0.538	0.000	0.333	0.269	[**96**]
Gibert & Angelino	3×10^2 4×10^3	0.75 2	23.9 (40.0)	0.000	0.558	0.000	0.538	0.000	0.333	0.000	[**96**]
Ha & Yavuzkurt	16 - 94	12.5 - 500	7.9 (16.0)	2.000	0.420	0.000	0.500	0.000	0.333	0.000	[**191**]
Al Taweel & Landau (gas)	10 - 10^6	10^{-4} - 1	1.2 (10.5)	0.000	1.100	0	0.500	0	0.500	0.500	[**190**]
Al Taweel & Landau (liquid)	10 - 10^6	10^{-4} - 1	8.3 (51.6)	0.000	0.640	0	0.500	0	0.500	0.500	[**190**]
Kawahara et al.	1.9×10^3	1.48×10^{-2}	55.9	data points - no given correlation							[**85**]
Gopinath & Mills	2.87×10^2	0.54	15.8	data points - no given correlation							[**83**]
Drummond & Lyman	1 - 150	10^{-4} - 1	64.0 (190.7)	data points - no given correlation							[**99**]
Alassar et al.	10 - 200	0.16 - 5	39.3 (76.7)	data points - no given correlation							[**100**]
Xu et al.	1.25 - 18	0.22 - 2.7×10^3	11.5 (39.5)	data points - no given correlation							[**192**]
Blackburn	1 - 100	5×10^{-2} - 5	30.6 (73.1)	data points - no given correlation							[**109**]
Meta correlation (gas)	10^{-1} - 10^6	10×10^{-3} - 10^3	0.8 (10.4)	$\overline{\overline{Nu}} = 2 + 0.5 Re^{1/2} Pr^{1/3} \left[\frac{1}{0.45\epsilon^{-1/2}+1} + \frac{1}{2.50 \exp(\log(\epsilon))^2 - 1.25} \right]$							[**174**]
Meta correlation (liquid)	10^{-1} - 10^6	10×10^{-3} - 10^3	3.7 (51.5)	$\overline{\overline{Nu}} = 2 + 0.5 Re^{1/2} Pr^{1/3} \left[\frac{1}{0.78\epsilon^{-1/2}+1} + \frac{1}{2.50 \exp(\log(\epsilon))^2 - 1.85} \right]$							[**174**]

7.2. The Quasi-Steady HMT Area of the Plane

Several authors concluded that, for a large enough amplitude parameter ϵ, the HMT in oscillating flow can be described by correlations for steady flow with sufficient accuracy. In these cases the quasi-steady assumption hold true. This threshold was suggested as $\epsilon > 0.75$ by Gibert & Angelino [**96**] and supported by Al Taweel & Landau [**190**], while Drummond & Lyman [**99**] derived it to be $\epsilon > 0.25$. The general quasi-steady assumption for large ϵ is also supported by the theoretical work of Ha & Yavuzkurt [**191**] and the work of Subramaniyam et al. [**190**]. Additionally, the experimental work of Xu et al. [**192**] fit the quasi-steady assumption quite well, for $\epsilon > 1$ but also for $\epsilon < 1$. The simulation results of Blackburn [**109**] and Alassar et al. [**100**] match each other well and also match the steady state assumption for $\epsilon \gg 1$. In light of the review of the bulk of recent data, the approach of modelling the HMT for large ϵ validly with the quasi-steady assumption is substantiated. Nevertheless, the exact quasi-steady limit remains unclear, but it is approximately $\epsilon \approx 1$. For the sake of a comprehensive approach and in order to avoid model discontinuities (which other authors accepted), a conservative $\epsilon \geq 3$ is chosen as the quasi-steady limit in this work. A black rectangle marks the quasi-steady area in Figure 7.1, where a multitude of steady data is available. For this area, a first structured review of steady models for the HMT to particles is conducted. While meta studies on this topic by Whitaker [**180**] and Gnielinski [**181**] provide good insights and also incorporate a large number of works, they arrive at somewhat different correlations. These two studies, along with central preceding studies and newer experimental and numerical works, are plotted in Figure 7.2. Solid lines indicate correlations given by the respective authors in the stated ranges of validity, or implicitly by the investigated ranges, while dots represent data points without a correlation provided by the authors. The dependencies of the investigated correlations on the Prandtl number (Schmidt number) are not considered in

this work in order to achieve a better comparison of the Reynolds number dependencies. A meta correlation of the steady Nusselt number (Sherwood number) averaged over the surface of the particle

$$\overline{Nu}(\overline{Sh}) = 2 + 0.5Re^{1/2}Pr^{1/3}(Sc^{1/3}) \tag{7.3}$$

is suggested for its simplicity, while fitting the data well. The normalized root-mean-square deviation ($NRMSD$) of each correlation or data set from Steady Meta Correlation 7.3 is provided in Table 7.1. The meta correlation fits most of the correlations very

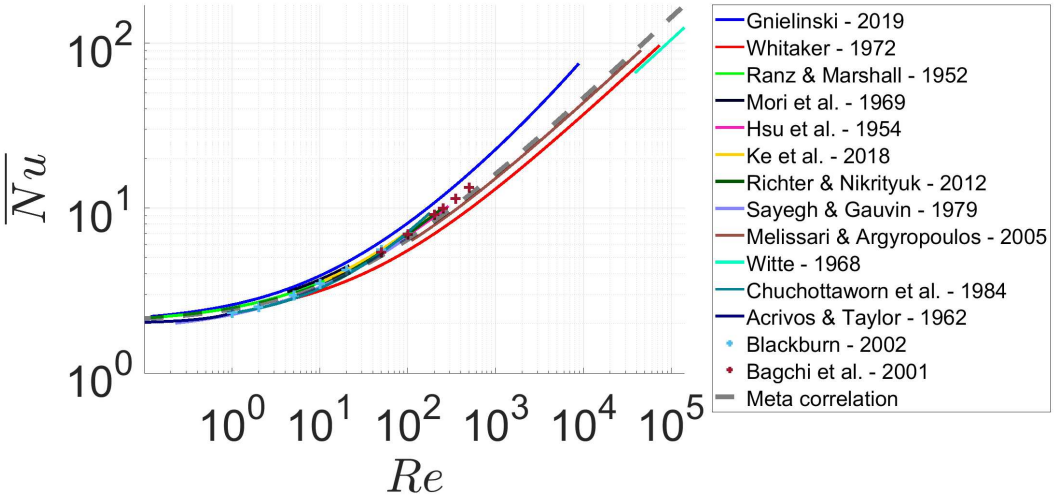

Figure 7.2. Overview of considered experimental and numerical HMT data for single spherical particles in **steady** flow. Solid lines indicate correlations provided by the respective authors, while single points indicate individual measurements or simulation points without correlations provided by the authors. Additionally, **Steady** Meta Correlation 7.3 is plotted, which is fitted to the listed data. The Prandtl number is set to $Pr = 0.71$ as it is found with air at STP.

well with each NRMSD $\leq$ 10%, as shown in Figure 7.4. The only outlier is Witte (26.2%), which represents a special case with the investigation of the HMT to a tantalum sphere in liquid sodium. Based on the deviation from the other experimental setups and investigated systems, a somewhat different correlation is expected. Since the steady meta

correlation of this work over-predicts the lowest values of the meta study by Whitaker (7.0%) to a similar degree as it under-predicts the highest values of the meta study by Gnielinski (9.8%), it is deemed acceptable at this point based on the lack of any further data for spheres in high Reynolds number flows. The Meta Correlation 7.3 is now used in order to model the HMT to particles in oscillating flows for $\epsilon \geq 3$, together with the data from oscillating flows.

7.3. Models for Oscillating Flows

Several works exist in literature which have investigated the HMT to spheres in an oscillating flow with an $\epsilon \geq 3$. Their data often fit the quasi-steady assumption well or they suggested a steady correlation themselves, as discussed in Section 7.2. This is not the case for $\epsilon \ll 1$, where the amplitude parameter has to be taken into account, especially if, in addition to a small ϵ, also large Womersley numbers $Wo^2 \gg 1$ occur. In these cases, the Streaming Reynolds number $Re_S = Re\ \epsilon$ is significant, leading to an increased influence of Steady Streaming in the HMT process [**61**]. Most investigated authors account for the influence of Steady Streaming by correcting the steady HMT correlations with a term "ϵ^l", or sometimes directly working with the Streaming Reynolds number. Taxonomy 7.1 was updated to incorporate these models accordingly. The meta study by Al Taweel & Landau [**190**], confined to the mass transfer in the Steady Streaming area of the plane, laid the groundwork for this updated meta study. On the one hand, unfortunately, some of their referenced papers are no longer available, leaving only the data as stated by Al Taweel & Landau. On the other hand, even more data could be retrieved from some of the works investigated by Al Taweel & Landau with the help of the relations presented in Figure 4.8. A detailed explanation of the conducted data preparation can be found in Appendix E. However, more data from various recent works are available now, especially for a gaseous environment: Gopinath & Mills [**83**] based their work on the flow formulations by Riley [**57**] for the region of impactful Steady Streaming with $\epsilon \ll 1$ and $Wo^2 \gg 1$. They derived the governing equation of energy for this case, which is numerically solved along with the equation of motion in order to provide several data points for a regression. A simple experiment was conducted for the validation of the resulting correlation. Kawahara et al. [**85**] investigated the mass transfer

from a camphor-covered sphere placed in an USL. They found good agreement with the experiments of Gopinath & Mills and Burdukov & Nakoryakov. Drummond & Lyman [**99**] applied a pseudospectral method in order to solve the NSEs and mass transport equations. They found a decreasing HMT for an increasing amplitude parameter, which is a unique result within the literature. Additionally, they suggested a quasi-steady limit of $\epsilon \geq 0.25$. Alassar et al. [**100**] solved the NSEs and energy equations for a Boussinesq fluid. The Prandtl number was assumed constant, $Pr = 0.71$, as was done in this work. While the authors investigated the forced and mixed convection regimes, only data for forced convection were utilized in this work for better comparability. Ha & Yavukurt [**191**] solved the two-dimensional, unsteady, laminar conservation equations for mass, momentum, and energy transport numerically in order to investigate the heat transfer to a particle. They found that for $\epsilon \gg 1$ it can be approximated well with the steady HMT approach. Xu et al. [**192**] investigated the heat transfer from a coal particle in a power plant boiler in the presence of an acoustic field. The mathematical framework of Ha & Yavukurt was utilized, while the particle size was kept constant at 100 µm and the flue gas properties were kept constant at a temperature of 1200 °C. The oscillation frequency and oscillation amplitude were varied and they found a decrease in heat transfer intensity at $\epsilon \ll 1$, an increase at $\epsilon \approx 1$, and a decreasing dependency on the amplitude parameter for $\epsilon \gg 1$. The numerical calculations were validated by experiments with copper spheres in an acoustic field. Blackburn [**109**] investigated the heat and mass transfer to a particle in an oscillating flow numerically. The author also utilized the two defining dimensionless numbers of amplitude parameter $0.05 \leq \epsilon \leq 5$ and oscillating Reynolds number $1 \leq Re \leq 100$. Additionally, the steady case was calculated for comparison. Blackburn found a slightly decreased HMT intensity for the oscillating case compared with the steady case. This is a unique result in the literature, even though the author's values for the steady case are slightly higher than those found in many other works.

The HMT in gases and liquids are quite similar to each other since it is subject to the same physical phenomena and, therefore, often modelled similarly. Although the Prandtl numbers (Schmidt numbers) are commonly several magnitudes greater in liquids than in gases, the basic models and correlations are the same. This is not the case for Steady Streaming, where different asymptotic behaviour for $\epsilon \to 0$ could be observed in gases and liquids, necessitating a distinction of cases [**190**]. Therefore, similar to the

approach for the steady models in the previous section, two meta correlations were found covering the entire plane, one being applicable for a gaseous environment and the other for a liquid environment. The Nusselt number (Sherwood number) is averaged over the particle surface and averaged over one oscillation cycle in this case.

Meta correlation for **gaseous** environments:

$$\overline{\overline{Nu}}\left(\overline{\overline{Sh}}\right) = \underbrace{2}_{A} + \underbrace{0.5Re^{1/2}Pr^{1/3}\left(Sc^{1/3}\right)}_{B}\underbrace{\left[\frac{1}{0.45\epsilon^{-1/2}+1}\right]}_{C} + \underbrace{\left[\frac{1}{2.50\exp(\log(\epsilon))^2-1.25}\right]}_{D} \tag{7.4}$$

Meta correlation for **liquid** environments:

$$\overline{\overline{Nu}}\left(\overline{\overline{Sh}}\right) = \underbrace{2}_{A} + \underbrace{0.5Re^{1/2}Pr^{1/3}\left(Sc^{1/3}\right)}_{B}\underbrace{\left[\frac{1}{0.78\epsilon^{-1/6}+1}\right]}_{C} + \underbrace{\left[\frac{1}{2.50\exp(\log(\epsilon))^2-1.85}\right]}_{D} \tag{7.5}$$

Figure 7.3 displays all the investigated models in the plane together with Meta Correlation 7.4 for gaseous environments. The Prandtl number is set to $Pr = 0.71$ as is found with air at STP.

7.4. Meta Correlation Design

The plane captures the extremes of very small and very large amplitude parameters and Reynolds numbers. It was ensured that Meta Correlations 7.4 and 7.5 follow all the various asymptotic behaviours that the experimental and theoretical works in literature derived. For small Reynolds numbers, the conductive (diffusive) limit of $Nu(Sh) = 2$ for a sphere is ensured with the term 'A'. The quasi-steady behaviour of $\epsilon \gg 1$ is modeled with term 'B', which reflects the Steady Meta-Correlation 7.3. While term 'C' tends towards unity for large ϵ, term 'D' tends towards zero. The steady Term 'B' is then corrected for $\epsilon \ll 1$ with Term 'C'. This term places the dependency on ϵ and corrects the factor accordingly. Here, a distinction needs to be drawn between the asymptotic behaviour in gases and liquids, hence the two correlations differ here. The enhancement

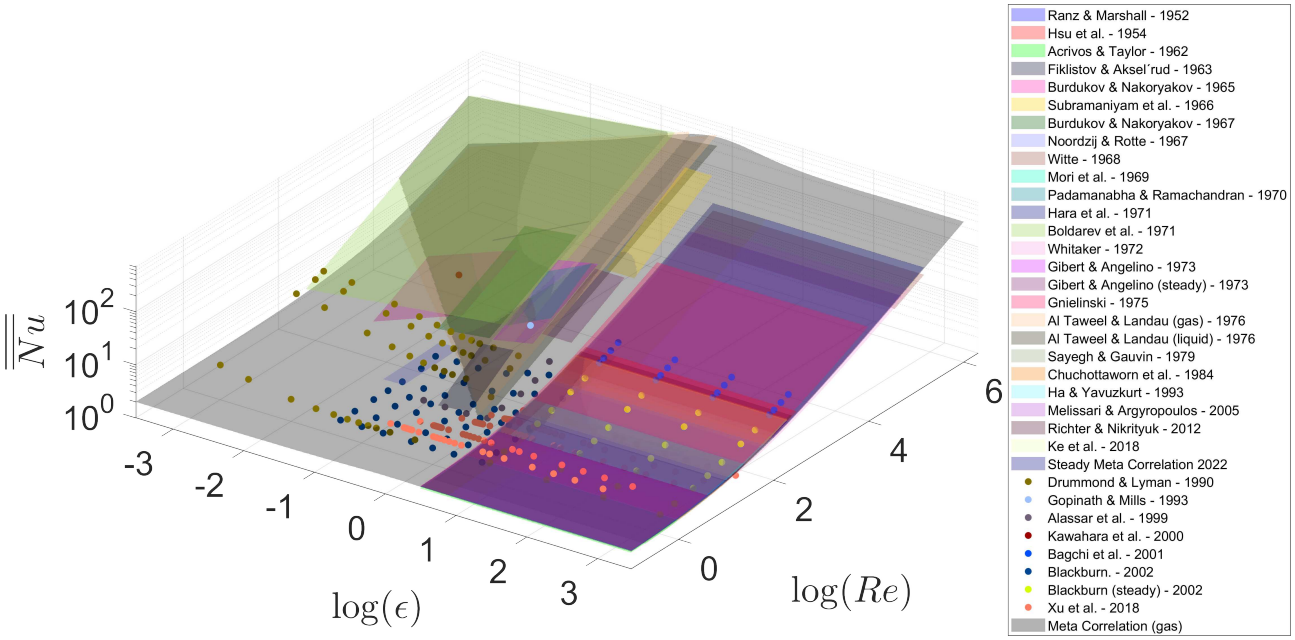

Figure 7.3. Nusselt number averaged over the particle surface and averaged over one oscillation cycle predicted by various investigated models plotted in the ϵ-Re plane. Additionally, Meta Correlation 7.4 for gaseous environments is plotted, while the Prandtl number is set to $Pr = 0.71$ as is found with air at STP.

of the HMT at $\epsilon \approx 1$, which is suggested by several models, is described by term 'D'. By form, the standard normal distribution of a probability density function was utilized here. It describes the enhancement of the HMT at $\epsilon \approx 1$ well, especially for $\epsilon < 1$. The expectation and the standard deviation were fitted well to values of zero and unity, respectively. This term also differs for gases and liquids, mostly in order to offset the difference in Term 'C' and to ensure model consistency. The split of correlations in the Steady Streaming area for gases and liquids in Figure 7.3 is noticeable, especially with their different asymptotic behaviour for $\epsilon \to 0$, while the asymptotic behaviour for gases is captured well with Meta Correlation 7.4.

7.5. Deviations

Figure 7.4 shows the deviations of Meta Correlations 7.4 and 7.5 from the respective individual models. The colored bars show the $NRMSD$, calculated with Equation 7.2,

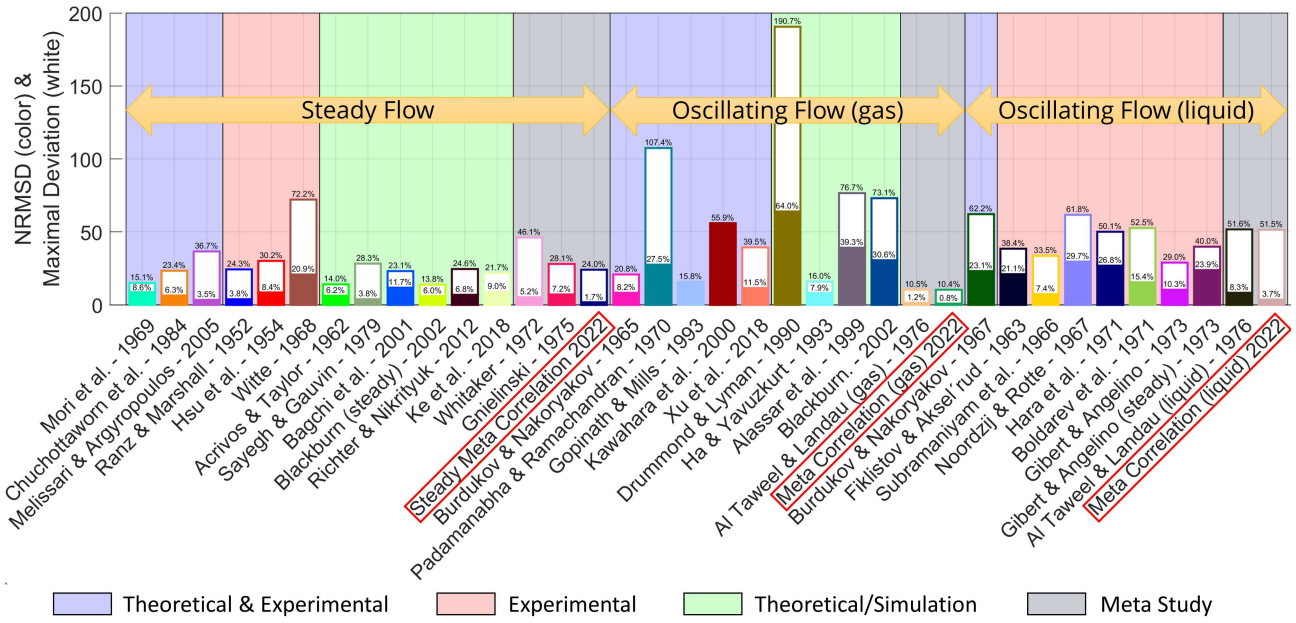

Figure 7.4. Deviations from Meta Correlations 7.4 and 7.5 from the respective individual models investigated and listed in Table 7.1. The colored bars show the $NRMSD$, calculated with Equation 7.2, while the white bars highlight the maximum normalized deviation. The deviation presented for Meta Correlations 7.4 and 7.5 is for all investigated models and data combined.

while the white bars highlight the maximum normalized deviation. Meta Correlations 7.4 and 7.5 deviate insignificantly from Steady Meta Correlation 7.3 and from the investigated steady models in general, as pointed out in Section 7.2. While the correlations for steady flow behave very similarly, this is not so clear for oscillating flows. Besides the mentioned necessity for a distinction between gaseous and liquid flows, due to their different asymptotic behaviour, the overall measured and simulated data diverge substantially. Drummond & Lyman are the obvious outlier here since they are the only authors who predicted an increase of HMT intensity with a decreasing amplitude parameter ϵ, which

is also reflected in a large deviation of their data. Blackburn **[109]** commented on this study and suggested that the mesh resolution near the surface of the sphere might be too low. This would result in the inability to capture the flow behaviour for small oscillation amplitudes properly. The other models for oscillating flow, which often cover the same region of the plane, deliver scattered data. This implies an insufficient experimental or simulation design by many authors, or additional dependencies beyond solely the oscillation Reynolds number and the amplitude parameter, contrary to the consensus in the literature. Nevertheless, based on the currently available data, Meta Correlations 7.4 and 7.5 are viable, especially with regard to the large parameter ranges covering several orders. This is also reflected in their $NRMSD$ from all combined data of 0.8% for gases and 3.7% for liquids. Additionally, Meta Correlations 7.4 and 7.5 only slightly deviate from the previous meta analyses in their respective part of the plane (1.2% for gases and 8.3% for liquids).

7.6. Quasi-Steady Assumption

The quasi-steady assumption is often applied in the literature for the HMT to particles in oscillating flows. Figure 7.5 shows a comparison of Meta Correlation 7.4 with the derived Steady Correlation 7.3. It shows that the quasi-steady approach is only valid for $\epsilon \gg 1$ or $Re < 1$. For $\epsilon \approx 1$, it under-predicts the intensity of the HMT, while it over-predicts the intensity of the HMT for $\epsilon \ll 1$ and $Re \gg 1$.

7.7. Heat and Mass Transfer to Small Particles

Similar to the drag at particles smaller than d<1 µm,as discussed in Section 5.6, non-continuum effects need to be taken into account for the HMT to small particles as well. The retroactive effect of momentum transfer also influences heat transfer. While an imagined slip (jump in fluid velocity at the surface of the particle) was introduced in

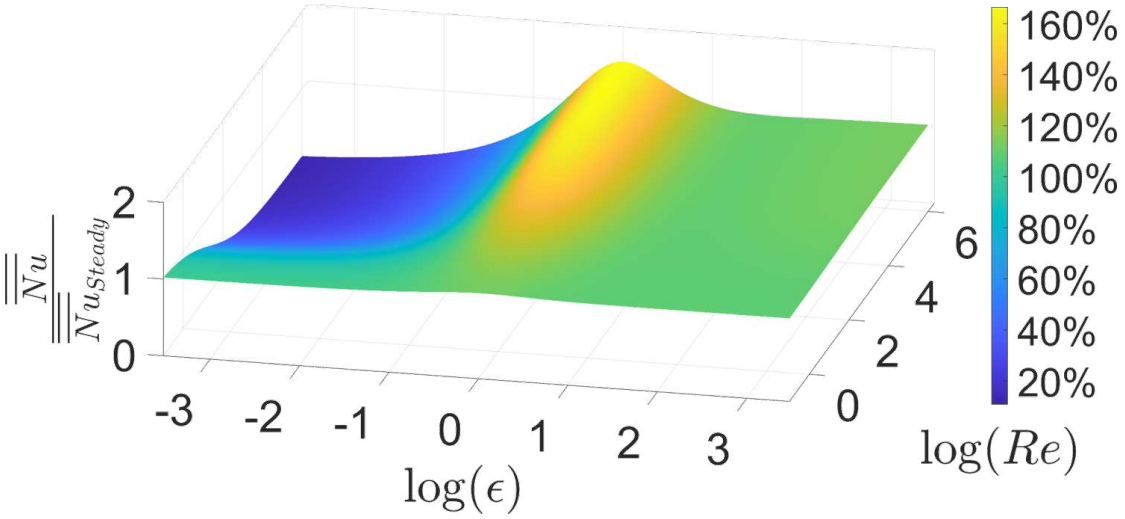

Figure 7.5. Comparison of Meta Correlation 7.4 with Steady Correlation 7.3.

the case of reduced drag in order to help with the concept, here the change in momentum transfer behaves as a temperature jump at the surface of the particle. This concept is displayed on the left side of Figure 7.6. For the conductive limit ($U \to 0$) it can be calculated with **[135]**

$$T(r) = T - \frac{T - T_p}{1 + \frac{4\kappa}{\kappa+1}\frac{2-\sigma_T}{\sigma_T}\frac{Kn}{Pr}}\frac{a}{r} \tag{7.6}$$

with the corresponding Nusselt number

$$Nu = \frac{2}{1 + \frac{4\kappa}{\kappa+1}\frac{2-\sigma_T}{\sigma_T}\frac{Kn}{Pr}} \tag{7.7}$$

Here, σ_T is the thermal accommodation coefficient (TAC) and κ the specific heat capacity ratio. Very small particles (d<1 µm) fall in the fast relaxation limit in most circumstances, as introduced in Section 5.3, leading to a negligible slip velocity between particle and fluid. This means that very small particles will always be close to a vanishing slip velocity and the conductive limit regarding the HMT, bringing the possibility to calculate the Nusselt number with Equation 7.7. The right side of Figure 7.6 shows

the Nusselt number in respect to the Knudsen number, while the Prandtl number is set to $Pr = 0.71$ and the specific heat capacity ratio to $\kappa = 1.4$, as found with air at STP. The TAC is set to 0.61 as suggested by Dharmadurai [**193**] for air even though the TAC is influenced by a plethora of factors, e.g. surface rough roughness of the particle [**194**]. The Nusselt number decreases with increasing Knudsen number (with decreasing particle diameter). In contrast to this stands the decrease of particle drag and the resulting increase in slip velocity and increase in HMT with increasing Knudsen number, as pointed out by Mohajer et al. [**133**]. They concluded that, for a small temperature difference between particle and fluid, the increased slip velocity has a larger effect on the HMT than the temperature jump and vice versa. In addition to the Nusselt number, the Cunningham factor for slip correction is plotted on the right side of Figure 7.6.

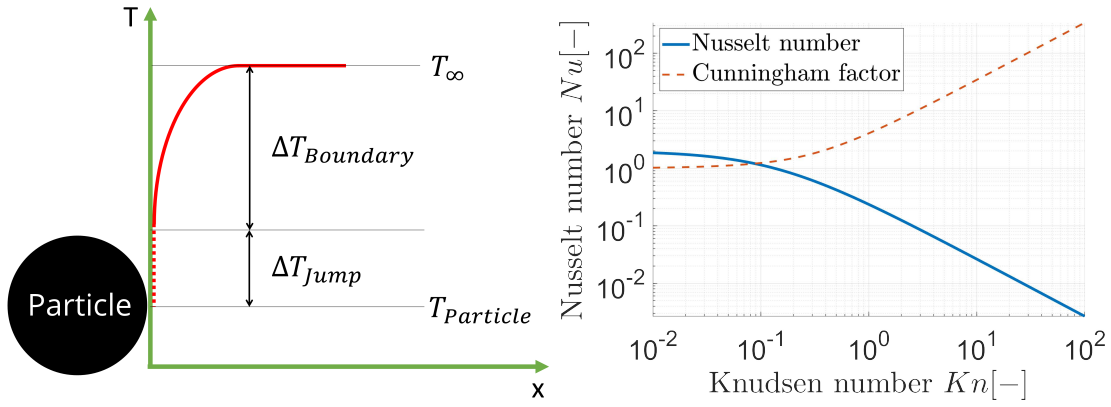

Figure 7.6. Temperature jump at small particles (d<1 µm). **left:** Scheme of the imagined temperature jump and its effect on the temperature distribution in the vicinity of small particles. **right:** Plot of Relation 7.7 and Cunningham factor in respect to the Knudsen number. The Prandtl number is set to $Pr = 0.71$ and the specific heat capacity ratio to $\kappa = 1.4$, as found with air at STP. The TAC is set to 0.61.

7.8. Conclusion of Heat and Mass Transfer to Particles

33 data sets from the literature were correlated into a meta correlation, covering the entire plane. First, the area of quasi-steady HMT was defined and then a steady

meta correlation for this part of the plane was found by correlating 14 data sets from the literature. This meta correlation was then utilized along with 19 data sets for the HMT to particles in oscillating flows in order to derive two meta correlations - one for gaseous and one for fluid environments. With an overall $NRMSD$ of 0.8% for an gaseous environment and 3.7% for an fluid environment, the meta correlations can be considered in good agreement with the data. The major insights of this chapter, besides the utility of the meta correlations, are the enhanced HMT up to 60% for an amplitude parameter of $\epsilon \approx 1$ and the reduced HMT for $\epsilon \ll 1$ compared with the quasi-steady approach. Finally, it was laid out how to deal with non-continuum effects influencing the HMT to small particles.

CHAPTER 8

Summary & Discussion

The pulsation reactor was introduced as an apparatus for particle treatment in a pulsating hot gas stream. It was pointed out that despite being in use in the industry for several decades, the processes in the reactor and at the level of the single particle are not yet fully understood. One of these aspects is the heat and mass transfer to particles in the pulsating fluid. Therefore, a three stage model (particle motion, flow patterns, and HMT) was derived in order to predict the HMT to a single particle in such a flow. The starting point of the model were the five central input parameters that characterize the particle flow interaction: fluid velocity amplitude, pulsating frequency, fluid temperature, particle size, and particle density. After providing an overview of the state of the research on this topic, the basic assumptions and considerations were laid out, before the model itself was explained. The model itself and the interaction of the three stages of the model is summarized in the following section by describing the algorithm to determine the HMT to the particle. Afterwards, the influence of the five input parameters on the HMT to the particle is discussed in Section 8.2. Since the model utilizes few input parameters with a very broad value range, far exceeding the physical capabilities of pulsation reactors, the HMT in pulsating flows within the limitations of pulsation reactors is discussed in Section 8.3. This is followed by a more general discussion on the advantages and shortcomings of the model in Section 8.4 and possible ways to overcome the shortcomings and improve the model in Section 9.

8.1. Model Algorithm

The model algorithm is presented here, enabling a structured approach to determining the HMT intensity from oscillating flows to entrained particles. The important steps are visualized in Flow Chart 8.1. This algorithm can also be applied to a pulsating flow, in case the transient part of the slip velocity can be neglected, as shown in Section 4.4. The presented model utilizes the input parameters (fluid velocity amplitude, frequency, fluid temperature, particle diameter, particle density). Those can be partly exchanged for other quantities as demonstrated in Section 4.1. The input parameters can be interpreted as process conditions in a pulsation reactor or ultra sonic levitator, as pointed out in Figure 2.2, while they translate into several dimensionless numbers via the relations in Figure 4.8. The meaning of the important dimensionless numbers is discussed in Section 4.6, but the oscillation Reynolds number Re and the amplitude parameter ϵ are highlighted here. They span a plane, as derived in Section 4.7, and completely define the motion of the particle in the oscillating flow, as long as particle relaxation can be neglected. The intensity of occurring particle relaxation can be determined with the help of the Womersley number Wo^2 and the density ratio γ via the relations in Table 5.1 and Figure 5.3. In case the density ratio falls between the density ratio for the FRL and SRL, which both depend on the Womersley number, $\gamma_{crit,FRL}(Wo^2) \leq \gamma \leq \gamma_{crit,SRL}(Wo^2)$, particle relaxation needs to be taken into account. In this case, a drag model with an appropriate validity range must be utilized in order to determine the slip velocity amplitude. Several drag models are presented in Section 5.1 and cover large parts of the plane as displayed in Figure 5.1. The slip velocity amplitude can now be calculated for large parts of the plane with the relations in Table 5.1, while the density ratio functions as a parameter of the plane. Many drag models are derived through asymptotic analysis and it is not explicit what constitutes a sufficient extreme value for

the suggested simplifications, as discussed in Section 5.5. Therefore, analytic relations are provided in order to calculate the deviations between the simple Stokes model and the other models in Table 5.3. Additionally, criteria are provided for the deviation to stay below 5%, which are graphically displayed in Figure 5.6. In case these criteria are met, the Stokes model can be utilized regardless of its range of validity. In case the approximate position on the plane is not known for an input parameter combination, the Stokes model can be used in order to deduce an educated guess on the position and then recalculate with an appropriate drag model, if necessary. For a particle with small diameter ($d \leq 1\,\mu m$), non-continuum effects start to emerge, as discussed in Section 5.6. In this case, the drag terms in each model need to be corrected with the Cunningham factor C_C, acting as a parameter of the plane. With the determination of the slip velocity complete, the exact position on the plane is known. Table 5.2 together with Figure 5.5 provide the possibility to roughly but simply navigate the plane.

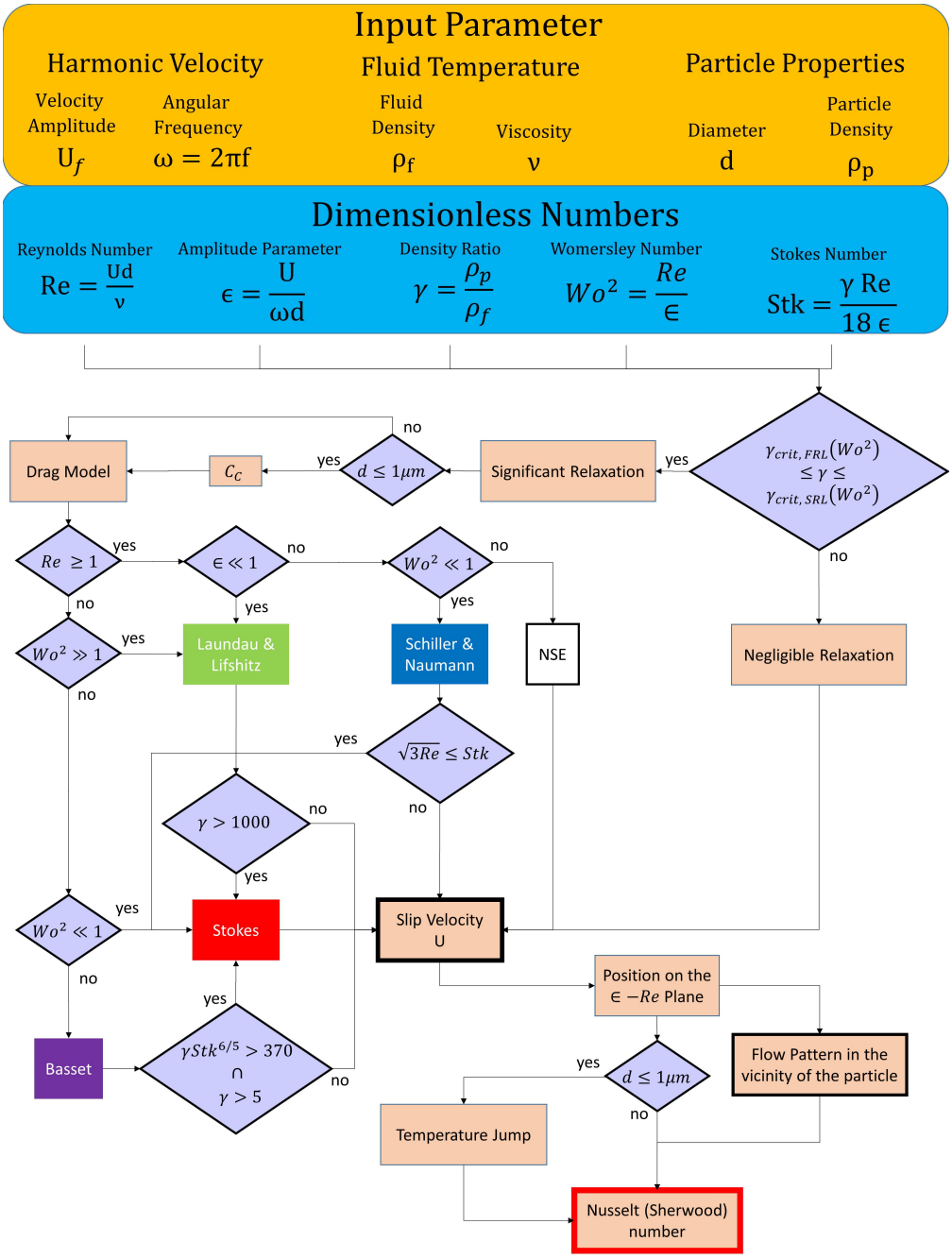

Figure 8.1. Flow Chart of the model algorithm for determining the Nusselt or Sherwood number for a particle in an oscillating (pulsating) flow.

The characteristics of the flow pattern in the vicinity of the particle are linked to the value of oscillation Reynolds number and amplitude parameter, as described in Section 6. Therefore, knowledge of the position on the plane enables direct inference of the flow pattern around the particle, as pointed out in Figure 6.6. Conclusions can be drawn from the characteristics of the flow pattern on the intensity of occurring HMT, but this step in the modelling process is optional, since the intensity of the HMT is already determined by the position on the plane. As soon as the oscillation Reynolds number and the amplitude parameter are determined, Meta Correlation 7.4 or 7.5 can be employed, for a gaseous or liquid fluid, respectively, and together with the Prandtl or the Schmidt number, the Nusselt or the Sherwood number can be calculated directly. The Nusselt number for gas is plotted in Figure 7.3, while Figure 7.5 provides good insights on the locations of areas of enhanced, reduced, and unaffected HMT intensity in the plane, compared with a steady flow. In cases dealing with a very small particle ($d \leq 1\,\mu\text{m}$), the Nusselt number can be calculated with Equation 7.7 in the conductive limit.

8.2. Influence of input parameters on the HMT

This is a discussion on the influence of the five input parameters from Table 4.1 on the HMT to the particle. The sensitivity of the input parameters on the position on the plane (Figure 5.5) and the HMT intensity to a particle in an oscillating flow compared with a steady flow (Figure 7.5) are displayed in Figure 8.2 again, side by side, for convenient comparison. However, Figure 7.5 displays the HMT intensity in relation to the HMT in a steady flow and not the actual Nusselt number, which would be Figure 7.3. For a more quantitative analysis Table 5.2 can be consulted, instead of the graphical interpretation of the sensitivities in Figure 5.5. Note that the sign, orientation, and length of the red vectors are only valid for gases, as highlighted in Section 5.4. The impact of input

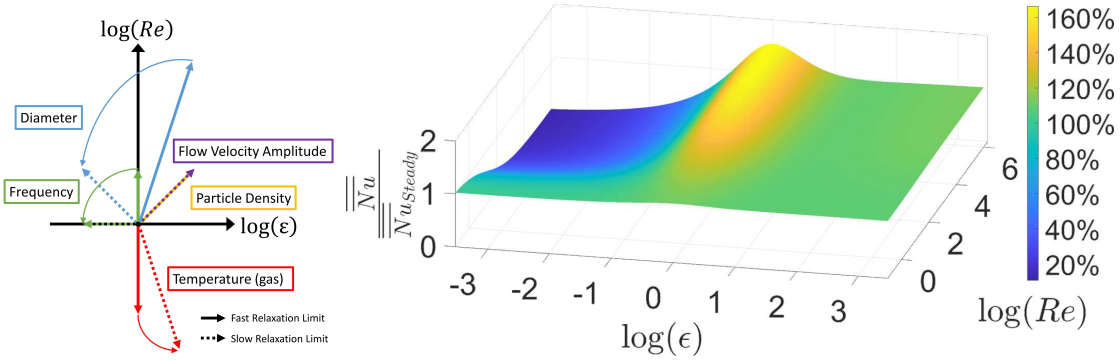

Figure 8.2. Influence of input parameters on the heat and mass transfer to the particle, emphasised by direct comparison of Figure 5.5 and Figure 7.5.

parameters is discussed in terms of the fast relaxation limit (FRL) and slow relaxation limit (SRL), as presented in Section 5.3.

Particle Diameter

The diameter of the particle has the largest influence on the position on the ϵ-Re plane, especially towards the FRL. Even in the SRL, the influence is substantial and always has a positive component in the Re direction. This implies that the particle diameter has the largest influence on the HMT to the particles as well, since a large Reynolds number is associated with high HMT, as long as the amplitude parameter ϵ is not much smaller than unity. While, for the FRL, the influence of the particle diameter on the amplitude parameter is substantial in the positive ϵ direction, it changes sign in the relaxation area and has the same influence in the negative ϵ direction at the SRL. This combination leads to large particles being at risk of occupying a position in the low HMT area of the plane when not compensated for with the other input parameters.

Frequency

The frequency affects the position on the plane solely in the positive Re direction in the FRL, while it effects solely the negative ϵ direction in the SLR. This implies that a combination of both influences occurs in the relaxation area. In the FRL, an increase

in frequency results in pure increase of Reynolds number and therefore Nusselt number. The frequency is the only option in order to actively shift the position of small particles to smaller amplitude parameters, even though its impact is limited.

Temperature

The fluid (gas) temperature has a large influence in the negative Re direction (all relaxation cases), while it is especially large for the SRL, which is due to a change in fluid viscosity. In this case, it also has a slight positive influence in the ϵ direction due to a change in fluid density.

Velocity Amplitude

Completely independent of particle relaxation, an increase in flow velocity amplitude will always lead to an equal increase in ϵ and Re.

Particle Density

The particle density behaves similarly to the velocity amplitude. It has no influence in the SRL, but the same influence as the velocity amplitude in the FLR of increasing ϵ and Re to the same degree.

8.3. The ϵ-Re Plane in the Special Case of the Pulsation Reactor

In order to fully utilize the potential of the pulsation reactor as an apparatus for the synthesis of high performance materials with configurable material properties, the HMT at the particle must become adjustable itself. Often the goal is to maximize the heat and mass transfer in order to enhance the effect of the shock-like treatment with its short residence times, which are characteristic of pulsation reactors. However, a reduced HMT can be utilized to influence occurring chemical reactions as well. In both cases, an adjustable HMT is desirable. This can be achieved theoretically by following the algorithm summarized in Section 8.1 and then to change the process conditions in a PR accordingly.

While the ϵ-Re plane provides valuable insights for all parameter ranges, only certain areas are accessible in pulsation reactors, due to physical and constructional constraints. In order to investigate the potential of a PR, the extreme values of the achievable process conditions in a PR, as listed in Table 2.1, are used as input parameters for the presented model and the algorithm from Section 8.1 is applied. A visualisation of the reachable locations on the ϵ-Re plane can be seen in Figure 8.3. Here, the color code of the background indicates the Nusselt number at the respective location. In the foreground, different frequencies are indicated by the shape of the marker, while the particle diameter is differentiated by marker color. The density of the particle is displayed by the marker edge color. Low and high fluid velocity amplitudes are highlighted by the thickness of the marker edge, while high fluid temperatures are indicated by a magenta circle around the marker. The upper and lower extreme value of the parameters were utilized, while also an intermediate particle diameter was applied. Also, an oscillation frequency of 1 MHz is displayed, which can not be achieved with conventional pulsation reactors, but is rather the high end for ultra sonic apparatus, e.g. ultra sonic levitators (USL). These devices create process conditions similar to those of a PR in terms of velocity behaviour and are the focus of many scientific investigations and publications [**86**]. The influences of the input parameters behave as explained in Section 5.4. The particle diameter has by far the largest influence, while simultaneously spanning the largest parameter range of six orders here. In the FRL (mirco and nano sized particles), the particle diameter dominates the influence on the Reynolds number, while when moving into the relaxation regime and the SRL (milli sized particles) the influence towards the amplitude parameter becomes more pronounced. The influence of the pulsation frequency on the Reynolds number is quite noticeable in the FRL, but the influence on the amplitude parameter in

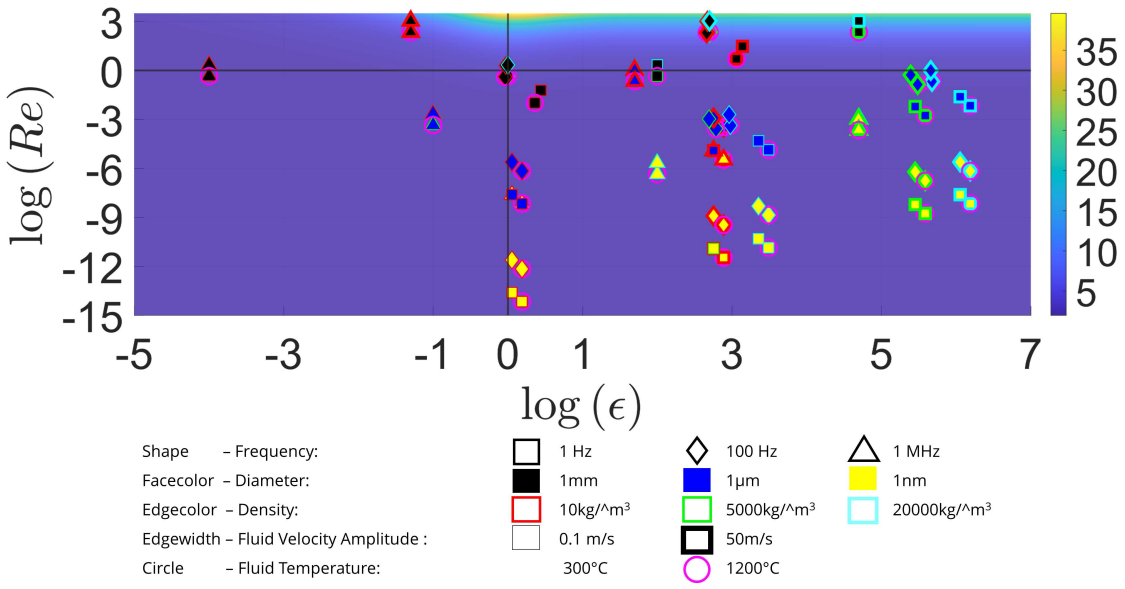

Figure 8.3. Locations on the ϵ-Re plane with extreme value combinations for the pulsation reactor, as listed in Table 2.1. Different frequencies are indicated by the shape of the marker, while the particle diameter is differentiated by marker color. The density of the particle is displayed by the marker edge color. Low and high fluid velocity amplitudes are highlighted by the thickness of the marker edge, while high fluid temperatures are marked by a magenta circle around the marker. The color code of the background indicates the Nusselt number at the respective location.

the SRL is remarkable, even though the frequency only spans two orders here. As derived earlier, the particle density is influential in the FRL, but becomes negligible in the SRL. The fluid velocity amplitude spans almost 3 orders here, which translates directly to the Reynolds number and the amplitude parameter alike, independent of the position on the plane, hence the occurring relaxation. Even though the gas temperature (PRs are only operated with gases) has a strong nominal influence on the position in the plane, it spans not even half an order here and, therefore, its influence is minimal. But still, the behaviour of only influencing the Reynolds number in the SRL and influencing also the amplitude parameter in the FRL by temperature can be observed.

It was derived that the achievable Reynolds number and amplitude parameter, even with the extension of USL, are mainly confined to the fourth quadrant of the ϵ-Re plane,

which is especially true for micro sized particles and smaller. These small (and therefore non-inert) particles follow the flow almost perfectly, allowing for an only vanishing small slip velocity between particle and fluid. This translates into a small oscillation Reynolds number, and to the conductive (diffusive) limit of $\overline{\overline{Nu}}(\overline{\overline{Sh}}) = 2$ for the HMT at the particle. In case of particles smaller than micrometer size, this is even lower due to non-continuum effects and the temperature jump discussed in Section 7.7. For millimeter size particles, Reynolds numbers of up to 1000 can be achieved, resulting in a drastically increased HMT compared with steady flow reactors (e.g. entrained flow reactors). A further enhanced HMT due to the flow conditions was found at $\epsilon \approx 1$, on top of the enhanced HMT due to an persistent slip velocity, as derived in Chapter 7. The pulsation frequency provided by a PR enables these amplitude parameters to be achieved, but only in combination with small flow velocity amplitudes. This is due to high flow velocities leading to high amplitude parameters, as well as high Reynolds numbers, necessary for a meaningful enhancement of HMT intensity. High velocity amplitudes could be offset in order to return to the area of $\epsilon \approx 1$, with even higher pulsation frequencies, which can be found with USLs, but not PRs. Similarly, high particle densities result in larger ϵ, where the flow can be modelled as quasi-steady and an increase in HMT results from a constant quasi-steady slip velocity only. The fluid temperature can only be varied minimally in a PR compared with the other parameters, and has therefore little influence on the location in the ϵ-Re plane as well. Since this is the most crucial parameter for many possible chemical reactions at the particle, the temperature should be chosen according to this basis and not in order to shift the position on the plane.

8.4. Discussion

A model was presented which enables enables the estimation of particle motion and the occurring heat and mass transfer at single particles in one-dimensional oscillating

flows. It can be utilized for many cases of a pulsating flow as well. The model utilizes a few input parameters (fluid temperature, fluid velocity amplitude, oscillation frequency, particle diameter, particle density), with large ranges. It revolves around two central dimensionless numbers: the oscillation Reynolds number and the amplitude parameter. These span a plane, enabling direct visual access to the model and providing an intuitive way of interacting with the model. This plane has so far only been utilized in the literature to discuss qualitative asymptotic analyses, but not yet for a quantified approach. Also, only parts of the plane were approached or discussed individually, while this work treats the plane comprehensively. It can best be utilized as a tool in order to find the position on the plane for a set of input parameters and to gain a general direction on how to change the input parameters in order to change the position on the plane and the resulting HMT accordingly. This work provides an easy to implement model for the consideration of HMT to particles in oscillating and pulsating flows. It draws from various sources in the literature, which are often on an abstract mathematical basis and cover only small parts of the whole picture. This work unites those many approaches on a shared graphical basis with the ϵ-Re plane, while displaying the algorithm as accessibly as possible for the end using process engineer.

Even though the model brings a lot of value for the discussion on the HMT to particles, some limitations for applications must be pointed out. A central feature of the model is the simplification of transferring from a pulsating to an oscillating flow. This is possible in many cases, especially for long periods of consideration. Pulsation reactors often apply a shock-like treatment to the material, where the first contact between gas and particles and the initial particle relaxation can be crucial. In these cases, the transient part can still be significant and the effects on the HMT can be better estimated without this simplification. Often the heat up of the particles is almost instantaneous, especially for

small particles, while a possible mass transfer occurs over a longer time period. Therefore, in such a case, it is questionable whether the heat transfer should be calculated with the model, but a calculation of the mass transfer would be reasonable. In contrast, the model can be applied to particles in USLs in all circumstances, since the transient effects wear off much faster than the observation period is long. Even though the absolute velocity profiles in a pulsation reactor resonance tube are generally as displayed in Figure 4.1, no information about the degree of turbulence is conveyed. While the center part of the flow behaves like a plug, it still can have a substantial degree of turbulence in some cases [**195**]. The presented model assumes a harmonic, one-dimensional flow velocity, which might not be sufficient if the size of the particle matches the dimensions of the eddies. There, the slip velocity between particle and gas can be substantially higher than predicted by the model, affecting the HMT to the particle as well. Again, the model can be applied to particles in USLs, since the fluid dynamic case of $\epsilon \ll 1$ is covered by the model. The model predicts (substantiated by the literature) an increased HMT to the particle for an amplitude parameter of $\epsilon \approx 1$ and an oscillation Reynolds number of $Re \gg 1$ compared with the quasi-steady case. At this point in time it is not possible to create suitable process conditions (input parameter combinations) in a PR to capitalise on this effect. This leaves only the enhanced heat and mass transfer due to a sustained slip velocity between particle and gas in a PR compared with an entrained flow reactor, which has already a substantial effect in most cases. This implies that the HMT to particles in a pulsation reactor can be sufficiently modelled under the quasi-steady assumption. This is not the case for considerations of high oscillation frequencies, e.g. with USLs, or particles with larger diameters.

CHAPTER 9

Outlook

The presented model provides insights into the occurring heat and mass transfer to solid particles in one-dimensional oscillating flows. One of its main features is the comprehensive analytical approach and mathematical accessibility. Many further, interesting phenomena could be investigated by adding sub models, which, however, would often result in the loss of this feature. Nevertheless, the model could be further aligned with the special conditions in a pulsation reactor, namely by modelling the shock-like treatment when particles have first contact with the hot gas. Additionally, a way could be found in order to incorporate various degrees of turbulence which might occur in a pulsation reactor. Often, pulsation reactors are operated by spraying the product precursors solved in a combustible carrier into the the resonance tube. Therefore, the model could be improved by working in corrections for liquid droplets, e.g. via the work of Sirignano [**196**], namely droplet deformation and reduced drag, due to internal back flow. Another interesting point to consider could be the effect of pressure oscillations on the integrity of the droplet. There could be a high heat transfer during a high pressure phase, heating the droplet up to the boiling point. The following pressure drop could result in an explosive vaporization of the droplet, leading to nano sized particles found with pulsation reactor synthesis. Some additional insights could be gained in considering the decrease of the droplet diameter on the particle trajectory along the resonance tube.

References

[1] C. Hoffmann and M. Ommer, "Reaktoren für Fluid-Feststoff-Reaktionen: Pulsationsreaktoren," in *Handbuch Chemische Reaktoren* (W. Reschetilowski, ed.), Springer Reference Naturwissenschaften, pp. 1–19, Springer Berlin Heidelberg and Springer Spektrum, 2019.

[2] Hermann von Helmholtz, "On the sensations of tone as a physiological basis for the theory of music," *Nature*, vol. 12, no. 308, pp. 449–452, 1875. PII: BF012449a0.

[3] M. Alster, "Improved calculation of resonant frequencies of Helmholtz resonators," *Journal of Sound and Vibration*, vol. 24, no. 1, pp. 63–85, 1972. PII: 0022460X7290123X.

[4] T. Kudra, "Pulse-combustion drying: Status and potentials," *Drying Technology*, vol. 26, no. 12, pp. 1409–1420, 2008.

[5] S. Fraenkel, J. Nogueira, J. Carvalho, and F. Costa, "Heat transfer coefficients for drying in pulsating flows," *International Communications in Heat and Mass Transfer*, vol. 25, no. 4, pp. 471–480, 1998. PII: S0735193398000347.

[6] S. Heidinger, F. Spranger, J. Dostál, C. Zhang, and C. Klaus, "Material treatment in the pulsation reactor - from flame spray pyrolysis to industrial scale," *Sustainability*, vol. 14, no. 6, p. 3232, 2022. PII: su14063232.

[7] C. Klaus, K. Wegner, T. Rammelt, and M. Ommer, "New challenges in thermal processing," *Interceram - International Ceramic Review*, vol. 70, no. 1, pp. 22–25, 2021. PII: 443.

[8] J. Dostál, S. Heidinger, C. Klaus, S. Unz, and M. Beckmann, "Effects of fuel input on pulsation reactor behavior - an experimental study," *Processes*, vol. 11, no. 2, p. 444, 2023.

[9] B. T. Zinn, "Pulse combustion: Recent applications and research issues," *Symposium (International) on Combustion*, vol. 24, no. 1, pp. 1297–1305, 1992. PII: S0082078406801517.

[10] X. Meng, W. de Jong, and T. Kudra, "A state-of-the-art review of pulse combustion: Principles, modeling, applications and R&D issues," *Renewable Sustainable Energy Rev*, vol. 55, pp. 73–114, 2016. PII: S1364032115011892.

[11] S. Großgebauer, *Mathematische Modellierung und experimentelle Untersuchung von selbstständig pulsierenden Brennern zur Stoffbehandlung*. Phd-thesis, Technische Universität Dresden, 2008.

[12] Klaus, C., K Wegner, and M Ommer, "Partikelsynthese im Pulsationsreaktor - von der Idee zur Produktion," in *30. Deutscher Flammentag*, pp. 582–590, 2021.

[13] S. Begand, B. Dahm, and S. Ambrosius, "The pulsed reactor for processing in the chemical industry," *Chemical Engineering & Technology*, vol. 21, no. 5, p. 420, 1998.

[14] S. Begand, *Herstellung nanoskaliger Oxidpulver durch thermisch gesteuerte Synthese in einem Pulsationsreaktor*. Phd-thesis, der Naturwissenschaftlich-Technischen Fakultät der Chemie, Pharmazie und Werkstoffwissenschaften der Universitat des Saarlandes, 2001.

[15] Z. Wu and X. Liu, "Simulation of spray dying of a solution atomized in a pulsating flow," *Drying Technology*, vol. 20, no. 6, pp. 1101–1121, 2002.

[16] A. B. Basset, "On the motion of a sphere in a viscous liquid," *Philosophical Transactions of the Royal Society of London. (A.)*, vol. 179, pp. 43–63, 1888.

[17] J. Boussinesq, "Sur la resistance quoppose un liquide indefini en repos, sans pesanteur, au movement varie d'une shere solide," *CR Acad. Sci. Paris*, vol. 100, pp. 985–937, 1885.

[18] C. W. Oseen, *Neuere Methoden und Ergebnisse in der Hydrodynamik*, vol. 1. Akademische Verlagsgesellschaft MBH, 1927.

[19] C. M. Tchen, *The motion of small particles suspended in a turbulent flow*. PhD thesis, Delft University of Technology, 1947.

[20] M. R. Maxey, "Equation of motion for a small rigid sphere in a nonuniform flow," *Physics of Fluids*, vol. 26, no. 4, p. 883, 1983.

[21] A. T. Hjelmfelt and L. F. Mockros, "Motion of discrete particles in a turbulent fluid," *Applied Scientific Research*, vol. 16, no. 1, pp. 149–161, 1966.

[22] K. W. Chan, M. Baird, and G. F. Round, "Motion of a solid sphere in a horizontally oscillating liquid," *Chemical Engineering Science*, vol. 29, no. 7, pp. 1585–1592, 1974. PII: 0009250974870090.

[23] C. F. M. Coimbra and R. H. Rangel, "Spherical particle motion in harmonic stokes flows," *AIAA Journal*, vol. 39, no. 9, pp. 1673–1682, 2001.

[24] W. B. Krantz, J. F. Carley, and A. M. Al Taweel, "Levitation of solid spheres in pulsating liquids," *Industrial & Engineering Chemistry Fundamentals*, vol. 12, no. 4, pp. 391–396, 1973.

[25] E. B. Tunstall and G. Houghton, "Retardation of falling spheres by hydrodynamic oscillations," *Chemical Engineering Science*, vol. 23, no. 9, pp. 1067–1081, 1968. PII: 0009250968870927.

[26] P. A. Hwang, "Fall velocity of particles in oscillating flow," *Journal of Hydraulic Engineering*, vol. 111, no. 3, pp. 485–502, 1985.

[27] S. Ikeda and M. Yamasaka, "Fall velocity of single spheres in vertically oscillating fluids," *Fluid Dynamics Research*, vol. 5, no. 3, pp. 203–216, 1989.

[28] G. Houghton, "Particle trajectories and terminal velocities in vertically oscillating fluids," *The Canadian Journal of Chemical Engineering*, vol. 44, no. 2, pp. 90–95, 1966.

[29] O. Molerus, "Teilchenbewegung in einem pulsierenden Strömungsfeld," *Chemie Ingenieur Technik*, vol. 36, no. 8, pp. 866–870, 1964.

[30] G. Houghton, "The behaviour of particles in a sinusoidal velocity field," *Proceedings of the Royal Society of London. Series A. Mathematical and Physical Sciences*, vol. 272, no. 1348, pp. 33–43, 1963.

[31] G. Houghton, "Particle retardation in vertically oscillating fluids," *The Canadian Journal of Chemical Engineering*, vol. 46, no. 2, pp. 79–81, 1968.

[32] R. A. Herringe, "On the motion of small spheres in oscillating liquids," *The Chemical Engineering Journal*, vol. 11, no. 2, pp. 89–99, 1976. PII: S0300946776800305.

[33] M. Abbad and M. Souhar, "Effects of the history force on an oscillating rigid sphere at low reynolds number," *Experiments in Fluids*, vol. 36, no. 5, pp. 775–782, 2004. PII: 288FM796692VCJBL.

[34] F. Odar and W. S. Hamilton, "Forces on a sphere accelerating in a viscous fluid," *Journal of Fluid Mechanics*, vol. 18, no. 02, p. 302, 1964.

[35] E. E. Michaelides, "Review - the transient equation of motion for particles, bubbles, and droplets," *Journal of Fluids Engineering*, vol. 119, no. 2, pp. 233–247, 1997.

[36] Y. Tsuji, N. Kato, and T. Tanaka, "Experiments on the unsteady drag and wake of a sphere at high reynolds numbers," *International Journal of Multiphase Flow*, vol. 17, no. 3, pp. 343–354, 1991. PII: 030193229190004M.

[37] S. K. Karanfilian and T. J. Kotas, "Drag on a sphere in unsteady motion in a liquid at rest," *Journal of Fluid Mechanics*, vol. 87, no. 1, pp. 85–96, 1978. PII: S0022112078002943.

[38] M. Baird, M. G. Senior, and R. J. Thompson, "Terminal velocities of spherical particles in a vertically oscillating liquid," *Chemical Engineering Science*, vol. 22, no. 4, pp. 551–558, 1967. PII: 0009250967800381.

[39] R. Mei, "Flow due to an oscillating sphere and an expression for unsteady drag on the sphere at finite reynolds number," *Journal of Fluid Mechanics*, vol. 270, pp. 133–174, 1994. PII: S0022112094004222.

[40] F. Odar, *Verification of the proposed equation for calculation of the forces on a sphere accelerating in a viscous fluid*, vol. 190. US Army Materiel Command, Cold Regions Research & Engineering Laboratory, 1966.

[41] R. Mei, C. J. Lawrence, and R. J. Adrian, "Unsteady drag on a sphere at finite reynolds number with small fluctuations in the free-stream velocity," *Journal of Fluid Mechanics*, vol. 233, pp. 613–631, 1991. PII: S0022112091000629.

[42] R. Mei and R. J. Adrian, "Flow past a sphere with an oscillation in the free-stream velocity and unsteady drag at finite reynolds number," *Journal of Fluid Mechanics*, vol. 237, pp. 323–341, 1992. PII: S0022112092003434.

[43] L. D. Landau and E. M. Lifshitz, *Fluid mechanics*, vol. v.6 of *Course of theoretical physics*. Pergamon, 2nd ed. ed., 1987.

[44] V. K. Gupta, G. Shanker, and N. K. Sharma, "Experiment on fluid drag and viscosity with an oscillating sphere," *American Journal of Physics*, vol. 54, no. 7, pp. 619–622, 1986.

[45] J. W. Strutt, "On the circulation of air observed in Kundt's tubes, and on some allied acoustical problems," in *Scientific Papers*, pp. 239–257, Cambridge university press, null.

[46] H. Schlichting, "Berechnung ebener periodischer Grenzschichtströmungen," *Phys. Z.*, vol. 33, pp. 327–335, 1932.

[47] J. M. Andres and U. Ingard, "Acoustic Streaming at low Reynolds numbers," *The Journal of the Acoustical Society of America*, vol. 25, no. 5, pp. 932–938, 1953.

[48] C. A. Lane, "Acoustical streaming in the vicinity of a sphere," *The Journal of the Acoustical Society of America*, vol. 27, no. 6, pp. 1082–1086, 1955.

[49] W. P. Raney, J. C. Corelli, and P. J. Westervelt, "Acoustical streaming in the vicinity of a cylinder," *The Journal of the Acoustical Society of America*, vol. 26, no. 6, pp. 1006–1014, 1954.

[50] J. Holtsmark, I. Johnsen, T. Sikkeland, and S. Skavlem, "Boundary layer flow near a cylindrical obstacle in an oscillating, incompressible fluid," *The Journal of the Acoustical Society of America*, vol. 26, no. 1, pp. 26–39, 1954.

[51] R. W. Thrasher and P. J. Westervelt, "Acoustic Streaming in the vicinity of a sphere," *The Journal of the Acoustical Society of America*, vol. 28, no. 4, p. 796, 1956.

[52] W. L. Nyborg, "Acoustic Streaming due to attenuated plane waves," *The Journal of the Acoustical Society of America*, vol. 25, no. 1, pp. 68–75, 1953.

[53] E. Klaseboer, Q. Sun, and D. Y. C. Chan, "Analytical solution for an acoustic boundary layer around an oscillating rigid sphere," *Physics of Fluids*, vol. 32, no. 12, p. 126105, 2020.

[54] T. Baasch, A. A. Doinikov, and J. Dual, "Acoustic Streaming outside and inside a fluid particle undergoing monopole and dipole oscillations," *Physical review. E*, vol. 101, no. 1-1, p. 013108, 2020. Journal Article.

[55] W. L. Nyborg, "Acoustic Streaming near a boundary," *The Journal of the Acoustical Society of America*, vol. 30, no. 4, pp. 329–339, 1958.

[56] N. Riley, "Oscillatory viscous flows. review and extension," *IMA Journal of Applied Mathematics*, vol. 3, no. 4, pp. 419–434, 1967.

[57] N. Riley, "On a sphere oscillating in a viscous fluid," *The Quarterly Journal of Mechanics and Applied Mathematics*, vol. 19, no. 4, pp. 461–472, 1966.

[58] C.-Y. Wang, "The flow field induced by an oscillating sphere," *Journal of Sound and Vibration*, vol. 2, no. 3, pp. 257–269, 1965. PII: 0022460X65901124.

[59] J. T. Stuart, "Double boundary layers in oscillatory viscous flow," *Journal of Fluid Mechanics*, vol. 24, no. 04, p. 673, 1966.

[60] N. Riley, "Acoustic Streaming," *Theoretical and Computational Fluid Dynamics*, vol. 10, no. 1, pp. 349–356, 1998.

[61] N. Riley, "Steady Streaming," *Annual Review of Fluid Mechanics*, vol. 33, no. 1, pp. 43–65, 2001.

[62] J. Lighthill, "Acoustic Streaming," *Journal of Sound and Vibration*, vol. 61, no. 3, pp. 391–418, 1978. PII: 0022460X78903887.

[63] S. A. Elder, "Cavitation microstreaming," *The Journal of the Acoustical Society of America*, vol. 31, no. 1, pp. 54–64, 1959.

[64] B. J. Davidson and N. Riley, "Cavitation microstreaming," *Journal of Sound and Vibration*, vol. 15, no. 2, pp. 217–233, 1971. PII: 0022460X71905360.

[65] M. S. Longuet-Higgins, "Particle drift near an oscillating bubble," *Proceedings of the Royal Society of London. Series A: Mathematical, Physical and Engineering Sciences*, vol. 453, no. 1962, pp. 1551–1568, 1997.

[66] M. S. Longuet-Higgins, "Viscous streaming from an oscillating spherical bubble," *Proceedings of the Royal Society of London. Series A, Containing Papers of a Mathematical and Physical Character*, vol. 454, no. 1970, pp. 725–742, 1998.

[67] C. Pozrikidis, "A study of linearized oscillatory flow past particles by the boundary-integral method," *Journal of Fluid Mechanics*, vol. 202, pp. 17–41, 1989.

[68] E. J. Chang and M. R. Maxey, "Unsteady flow about a sphere at low to moderate Reynolds numbers. Part 1. Oscillatory motion," *Journal of Fluid Mechanics*, vol. 277, pp. 347–379, 1994. PII: S002211209400279X.

[69] R. S. Alassar and H. M. Badr, "Oscillating viscous flow over a sphere," *Computers & Fluids*, vol. 26, no. 7, pp. 661–682, 1997. PII: S0045793097000170.

[70] G. Mishra, S. A. Patel, and R. P. Chhabra, "Pulsatile flow of power-law fluids over a sphere: Momentum and heat transfer characteristics," *Powder Technology*, vol. 360, pp. 789–817, 2020. PII: S0032591019308782.

[71] R. S. Alassar, "Acoustic Streaming on spheres," *International Journal of Non-Linear Mechanics*, vol. 43, no. 9, pp. 892–897, 2008. PII: S0020746208001170.

[72] D. Klotsa, M. R. Swift, R. M. Bowley, and P. J. King, "Interaction of spheres in oscillatory fluid flows," *Physical Review E*, vol. 76, no. 5, 2007.

[73] D. Klotsa, M. R. Swift, R. M. Bowley, and P. J. King, "Chain formation of spheres in oscillatory fluid flows," *Physical Review E*, vol. 79, no. 2, 2009.

[74] J. Jalal, S. Leontini, D. Fabre, and Manasseh R., "Effects of forces induced by Steady Streaming flows on rigid oscillating spheres," *Australasian Fluid Mechanics Conference*, vol. 20, 2016.

[75] D. Fabre, J. Jalal, J. S. Leontini, and R. Manasseh, "Acoustic Streaming and the induced forces between two spheres," *Journal of Fluid Mechanics*, vol. 810, pp. 378–391, 2017. PII: S0022112016007242.

[76] J. Jalal, *Interaction of Spherical Particles Owing to Steady Streaming Induced by Ultrasound*. Phd, Swinburne University of Technology, 2018.

[77] C. W. Kotas, M. Yoda, and P. H. Rogers, "Visualization of Steady Streaming near oscillating spheroids," *Experiments in Fluids*, vol. 42, no. 1, pp. 111–121, 2006. PII: 224.

[78] F. Otto, E. K. Riegler, and G. A. Voth, "Measurements of the Steady Streaming flow around oscillating spheres using three dimensional particle tracking velocimetry," *Physics of Fluids*, vol. 20, no. 9, p. 093304, 2008.

[79] C. B. Baxi and A. Ramachandran, "Effect of vibration on heat transfer from spheres," *Journal of Heat Transfer*, vol. 91, no. 3, pp. 337–343, 1969.

[80] P. S. Larsen and J. W. Jensen, "Evaporation rates of drops in forced convection with superposed transverse sound field," *International Journal of Heat and Mass Transfer*, vol. 21, no. 4, pp. 511–517, 1978. PII: 0017931078900856.

[81] Y. Mori, M. Imabayashi, K. Hijikata, and Y. Yoshida, "Unsteady heat and mass transfer from spheres," *International Journal of Heat and Mass Transfer*, vol. 12, no. 5, pp. 571–585, 1969. PII: 0017931069900398.

[82] A. Gopinath, "Steady Streaming due to small-amplitude torsional oscillations of a sphere in a viscous fluid," *The Quarterly Journal of Mechanics and Applied Mathematics*, vol. 46, no. 3, pp. 501–520, 1993.

[83] A. Gopinath and A. F. Mills, "Convective heat transfer from a sphere due to Acoustic Streaming," *Journal of Heat Transfer*, vol. 115, no. 2, pp. 332–341, 1993.

[84] A. Gopinath, "Steady Streaming due to small-amplitude superimposed oscillations of a sphere in a viscous fluid," *The Quarterly Journal of Mechanics and Applied Mathematics*, vol. 47, no. 3, pp. 461–480, 1994.

[85] N. Kawahara, A. L. Yarin, G. Brenn, O. Kastner, and F. Durst, "Effect of Acoustic Streaming on the mass transfer from a sublimating sphere," *Physics of Fluids*, vol. 12, no. 4, pp. 912–923, 2000.

[86] A. L. Yarin, M. Pfaffenlehner, and C. Tropea, "On the acoustic levitation of droplets," *Journal of Fluid Mechanics*, vol. 356, pp. 65–91, 1998. PII: S0022112097007829.

[87] A.L. Yarin , O. Kastner, D. Rensink, and C. Tropea, "Evaporation of acoustically levitated droplets," *Journal of Fluid Mechanics*, vol. 399, pp. 151–204, 1999.

[88] A. M. Al Taweel and M. I. Ismail, "Comparative analysis of mass transfer at vibrating electrodes," *Journal of Applied Electrochemistry*, vol. 6, no. 6, pp. 559–564, 1976. PII: BF00614544.

[89] A. P. Burdukov and V. E. Nakoryakov, "On mass transfer in an acoustic field," *Journal of Applied Mechanics and Technical Physics*, vol. 6, no. 2, pp. 51–55, 1965. PII: BF00915612.

[90] A. P. Burdukov and V. E. Nakoryakov, "Effects of vibrations on mass transfer from a sphere at high Prandtl numbers," *Journal of Applied Mechanics and Technical Physics*, vol. 8, no. 3, pp. 111–113, 1967. PII: BF00913231.

[91] I. N. Fiklistov and G. A. Aksel'rud, "Kinetics of mass transfer between a bed of solid particles and a pulsating stream of liquid," *Journal of engineering physics*, vol. 10, no. 4, pp. 312–316, 1963. PII: BF00837832.

[92] W. E. Rowe and W. L. Nyborg, "Changes in an electrode process brought about by small–scale Acoustic Streaming," *The Journal of the Acoustical Society of America*, vol. 39, no. 5A, pp. 965–971, 1966.

[93] D. Padamanabha, B. G. Nair, and A. Ramachandran, "Effect of vertical vibration on mass transfer from spheres," *Indian Journal of Technology*, vol. 8, no. 7, pp. 243–247, 1970.

[94] H. Hara and K. Endoh, "The influence of ultrasonics on heat transfer from a single sphere in liquids," *Journal of Chemical Engineering of Japan*, vol. 7, no. 5, pp. 385–386, 1971.

[95] A. M. Boldarev, A. P. Burdukov, V. E. Nakoryakov, and V. I. Sosunov, "Investigation of the effect of ultrasonic vibrations on mass transfer from a sphere, with large Prandtl numbers," *Journal of Applied Mechanics and Technical Physics*, vol. 12, no. 2, pp. 295–297, 1971. PII: BF00850707.

[96] H. Gibert and H. Angelino, "Influence de la pulsation sur les transferts de matière entre une sphère et un liquide," *The Canadian Journal of Chemical Engineering*, vol. 51, no. 3, pp. 319–325, 1973.

[97] N. O. Lemcoff and G. J. Jameson, "Solid—liquid mass transfer in a resonant bubble contactor," *Chemical Engineering Science*, vol. 30, no. 4, pp. 363–367, 1975. PII: 0009250975850019.

[98] M. P. Noordzij and J. W. Rotte, "Mass-transfer coefficients for a simultaneously rotating and translating sphere," *Chemical Engineering Science*, vol. 23, no. 6, pp. 657–660, 1967. PII: 0009250968890104.

[99] C. K. Drummond and F. A. Lyman, "Mass transfer from a sphere in an oscillating flow with zero mean velocity," *Computational Mechanics*, vol. 6, no. 4, pp. 315–326, 1990. PII: BF00370111.

[100] R. S. Alassar, H. M. Badr, and H. A. Mavromatis, "Heat convection from a sphere placed in an oscillating free-stream," *International Journal of Heat and Mass Transfer*, vol. 42, no. 7, pp. 1289–1304, 1999. PII: S0017931098002105.

[101] M. Ohmi and T. Usui, "Theory of mass transfer from a sphere and a circular cylinder in pulsating flow," *Transactions of the Iron and Steel Institute of Japan*, vol. 22, no. 8, pp. 593–599, 1982.

[102] M. Ohmi, T. Usui, Y. Matsumoto, and Y. Masuyama, "Experimental study of mass transfer from a sphere in pulsating flow," *Transactions of the Iron and Steel Institute of Japan*, vol. 22, no. 8, pp. 600–607, 1982.

[103] M. Y. Ha, "A theoretical study on the acoustically driven oscillating flow around small spherical particles," *KSME Journal*, vol. 6, no. 1, pp. 49–57, 1992.

[104] M. Yeong Ha and S. Yavuzkurt, "A theoretical investigation of acoustic enhancement of heat and mass transfer - i. Pure oscillating flow," *International Journal of Heat and Mass Transfer*, vol. 36, no. 8, pp. 2183–2192, 1993. PII: S0017931005801498.

[105] M. Yeong Ha and S. Yavuzkurt, "A theoretical investigation of acoustic enhancement of heat and mass transfer - ii. Oscillating flow with a steady velocity component," *International Journal of Heat and Mass Transfer*, vol. 36, no. 8, pp. 2193–2202, 1993. PII: S0017931005801504.

[106] G. Jiang, W. Xu, Y. Liu, Y. Wu, and Q. Kong, "A numerical study on the oscillating flow induced by an acoustic field around coal particles," *Journal of Combustion*, vol. 2016, pp. 1–13, 2016. PII: 8306839.

[107] G. Jiang, Y. Yang, Y. Liu, and Y. Jiang, "Acoustic Streaming outside spherical particles and parameter analysis of heat transfer enhancement," *European Journal of Mechanics - B/Fluids*, vol. 86, pp. 1–14, 2021. PII: S0997754620306270.

[108] G. Jiang, Y. Yang, W. Xu, M. Yu, and Y.-c. Liu, "Convective heat exchange characteristics of acoustic-induced flows over a sphere: The role of Acoustic Streaming," *Applied Acoustics*, vol. 177, p. 107915, 2021. PII: S0003682X21000086.

[109] H. M. Blackburn, "Mass and momentum transport from a sphere in steady and oscillatory flows," *Physics of Fluids*, vol. 14, no. 11, pp. 3997–4011, 2002.

[110] E. G. Lierke and L. Holitzner, "Positioning of drops, particles and bubbles in ultrasonic standing-waves levitators. A final round up," *Acta Acustica united with Acustica*, vol. 99, no. 2, pp. 302–316, 2013.

[111] E. G. Lierke, "Vergleichende Betrachtungen zur berührungslosen Positionierung von Einzeltropfen in aerodynamischen, akustischen und elektrischen Kraftfeldern," *Forschung im Ingenieurwesen*, vol. 61, no. 7-8, pp. 201–216, 1995. PII: BF02609485.

[112] S. S. Sadhal, "Acoustofluidics 15: Streaming with sound waves interacting with solid particles," *Lab on a chip*, vol. 12, no. 15, pp. 2600–2611, 2012. Journal Article.

[113] J. L. Guinon, V. Perez-Herranz, J. Garca-Anton, and G. Lacoste, "Enhancement of mass transfer at a spherical electrode in pulsating flow," *Journal of Applied Electrochemistry*, vol. 25, no. 3, 1995.

[114] J. J. Carvalho, "Behavior of solid particles in pulsating flows," *Journal of Sound and Vibration*, vol. 185, no. 4, pp. 581–593, 1995. PII: S0022460X85704026.

[115] J. H. Krasuk and J. M. Smith, "Mass transfer in a pulsed column," *Chemical Engineering Science*, vol. 18, no. 9, pp. 591–598, 1963. PII: 0009250963850289.

[116] J. H. Krasuk and J. M. Smith, "Mass transfer in a packed, pulsed column," *AIChE Journal*, vol. 10, no. 5, pp. 759–763, 1964.

[117] X. D. Liu, C. W. Cao, and Z. H. Lang, "Heat transfer between materials and unsteady airflow from a Helmholtz-type combustor," *Drying Technology*, vol. 19, no. 8, pp. 1939–1948, 2001.

[118] A. Teiwes, M. Dosta, M. Jacob, and S. Heinrich, "Pulsed multiphase flows - numerical investigation of particle dynamics in pulsating gas - solid flows at elevated temperatures," *Processes*, vol. 8, no. 7, p. 815, 2020. PII: pr8070815.

[119] B. Dahm, *Ein Beitrag zum instationären Wärmeübergang auf Teilchen im Hinblick auf eine verfahrenstechnische Optimierung des Schmidtrohres*. Phd-thesis, Hochschule für Architektur und Bauwesen Weimar, 1975.

[120] E. Cunningham, "On the velocity of steady fall of spherical particles through fluid medium," *Proceedings of the Royal Society of London. Series A, Containing Papers of a Mathematical and Physical Character*, vol. 83, no. 563, pp. 357–365, 1910.

[121] M. Knudsen and S. Weber, "Luftwiderstand gegen die langsame Bewegung kleiner Kugeln," *Annalen der Physik*, vol. 341, no. 15, pp. 981–994, 1911.

[122] R. A. Millikan, "The isolation of an ion, a precision measurement of its charge, and the correction of Stokes's law," *Physical Review (Series I)*, vol. 32, no. 4, pp. 349–397, 1911.

[123] R. A. Millikan, "Coefficients of slip in gases and the law of reflection of molecules from the surfaces of solids and liquids," *Physical Review*, vol. 21, no. 3, pp. 217–238, 1923.

[124] M. D. Allen and O. G. Raabe, "Re-evaluation of Millikan's oil drop data for the motion of small particles in air," *J. Aerosol Sci.*, vol. 13, no. 6, pp. 537–547, 1982. PII: 0021850282900192.

[125] M. D. Allen and O. G. Raabe, "Slip correction measurements of spherical solid aerosol particles in an improved Millikan apparatus," *Aerosol Science and Technology*, vol. 4, no. 3, pp. 269–286, 1985.

[126] D. J. Rader, "Momentum slip correction factor for small particles in nine common gases," *Journal of Aerosol Science*, vol. 21, no. 2, pp. 161–168, 1990.

[127] R. A. Millikan, "The general law of fall of a small spherical body through a gas, and its bearing upon the nature of molecular reflection from surfaces," *Physical Review*, vol. 22, no. 1, pp. 1–23, 1923.

[128] D. K. Hutchins, M. H. Harper, and R. L. Felder, "Slip correction measurements for solid spherical particles by modulated dynamic light scattering," *Aerosol Science and Technology*, vol. 22, no. 2, pp. 202–218, 1995.

[129] J. H. Kim, G. W. Mulholland, S. R. Kukuck, and D. Y. H. Pui, "Slip correction measurements of certified PSL nanoparticles using a nanometer differential mobility analyzer (nano-DMA) for Knudsen number from 0.5 to 83," *Journal of research of the National Institute of Standards and Technology*, vol. 110, no. 1, pp. 31–54, 2005. Journal Article.

[130] R. W. Barber, "Numerical simulation of low reynolds number slip flow past a confined microsphere," *AIP Conference Proceedings*, vol. 663, no. 1, pp. 808–815, 2003.

[131] A. Moshfegh, M. Shams, G. Ahmadi, and R. Ebrahimi, "A novel surface-slip correction for microparticles motion," *Colloids and Surfaces A: Physicochemical and Engineering Aspects*, vol. 345, no. 1-3, pp. 112–120, 2009. PII: S092777570900260X.

[132] M. Smoluchowski von Smolan, "Über Wärmeleitung in verdünnten Gasen," *Annalen der Physik*, vol. 300, no. 1, pp. 101–130, 1898.

[133] B. Mohajer, V. Aliakbar, M. Shams, and A. Moshfegh, "Heat transfer analysis of a microspherical particle in the slip flow regime by considering variable properties," *Heat Transfer Engineering*, vol. 36, no. 6, pp. 596–610, 2015.

[134] Z. Liu, J. Zhou, and H. Wu, "Non-isothermal slip flow over micro spherical particle at low reynolds numbers," *Chemical Engineering Science*, vol. 191, pp. 19–30, 2018. PII: S0009250918304093.

[135] M. Anbarsooz and H. Niazmand, "Heat transfer characteristics of slip flow over solid spheres," *Proceedings of the school of Mechanical Engineers, Part C: Journal of Mechanical Engineering Science*, vol. 230, no. 19, pp. 3431–3441, 2016.

[136] Y. Ben-Ami and A. Manela, "The sound of a pulsating sphere in a rarefied gas: Continuum breakdown at short length and time scales," *Journal of Fluid Mechanics*, vol. 871, pp. 668–693, 2019. PII: S002211201900329X.

[137] Y. W. Yap and J. E. Sader, "Sphere oscillating in a rarefied gas," *Journal of Fluid Mechanics*, vol. 794, pp. 109–153, 2016. PII: S0022112016001439.

[138] J. Horwitz and A. Mani, "Accurate calculation of stokes drag for point–particle tracking in two-way coupled flows," *Journal of Computational Physics*, vol. 318, pp. 85–109, 2016. PII: S0021999116300808.

[139] J. Horwitz and A. Mani, "Correction scheme for point-particle models applied to a nonlinear drag law in simulations of particle-fluid interaction," *International Journal of Multiphase Flow*, vol. 101, pp. 74–84, 2018.

[140] Bruce E. Poling, John M. Prausnitz, and John P. O'Connell, *Properties of Gases and Liquids, Fifth Edition*. McGraw-Hill Education, 2001.

[141] R. Müller, "Die Annäherung der Temperaturabhängigkeit der Transportkoeffizienten von Gasen durch einen Potenzansatz," *Chemie Ingenieur Technik*, vol. 40, no. 7, pp. 344–349, 1968.

[142] L. E. Kinsler, A. R. Frey, A. B. Coppens, and J. V. Sanders, *Fundamentals of acoustics*. John Wiley & Sons, 2000.

[143] L. Shemer, I. Wygnanski, and E. Kit, "Pulsating flow in a pipe," *Journal of Fluid Mechanics*, vol. 153, no. -1, pp. 313–337, 1985.

[144] T. Sexl, "Über den von E. G. Richardson entdeckten Annulareffekt," *Zeitschrift für Physik*, vol. 61, no. 5-6, pp. 349–362, 1930. PII: BF01340631.

[145] J. R. Womersley, "Method for the calculation of velocity, rate of flow and viscous drag in arteries when the pressure gradient is known," *The Journal of Physiology*, vol. 127, no. 3, pp. 553–563, 1955.

[146] S. Uchida, "The pulsating viscous flow superposed on the steady laminar motion of incompressible fluid in a circular pipe," *Zeitschrift für angewandte Mathematik und Physik ZAMP*, vol. 7, no. 5, pp. 403–422, 1956. PII: BF01606327.

[147] A. Hussain and W. C. Reynolds, "The mechanics of an organized wave in turbulent shear flow," *Journal of Fluid Mechanics*, vol. 41, no. 2, pp. 241–258, 1970. PII: S0022112070000605.

[148] E. G. Richardson and E. Tyler, "The transverse velocity gradient near the mouths of pipes in which an alternating or continuous flow of air is established," *Proceedings of the Physical Society*, vol. 42, no. 1, pp. 1–15, 1929.

[149] D. Shmilovitz, "On the definition of total harmonic distortion and its effect on measurement interpretation," *IEEE Transactions on Power Delivery*, vol. 20, no. 1, pp. 526–528, 2005.

[150] A. Guha, "Transport and deposition of particles in turbulent and laminar flow," *Annual Review of Fluid Mechanics*, vol. 40, no. 1, pp. 311–341, 2008.

[151] G. Rudinger, *Fundamentals of Gas Particle Flow*. Elsevier, 2012.

[152] P. G. Saffman, "The lift on a small sphere in a slow shear flow," *Journal of Fluid Mechanics*, vol. 22, no. 2, pp. 385–400, 1965. PII: S0022112065000824.

[153] A. Guha, "A unified Eulerian theory of turbulent deposition to smooth and rough surfaces," *J. Aerosol Sci.*, vol. 28, no. 8, pp. 1517–1537, 1997. PII: S0021850297000281.

[154] L. Talbot, R. K. Cheng, R. W. Schefer, and D. R. Willis, "Thermophoresis of particles in a heated boundary layer," *Journal of Fluid Mechanics*, vol. 101, no. 4, pp. 737–758, 1980. PII: S0022112080001905.

[155] A. Melling, "Tracer particles and seeding for particle image velocimetry," *Measurement Science and Technology*, vol. 8, no. 12, pp. 1406–1416, 1997. PII: S0957-0233(97)84480-3.

[156] G. G. Stokes, "On the effect of the internal friction of fluids on the motion of pendulums," in *Mathematical and Physical Papers* (G. G. Stokes, ed.), pp. 1–10, Cambridge university press, 2009.

[157] S. Sazhin, T. Shakked, V. Sobolev, and D. Katoshevski, "Particle grouping in oscillating flows," *European Journal of Mechanics - B/Fluids*, vol. 27, no. 2, pp. 131–149, 2008. PII: S0997754607000453.

[158] R. P. Dring, "Sizing criteria for laser anemometry particles," *Journal of Fluids Engineering*, vol. 104, no. 1, pp. 15–17, 1982.

[159] M. C. Ruzicka, "On dimensionless numbers," *Chemical Engineering Research and Design*, vol. 86, no. 8, pp. 835–868, 2008. PII: S0263876208000725.

[160] S. Heidinger, S. Unz, and M. Beckmann, "Simple particle relaxation modeling in one-dimensional oscillating flows," *Processes*, vol. 10, no. 7, p. 1322, 2022. PII: pr10071322.

[161] C.-Y. Wang, "On high-frequency oscillatory viscous flows," *Journal of Fluid Mechanics*, vol. 32, no. 1, pp. 55–68, 1968. PII: S0022112068000583.

[162] K. Chong, S. D. Kelly, S. Smith, and J. D. Eldredge, "Inertial particle trapping in viscous streaming," *Physics of Fluids*, vol. 25, no. 3, p. 033602, 2013.

[163] R. Clift, J. R. Grace, and M. E. Weber, *Bubbles, drops, and particles*. Dover Publ., 2013.

[164] L. Schiller and A. Naumann, "Drag coefficient corellation," *VDI Zeitung*, 1935.

[165] P. N. Rowe *et al.*, "The drag coefficient of a sphere," *Trans. Inst. Chem. Eng*, vol. 39, pp. 175–181, 1961.

[166] X. Guan, X. Li, N. Yang, and M. Liu, "CFD simulation of gas-liquid flow in stirred tanks: Effect of drag models," *Chemical Engineering Journal*, vol. 386, p. 121554, 2020.

[167] N. Ellendt, A. M. Lumanglas, S. I. Moqadam, and L. Mädler, "A model for the drag and heat transfer of spheres in the laminar regime at high temperature differences," *International Journal of Thermal Sciences*, vol. 133, pp. 98–105, 2018.

[168] E. E. Michaelides, "On the drag coefficient and the correct integration of the equation of motion of particles in gases," *Journal of Fluids Engineering*, vol. 110, no. 3, pp. 339–341, 1988.

[169] S. Temkin and C.-M. Leung, "On the velocity of a rigid sphere in a sound wave," *Journal of Sound and Vibration*, vol. 49, no. 1, pp. 75–92, 1976. PII: 0022460X76907586.

[170] W. C. Hinds, *Aerosol Technology*. Wiley, 2nd ed. ed., 1999.

[171] P. D. Richardson, "Heat transfer from a circular cylinder by Acoustic Streaming," *Journal of Fluid Mechanics*, vol. 30, no. 2, pp. 337–355, 1967. PII: S0022112067001466.

[172] H. Schlichting and K. Gersten, *Boundary-Layer Theory*. Springer Berlin Heidelberg, 2017.

[173] W. R. Goossens, "Review of the empirical correlations for the drag coefficient of rigid spheres," *Powder Technology*, vol. 352, pp. 350–359, 2019. PII: S0032591019303237.

[174] S. Heidinger, S. Unz, and M. Beckmann, "Heat and mass transfer to particles in one-dimensional oscillating flows," *Processes*, vol. 11, no. 1, p. 173, 2023. PII: pr11010173.

[175] J. M. Valverde, "Acoustic Streaming in gas-fluidized beds of small particles," *Soft Matter*, vol. 9, no. 37, p. 8792, 2013.

[176] S. Yavuzkurt and M. Y. Ha, "A model of the enhancement of combustion of coal-water slurry fuels using high-intensity acoustic fields," *Journal of Energy Resources Technology*, vol. 113, no. 4, pp. 268–276, 1991.

[177] A.-N. Spiess and N. Neumeyer, "An evaluation of R2 as an inadequate measure for nonlinear models in pharmacological and biochemical research: A Monte Carlo approach," *BMC Pharmacology*, vol. 10, no. 1, p. 6, 2010. Journal Article Research Support, Non-U.S. Gov't.

[178] W. E. Ranz and W. R. Marshall, "Vaporation from drops, part i," *Chem. Eng. Progr.*, vol. 48, pp. 141–146, 1952.

[179] N. T. Hsu, K. Sato, and B. H. Sage, "Material transfer in turbulent gas streams," *Industrial & Engineering Chemistry*, vol. 46, no. 5, pp. 870–876, 1954.

[180] S. Whitaker, "Forced convection heat transfer correlations for flow in pipes, past flat plates, single cylinders, single spheres, and for flow in packed beds and tube bundles," *AIChE Journal*, vol. 18, no. 2, pp. 361–371, 1972.

[181] V. Gnielinski, "Berechnung mittlerer Wärme- und Stoffübergangskoeffizienten an laminar und turbulent überströmten Einzelkörpern mit Hilfe einer einheitlichen Gleichung," *Forschung im Ingenieurwesen*, vol. 41, no. 5, pp. 145–153, 1975. PII: BF02560793.

[182] C. Ke, S. Shu, H. Zhang, H. Yuan, and D. Yang, "On the drag coefficient and averaged nusselt number of an ellipsoidal particle in a fluid," *Powder Technology*, vol. 325, pp. 134–144, 2018. PII: S0032591017308446.

[183] A. Richter and P. A. Nikrityuk, "Drag forces and heat transfer coefficients for spherical, cuboidal and ellipsoidal particles in cross flow at sub-critical reynolds numbers," *Int. J. Heat Mass Transfer*, vol. 55, no. 4, pp. 1343–1354, 2012. PII: S0017931011005023.

[184] N. N. Sayegh and W. H. Gauvin, "Numerical analysis of variable property heat transfer to a single sphere in high temperature surroundings," *AIChE Journal*, vol. 25, no. 3, pp. 522–534, 1979.

[185] B. Melissari and S. A. Argyropoulos, "Development of a heat transfer dimensionless correlation for spheres immersed in a wide range of Prandtl number fluids," *International Journal of Heat and Mass Transfer*, vol. 48, no. 21-22, pp. 4333–4341, 2005.

[186] L. C. Witte, "An experimental study of forced-convection heat transfer from a sphere to liquid sodium," *Journal of Heat Transfer*, vol. 90, no. 1, pp. 9–12, 1968.

[187] P. Chuchottaworn, A. Fujinami, and K. Asano, "Experimental study of evaporation of a volatile pendant drop under high mass flux conditions," *Journal of Chemical Engineering of Japan*, vol. 17, no. 1, pp. 7–13, 1984.

[188] P. Bagchi, M. Y. Ha, and S. Balachandar, "Direct numerical simulation of flow and heat transfer from a sphere in a uniform cross-flow," *Journal of Fluids Engineering*, vol. 123, no. 2, pp. 347–358, 2001.

[189] A. Acrivos and T. D. Taylor, "Heat and mass transfer from single spheres in stokes flow," *Physics of Fluids*, vol. 5, no. 4, p. 387, 1962.

[190] A. M. Al Taweel and J. Landau, "Mass transfer between solid spheres and oscillating fluids - a critical review," *The Canadian Journal of Chemical Engineering*, vol. 54, no. 6, pp. 532–539, 1976.

[191] M. Y. Ha, S. Yavuzkurt, and K. C. Kim, "Heat transfer past particles entrained in an oscillating flow with and without a steady velocity," *Int. J. Heat Mass Transfer*, vol. 36, no. 4, pp. 949–959, 1993. PII: S0017931005802790.

[192] W. Xu, G. Jiang, L. An, and Y. Liu, "Numerical and experimental study of acoustically enhanced heat transfer from a single particle in flue gas," *Combust. Sci. Technol.*, vol. 190, no. 7, pp. 1158–1177, 2018.

[193] G. Dharmadurai, "Analysis of photoacoustically investigated gaseous heat transfer between solid surfaces," *Phys. Stat. Sol. A*, vol. 83, pp. K27–K30, 1984.

[194] S. Song and M. Yovanovich, *Correlation of thermal accommodation coefficient for engineering surfaces*. University of Waterloo, 1987.

[195] J. E. Dec, J. O. Keller, and I. Hongo, "Time-resolved velocities and turbulence in the oscillating flow of a pulse combustor tail pipe," *Combust. Flame*, vol. 83, no. 3-4, pp. 271–292, 1991. PII: 001021809190075M.

[196] W. A. Sirignano, *Fluid dynamics and transport of droplets and sprays*. Cambridge university press, 2nd ed. ed., 2010.

[197] M. T. Landahl and E. Mollo-Christensen, *Turbulence and random processes in fluid mechanics*. Cambridge university press, 2nd ed. ed., 1992.

[198] R. Courant, K. Friedrichs, and H. Lewy, "Über die partiellen Differenzengleichungen der mathematischen physik," *Mathematische Annalen*, vol. 100, no. 1, pp. 32–74, 1928. PII: BF01448839.

[199] The MathWorks Inc., "Matlab," 2022.

[200] Kitware Inc., "Paraview," 2022.

[201] I. E. Commission, "Electroacoustics—sound level meters — Part 1: Specifications (IEC 61672-1)," *Geneva, Switzerland*, 2013.

[202] N. P. Bansal and R. H. Doremus, *Handbook of glass properties*. Academic Press handbook series, Academic Press, 1986.

[203] S. Zakel, E. Brandes, and V. Schröder, "Reliable safety characteristics of flammable gases and liquids - the database CHEMSAFE," *Journal of Loss Prevention in the Process Industries*, vol. 62, p. 103914, 2019. PII: S0950423019300415.

APPENDIX A

Derivation and Solution of Particle Motion in the Stokes Model

The basis for deriving a motion equation for particles in a pulsating flow is the constantly existing equilibrium between the drag force F_D and the inertial force F_I. The inertial force in its general form

$$F_I = m \cdot a \tag{A.1}$$

is expressed by acceleration a and mass m. In this case, the shape of the particle is assumed to be spherical, which leads to an equation where the mass is

$$m = \rho_p \cdot V = \rho_p \frac{\pi}{6} d^3 \tag{A.2}$$

with the density of the particle ρ_p, the volume of the particle V, and the diameter of the particle d. This leaves the inertial force of a particle to be

$$F_I = \rho_p \frac{\pi}{6} d^3 a \tag{A.3}$$

The drag force, acting on the particle, can be expressed by the general form of Newton's resistance law

$$F_D = C_D \frac{\pi}{8} \rho_f d^2 u^2 \tag{A.4}$$

, where ρ_f is the density of the surrounding fluid, C_D is the drag coefficient, and u is the relative velocity between the particle and the fluid, which can be expressed with the

velocities of particle u_p and fluid u_f:

$$u = u_f - u_p \tag{A.5}$$

The fluid velocity is considered utilizing the wave form

$$\bar{u}_f + U_f \cos(\omega t + \phi_0) \tag{A.6}$$

with the mean fluid velocity $\bar{u}_f$, the amplitude of the fluid velocity U_f, and the angular frequency $\omega = 2\pi f$. The equilibrium between drag force and inertia is

$$F_D = F_I \tag{A.7}$$

$$C_D \frac{\pi}{8} \rho_f d^2 u^2 = \rho_p \frac{\pi}{6} d^3 a \tag{A.8}$$

$$a = \frac{3}{4} C_D \frac{\rho_f}{\rho_p} \frac{u^2}{d} \tag{A.9}$$

Various drag models, valid for different Reynolds number ranges, can be applied to this law by forms of the drag coefficient C_D. Here, Stokes is applied

$$C_{D,S} = \frac{24}{Re} \tag{A.10}$$

Inserting A.10 into A.9 leads to

$$a = \frac{18\eta}{\rho_p d^2} u \tag{A.11}$$

The acceleration a can also be denoted as $\dot{u}_p$ since it is the derivation of the particle velocity in respect to time. All the factors in the fraction of A.11 are not dependent on the motion and can be combined and expressed by the relaxation time τ:

$$\tau = \frac{\rho_p d^2}{18\eta} \tag{A.12}$$

Finally, using equations A.5 and A.6 leads to a form of the relation where the character of a homogeneous linear differential equation with constant coefficients becomes obvious:

$$\dot{u}_p + \frac{1}{\tau} u_p = \frac{1}{\tau} \left[\bar{u}_f + U_f \cos\left(\omega t + \phi_0\right) \right] \tag{A.13}$$

This ODE is solved by superimposing the solution of the homogeneous form

$$\dot{u}_p + \frac{1}{\tau} u_p = 0 \tag{A.14}$$

and the particular solution. The homogeneous solution to equation A.13 is found by using the ansatz $u_p = ce^{\lambda t}$, leading to the characteristic equation

$$\lambda + \frac{1}{\tau} = 0 \tag{A.15}$$

Solving this equation and inserting λ into the ansatz delivers the homogeneous solution

$$u_p = ce^{-\frac{t}{\tau}} \tag{A.16}$$

with a constant c, which is determined later by an initial condition. The particular solution to the ODE A.13 is found with the coefficient comparison approach. Each term in the perturbation function is accounted for with a similar term including undetermined coefficients A-C:

$$\bar{u}_f \mathrel{\hat{=}} A \tag{A.17}$$

$$U_f \cos\left(\omega t + \phi_0\right) \mathrel{\hat{=}} \tau B \sin\left(\omega t + \phi_0\right) + \tau C \cos\left(\omega t + \phi_0\right) \tag{A.18}$$

The superposition of these terms leads to an undetermined form of the solution:

$$u_p = A + B\cos(\omega t + \phi_0) + C\sin(\omega t + \phi_0) \tag{A.19}$$

$$\dot{u_p} = -\omega B\sin(\omega t + \phi_0) + \omega C\cos(\omega t + \phi_0) \tag{A.20}$$

These equations can be reinserted in the original ODE A.13:

$$\begin{aligned} &-\omega\tau B\sin(\omega t + \phi_0) + \omega\tau C\cos(\omega t + \phi_0) \\ &+ A + B\cos(\omega t + \phi_0) + C\sin(\omega t + \phi_0) \\ &= \bar{u}_f + U_f\cos(\omega t + \phi_0) \end{aligned} \tag{A.21}$$

Now the coefficients of each term can be compared with their counterparts from the perturbation function to determine A, B, and C:

$$A = \bar{u}_f \tag{A.22}$$

$$-\omega\tau B\sin(\omega t + \phi_0) + C\sin(\omega t + \phi_0) = 0 \tag{A.23}$$

$$\omega\tau C\cos(\omega t + \phi_0) + B\cos(\omega t + \phi_0) = U_f\cos(\omega t + \phi_0) \tag{A.24}$$

This linear system of equations can be solved to:

$$A = \bar{u}_f \tag{A.25}$$

$$B = \frac{U_f}{1 + (\omega\tau)^2} \tag{A.26}$$

$$C = U_f\frac{\omega\tau}{1 + (\omega\tau)^2} \tag{A.27}$$

After reinserting expression A.25 - A.27 into equation A.19 and substituting the oscillation Stokes number $Stk = \omega\tau$, the particular solution to the ODE is

$$u_p = \bar{u} + \frac{U_f}{1 + Stk^2} \left[\sin(\omega t + \phi_0) - Stk \cos(\omega t + \phi_0)\right] \tag{A.28}$$

Superimposing the homogeneous and the particular solution leads to

$$u_p = ce^{-\frac{t}{\tau}} + \bar{u}_f + \frac{U_f}{1 + Stk^2} \left[\sin(\omega t + \phi_0) - Stk \cos(\omega t + \phi_0)\right] \tag{A.29}$$

Applying the initial condition of the particle having a certain velocity u_0 at $t = 0$, c can be determined to

$$u_p(t = 0) = u_0 = \quad c + \bar{u}_f + \frac{U_f}{1 + Stk^2} \left[\cos(\phi_0) + Stk \sin(\phi_0)\right] \tag{A.30}$$

$$c = u_0 - \bar{u}_f - \frac{U_f}{1 + Stk^2} \left[\cos(\phi_0) + Stk \sin(\phi_0)\right] \tag{A.31}$$

Inserting A.31 into A.29 leads to the final solution of the ODE. This motion equation can be arranged into a transient and a resident part:

$$u_p(t) = \underbrace{\left[u_0 - \bar{u}_f - \frac{U_f}{1 + Stk^2} \left[\cos(\phi_0) + Stk \sin(\phi_0)\right]\right] e^{-\frac{t}{\tau}}}_{\text{transient}} + \underbrace{\bar{u}_f + \frac{U_f}{1 + Stk^2} \left[\cos(\omega t + \phi_0) + Stk \sin(\omega t + \phi_0)\right]}_{\text{resident}} \tag{A.32}$$

and the slip velocity can be calculated with

$$\begin{aligned} u(t) &= u_f(t) - u_p(t) \\ &= \underbrace{\left[\bar{u}_f - u_0 + \frac{U_f}{1+Stk^2}\left[\cos(\phi_0) + Stk\sin(\phi_0)\right]\right] e^{-\frac{t}{\tau}}}_{\text{transient}} \\ &+ \underbrace{U_f \frac{Stk}{1+Stk^2}\left[Stk\cos\left(\omega t + \phi_0\right) - \sin\left(\omega t + \phi_0\right)\right]}_{\text{resident}} \end{aligned} \tag{A.33}$$

APPENDIX B

Derivation and Solution of Particle Motion in the Landau & Lifshitz Model

A similar procedure as in Appendix A is applied for deriving the slip velocity amplitude calculated with the drag model by Landau & Lifshitz. As in Equation A.11, the point of origin is the constant equilibrium of the drag force and the inertia of the particle:

$$F_D = F_I \tag{B.1}$$

$$3\pi\eta d\left(1+\frac{d}{2\delta}\right)u + \frac{3}{4}\pi d^2\sqrt{\frac{2\eta\rho}{\omega}}\left(1+\frac{d}{9\delta}\right)\frac{du}{dt} = \rho_p\frac{\pi}{6}d^3a \tag{B.2}$$

Utilizing Relation A.5 and rearranging leads to the normal form of the differential equation:

$$\begin{aligned}\dot{u}_p + &\left[\frac{18\eta\left(1+\frac{d}{2\delta}\right)}{9d\sqrt{\frac{\eta\rho_f}{2\omega}}\left(1+\frac{d}{9\delta}\right)+\rho_p d^2}\right]u_p \\ &= \left[\frac{18\eta\left(1+\frac{d}{2\delta}\right)}{9d\sqrt{\frac{\eta\rho_f}{2\omega}}\left(1+\frac{d}{9\delta}\right)+\rho_p d^2}\right]U_f\cos(\omega t) \\ &- \left[\frac{9d\sqrt{\frac{\eta\rho_f}{2\omega}}\left(1+\frac{d}{9\delta}\right)}{9d\sqrt{\frac{\eta\rho_f}{2\omega}}\left(1+\frac{d}{9\delta}\right)+\rho_p d^2}\right]\omega U_f\sin(\omega t)\end{aligned} \tag{B.3}$$

Three coefficients are introduced for the sake of readability and convenience:

$$a = 18\eta \left(1 + \frac{d}{2\delta}\right) \tag{B.4}$$

$$b = 9d\sqrt{\frac{\eta\rho_f}{2\omega}} \left(1 + \frac{d}{9\delta}\right) \tag{B.5}$$

$$c = \rho_p d^2 \tag{B.6}$$

With these parameters, Equation B.3 simplifies to

$$\dot{u}_p + \frac{a}{b+c}u_p = \frac{a}{b+c}U_f \cos(\omega t) - \frac{b}{b+c}\omega U_f \sin(\omega t) \tag{B.7}$$

The general solution of this ODE relates to the constant part of the particle motion as well as the non-harmonic, transient part of the particle motion which quickly decays. Both of these parts of the solution are neglected here in order to focus on the homogeneous part, which delivers the desired amplitude of the slip velocity. Similar to solving the motion of the particle described with the Stokes drag law, a coefficient comparison approach is applied.

The ansatz,

$$u_p = A\sin(\omega t) + B\cos(\omega t) \tag{B.8}$$

$$\dot{u}_p = \omega A\cos(\omega t) - \omega B\cos(\omega t) \tag{B.9}$$

which matches the perturbation function, is inserted into the ODE:

$$\omega A\cos(\omega t) - \omega B\sin(\omega t) + \frac{a}{b+c}A\sin(\omega t) + \frac{a}{b+c}B\cos(\omega t) \tag{B.10}$$

$$= \frac{a}{b+c}U_f\cos(\omega t) - \frac{b}{b+c}\omega U_f \sin(\omega t) \tag{B.11}$$

This equation can be split into two independent equations:

$$\omega B \sin(\omega t) - \frac{a}{b+c} A \sin(\omega t) = \frac{b}{b+c} \omega U_f \sin(\omega t) \tag{B.12}$$

$$\omega A \cos(\omega t) + \frac{a}{b+c} B \cos(\omega t) = \frac{a}{b+c} U_f \cos(\omega t) \tag{B.13}$$

From this, the coefficients A and B can be determined to

$$A = U_f \frac{ac\omega}{a^2 + \omega^2 (b+c)^2} \tag{B.14}$$

$$B = U_f \frac{a^2 + \omega^2 b(b+c)}{a^2 + \omega^2 (b+c)^2} \tag{B.15}$$

Reinserting in Ansatz B.8 and rearranging it gives the resident solution to the original ODE B.3:

$$u_p = \frac{U_f}{a^2 + \omega^2 (b+c)^2} \left[ac\omega \sin(\omega t) + \left(a^2 + \omega^2 b(b+c) \right) \cos(\omega t) \right] \tag{B.16}$$

The slip velocity is derived by using Relation A.5 and A.6, while the extreme value is discovered by detecting zeros in the first differential and an expression for the desired amplitude of the slip velocity is found:

$$\frac{U_{LL}}{U_f} = \frac{1}{\sqrt{\left(\frac{a}{\omega c}\right)^2 + \left(\frac{b}{c} + 1\right)^2}} \tag{B.17}$$

with the Coefficients B.4-B.6. The Solution B.17 can be expressed in terms of the previously introduced oscillating Stokes number $Stk = \omega\tau = \omega \rho_p d^2 / 18\eta$ and the density ratio $\gamma = \rho_p / \rho_f$:

$$\frac{U_{LL}}{U_f} = \frac{1}{\sqrt{\left(\frac{3}{\sqrt{2\gamma Stk}} + \frac{1}{Stk}\right)^2 + \left(\frac{3}{2\sqrt{\gamma Stk}} + \frac{1}{\sqrt{2}\gamma} + 1\right)^2}} \tag{B.18}$$

APPENDIX C

Derivation of Deviation between Stokes and Schiller & Naumann

Considering a spherical rigid particle and starting from the basic equilibrium between the drag force $F_D = C_D \frac{\pi}{2} \rho_f d^2 u^2$ and the inertial force $F_I = \rho_p \frac{4\pi}{3} d^3 a_p$ for Stokes (index S) and Schiller & Naumann (index SN):

$$C_{D,S} \frac{\pi}{2} \rho_f d^2 u_{slip,S}^2 = \rho_p \frac{4\pi}{3} d^3 a_{p,S} \tag{C.1}$$

$$C_{D,SN} \frac{\pi}{2} \rho_f d^2 u_{slip,SN}^2 = \rho_p \frac{4\pi}{3} d^3 a_{p,SN} \tag{C.2}$$

Dividing C.1 by C.2 and rearranging leads to

$$\frac{u_{SN}^2(t)}{u_S^2(t)} = \frac{C_{D,S}(t)}{C_{D,SN}(t)} \frac{a_{p,SN}(t)}{a_{p,S}(t)} \tag{C.3}$$

For harmonic relations, the following statements with particle acceleration a_p and particle velocity u_p hold true:

$$a_p(t) = \dot{u}_p(t) \tag{C.4}$$

$$U_p = \omega A_p \tag{C.5}$$

Here, U_p and A_p denote the particle velocity amplitude and the particle acceleration amplitude, respectively. $\dot{u}_p$ is the particle velocity derivation in respect to time. The most interesting property is the maximum value of the slip velocity, hence the amplitude of the oscillation U. Relation C.3 also holds true for the maximum values and inserting

C.5 leads to

$$\frac{U_{SN}^2}{U_S^2} = \frac{C_{D,S}}{C_{D,SN}} \frac{U_{p,SN}}{U_{p,S}} \tag{C.6}$$

C_D is the maximum value of the drag coefficient when the slip velocity amplitude U is reached with the maximum Reynolds number

$$Re = \frac{Ud}{\nu} \tag{C.7}$$

Using the relations $U_S = Stk\ U_{p,S} = \tau\ A_{p,S}$ gives the expression

$$\frac{U_{SN}}{U_S} = Stk \frac{C_{D,S}}{C_{D,SN}} \frac{U_{p,SN}}{U_{SN}} \tag{C.8}$$

When the Pythagorean theorem,

$$U_f^2 = U^2 + U_p^2 \tag{C.9}$$

is applied, which can be derived from Figure 4.7, Equation C.8 can be further simplified:

$$\frac{U_{SN}}{U_S} = Stk \frac{C_{D,S}}{C_{D,SN}} \sqrt{\left(\frac{U_f}{U_{SN}}\right)^2 - 1} \tag{C.10}$$

In order to set the slip velocity amplitude in relation to the fluid velocity amplitude, each side of Equation C.10 can be multiplied with the right side of Equation 4.15:

$$\frac{U_{SN}}{U_f} = \frac{Stk}{\sqrt{1 + \frac{1}{Stk^2}}} \frac{C_{D,S}}{C_{D,SN}} \sqrt{\left(\frac{U_f}{U_{SN}}\right)^2 - 1} \tag{C.11}$$

Inserting the drag coefficients $C_{D,S} = 24/Re$ and $C_{D,SN} = (24/Re)SN$ with extreme values, respectively, leads to:

$$\frac{U_{SN}}{U_f} = \frac{1}{\sqrt{1 + \frac{SN^2}{Stk^2}}} \tag{C.12}$$

$$\frac{U_{SN}}{U_S} = \sqrt{\frac{Stk^2 + 1}{Stk^2 + SN^2}} \tag{C.13}$$

Since only now the different drag coefficients $C_{D,i}$ are inserted, Equation C.11 can also be used in order to calculate the deviation between the Stokes drag model and any other drag model, which follows Newton's drag formulation and can be expressed by a drag coefficient. Equations C.12 and C.13 are used to calculate the relative deviation between Stokes and Schiller & Naumann:

$$\frac{U_S - U_{SN}}{U_S} = 1 - \sqrt{\frac{Stk^2 + 1}{Stk^2 + SN^2}} \tag{C.14}$$

$$\frac{U_S - U_{SN}}{U_f} = \frac{1}{\sqrt{1 + \frac{1}{Stk^2}}} - \frac{1}{\sqrt{1 + \frac{SN^2}{Stk^2}}} \tag{C.15}$$

APPENDIX D

Parameters and Algorithm of the Direct Numerical Simulation and Flow Pattern Visualisation

The flow patterns in the vicinity of the particle are the result of direct numerical simulations (DNS), conducted with the commercial fluid simulation software Ansys Fluent ©. The algorithm for conducting the DNS and visualisation of the flow pattern is presented here, followed by the parameters of the utilized mesh and applied conditions. Fluent does not provide the inherent settings for a DNS. However, the laminar turbulence model, in connection with the very fine spacial and time resolutions as listed in Table D.1, can be considered a direct numerical simulation. The spatial resolution is chosen in order to be smaller than the Kolmogorov length scale [**197**], and the time resolution is chosen in order to ensure a Courant-Friedrichs-Lewy (CFL) number of unity or smaller $CFL \leq 1$ [**198**]. SIMPLEC is used as a solver. The boundary conditions are a harmonically oscillating free stream velocity $u(t) = U_f \cos(\omega t)$. Nine oscillation periods are calculated for the transient effects to wear off. The velocity distribution around the particle for each time step in the tenth period is then exported via text file into Matlab© [**199**]. Here, the velocities are averaged over the tenth period and converted into the CSV format. After being exported to ParaView© [**200**], the resulting vector field is normalized with the free stream velocity amplitude. The streamlines are then visualized and displayed in a circular window of 5 particle diameters around the particle. The mesh has a spacial resolution at the surface of the particle that starts with 0.03 d and a cell height of 3.94×10^{-5} d. The cell height increases over 300 layers with a rate

of 1.02. The fine mesh near the particle is enveloped by a coarse mesh with a cell size of 0.39 d, as displayed in Figure D.1. In case the particle displacement amplitude was much larger than the particle diameter ($\epsilon \gg 1$), a dynamic mesh was applied. The applied parameters for the various cases, presented in Chapter 6, are listed in Table D.1.

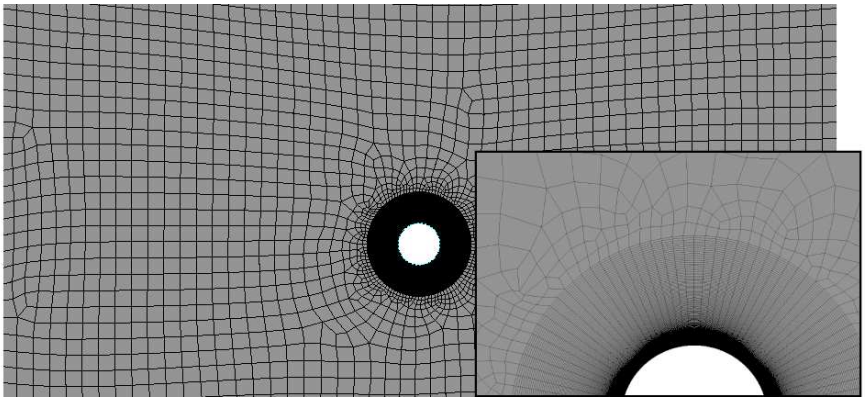

Figure D.1. The mesh utilized in the DNS. The spacial resolution at the surface of the particle starts with 0.03 d and a cell height of 3.94×10^{-5} d. The cell height increases over 300 layers with a rate of 1.02. The fine mesh near the particle is enveloped by a coarse mesh with a cell size of 0.39 d.

Table D.1. A list of applied parameters for the conducted DNS. The results are presented in Chapter 6. The parameters are the oscillation Reynolds number Re, the amplitude parameter ϵ, the kinematic viscosity ν, the velocity amplitude U, the particle diameter d, the angular frequency ω, the time step Δt, the spatial step Δx, and the Courant-Friedrichs-Lewy number CFL.

Re [-]	ϵ [-]	ν [m^2/s]	U [m/s]	d [m]	ω [1/s]	Δt [s]	Δx [m]	CFL [-]
10^{-3}	10^{-3}	1.83×10^{-4}	0.183	10^{-6}	1.83×10^{8}	2.15×10^{-10}	3.94×10^{-11}	10^{-3}
10^{-3}	1	1.83×10^{-4}	0.018	10^{-5}	1.83×10^{3}	2.15×10^{-7}	3.94×10^{-10}	0.01
10^{-3}	10^{3}	1.83×10^{-4}	0.183	10^{-6}	183	2.15×10^{-6}	3.94×10^{-11}	1
1	10^{3}	1.83×10^{-4}	18.3	10^{-5}	1.83×10^{3}	2.15×10^{-7}	3.94×10^{-10}	1
10^{3}	10^{3}	1.83×10^{-4}	18.3	0.01	1.83	2.15×10^{-4}	3.94×10^{-7}	1
1	10^{-3}	1.83×10^{-4}	0.18	10^{-3}	1.83×10^{5}	10^{-8}	3.94×10^{-8}	4.64×10^{-5}
100	1	1.83×10^{-4}	1.83	0.01	183	1.09×10^{-8}	2×10^{-9}	0.01

APPENDIX E

Conducted Data Preparation for HMT Models

The paper by Al Taweel & Landau [**88**] was the source for some of the works listed in Table 7.1. The handling of these works was conducted as follows: there was an attempt to retrieve the original paper. If this was not possible, the information stated by Al Taweel & Landau was used. In this case, their paper was indicated as the source of the data. In case the original paper was available, the data were compared with Al Taweel & Landau. In some cases, they did not specify a value or range of a parameter, even though it could be indirectly retrieved by the relations in Figure 4.8 or by other relations in general. These steps in data preparation are listed here for each individual case:

† Al Taweel & Landau did not provide a value range for the displacement amplitude A and stated only that the amplitude parameter is much smaller than unity for the work of Burdukov & Nakoryakov [**89**]. While this statement agrees with the respective paper, also the applied decibel range of the utilized levitator is stated in that paper: 150 dB to 163 dB. With the standard reference sound pressure level of $p_0 = 20\,\mu\text{Pa}$ [**201**] and the linear relation between pressure amplitude P and velocity amplitude U_f, $P = \rho_f c U_f$, with the speed of sound c in the fluid, the fluid velocity amplitude was calculated. Since no significant particle relaxation occurs [**160**], the slip velocity amplitude was set equal to the fluid velocity amplitude as given in Table E.1. Subsequently, the displacement amplitude and the amplitude parameter were calculated according to the relations in Figure 4.8.

‡ Al Taweel & Landau did not provide a value for the diameter of the sphere, but in the original paper of Burdukov & Nakoryakov [**90**], it is stated that the glass sphere with mount weighed about $m_{sphere} = 1.3\,\mathrm{g}$. Additionally, the thickness of benzoic acid coating was about $d_{acid} - d_{sphere} = \Delta d = 0.6\,\mathrm{mm}$ to $1\,\mathrm{mm}$, with a weight of about $m_{acid} = 150\,\mathrm{mg}$. This information allows for two ways of estimating the diameter of the glass sphere:

(1) Neglecting the weight of the mount and assuming the utilization of borosilicate glass, which is often used in a scientific environment, with a density of about $\rho_{sphere} = 2235\,\mathrm{kg/m^3}$ [**202**], the diameter can be calculated to about

$$V_{sphere} = \rho_{sphere} m_{sphere} = \frac{\pi}{6} d_{sphere}^3 \tag{E.1}$$

$$d_{sphere} = \left(\frac{6 m_{sphere}}{\pi \rho_{sphere}}\right)^{1/3} \approx 1\,\mathrm{cm} \tag{E.2}$$

In case ordinary glass (soda–lime) was used with a density of $\rho_{sphere} = 2520\,\mathrm{kg/m^3}$, the spheres would be insignificantly smaller.

(2) Calculating the dimensions of the coating by assuming a benzoic acid density of $\rho_{acid} = 1.260\,\mathrm{kg/m^3}$ [**203**], the diameter can be calculated

$$V_{acid} = \rho_{acid} m_{acid} = \frac{\pi}{6}\left(d_{acid}^3 - d_{sphere}^3\right) \tag{E.3}$$

$$d_{sphere} = -\frac{\Delta d}{2} + \sqrt{\left(\frac{\Delta d}{2}\right)^2 + \frac{\Delta d^2}{3} + \frac{2 m_{acid}}{\pi \rho_{acid} \Delta d}} \approx 1\,\mathrm{cm} \tag{E.4}$$

Even though Equation E.4 has two theoretical solutions due to its quadratic nature, only the physically plausible solution with a positive diameter was chosen.

In approaches 1 and 2, the diameter of the sphere can be estimated to be $d \approx 1\,\mathrm{cm}$. Therefore, this value is used in this work. Still, this problem is undetermined and the determination of another parameter is necessary in order to calculate all the parameters listed in Table E.1. In the original paper it is stated that the frequency varied from 10 Hz to 125 Hz, translating to angular frequencies of $63\,\mathrm{s}^{-1}$ to $785\,\mathrm{s}^{-1}$. All other input properties listed in the first row of Figure 4.8 are kept constant except the velocity amplitude U, which is dependent on the frequency. The parameter $K = \left[(U^2 d)/(2\sqrt{\omega\nu}D)\right]^{1/3}$ in the original paper was varied between 100 and 1200. The Schmidt number $Sc = \nu/D$ was estimated by Al Taweel & Landau to be approximately 1000 in this setup. Adopting this value and linking low oscillation frequencies to low velocity amplitudes and high oscillation frequencies to high velocity amplitudes delivers an investigated velocity amplitude window of approximately $U \approx 0.02\,\mathrm{m\,s}^{-1}$ to $1.43\,\mathrm{m\,s}^{-1}$. With these values, all the parameters listed in Table E.1 can be determined via the relations in Figure 4.8.

†† One parameter is missing in the original paper by Boldarev et al. [**95**] in order to calculate all the values listed in Table E.1. The velocity amplitude is calculated via the same approach as in the previous paragraph. The parameter $b = (U^{2/3}(d/2)^{1/3})/((\omega\nu)^{1/6}D^{1/3})$ is varied between 25 and 100 in the original paper while keeping all parameters except the oscillation frequency constant. This translates with $Sc = \nu/D \approx 2200$ to a velocity amplitude window of about $U \approx 0.24\,\mathrm{m\,s}^{-1}$ to $239\,\mathrm{m\,s}^{-1}$.

Table E.1. A list of investigated works by Al Taweel & Landau [**88**]. Some of their stated data have been marked (†, ‡, ††) and expanded with information from the original papers.

Authors	$\boldsymbol{\omega}$ [s^{-1}]	$\boldsymbol{A}$ [m]	$\boldsymbol{d}$ [m]	$\boldsymbol{U}$ [ms^{-1}]	$\boldsymbol{\nu}$ [m^2s^{-1}]	$\boldsymbol{\epsilon}$ [-]	$\boldsymbol{Re}$ [-]	**Source**
Fiklistov & Aksel'rud	3.8	1.2×10^{-3}	5×10^{-3}	2.1×10^{-3}	10^{-6}	0.24	10.5	[**91**]
	33.3	3.5×10^{-3}		1.9×10^{-2}		0.7	93.5	
Burdukov & Nakoryakov †	7.2×10^{4}	2.0×10^{-5}	3.5×10^{-3}	2.2	1.2×10^{-5}	2×10^{-3}	5.5×10^{2}	[**89**]
	1.1×10^{5}	1.4×10^{-4}	10^{-2}	9.8		4.5×10^{-2}	8.4×10^{3}	
Subramaniyam et al.	25	2.7×10^{-2}	1.3×10^{-2}	0.3	10^{-6}	1	4.5×10^{3}	[**88**]
	126	3.7×10^{-2}	2.5×10^{-2}	8.0		2.5	2.0×10^{5}	[**190**]
Burdukov & Nakoryakov ‡	63	3.2×10^{-4}	1×10^{-2}	2×10^{-2}	10^{-6}	3.2×10^{-2}	2×10^{2}	[**90**]
	785	1.8×10^{-3}		1.4		0.18	1.4×10^{4}	
Noordzij & Rotte	0	7.8×10^{-4}	2.5×10^{-2}	0.17	10^{-6}	3×10^{-2}	16	[**88**]
	220	1.6×10^{-3}		0.33		6×10^{-2}	2.6×10^{2}	[**98**]
Padamanabha &	19	1×10^{-2}	2.5×10^{-2}	0.19	1.2×10^{-5}	0.2	4×10^{2}	[**93**]
Ramachandran	63	2.2×10^{-2}	5×10^{-2}	1.38		0.87	2.9×10^{3}	
Hara et al.	1.2×10^{4}	4.4×10^{-5}	6.8×10^{-3}	5.5	10^{-6}	4.4×10^{-3}	5.5×10^{4}	[**88**]
	1.2×10^{5}	7.2×10^{-4}	10^{-2}	9.0		0.11	6.1×10^{4}	
Boldarev et al. ††	1.3×10^{5}	1.9×10^{-6}	1.5×10^{-4}	0.24	10^{-6}	3.1×10^{-4}	35.4	[**95**]
	6.3×10^{6}	3.8×10^{-5}	6×10^{-3}	239		0.25	1.4×10^{6}	
Gibert & Angelino	5	1.6×10^{-3}	8×10^{-3}	6.6×10^{-3}	10^{-6}	0.2	2×10^{2}	[**96**]
	25	2.3×10^{-2}	3×10^{-2}	6.3×10^{-1}		0.75	5×10^{3}	
Gibert & Angelino	5	6×10^{-3}	8×10^{-3}	9.8×10^{-3}	10^{-6}	0.75	3×10^{2}	[**96**]
	25	6.1×10^{-2}	3×10^{-2}	0.5		2	4×10^{3}	